Study of a novel VUV-imaging system in liquid argon for neutrino oscillation experiments

Relatore:
Dott.ssa Nicoletta Mauri

Correlatore:
Dott. Michele Pozzato

Presentata da:
Valerio Pia

Sommario

Negli ultimi decenni, una delle più importanti scoperte riguardanti i neutrini è stata il fenomeno delle oscillazioni, che implica una massa del neutrino non nulla. Il loro studio può fornire risposte a molte domande aperte riguardo la natura dei neutrini.

DUNE, un esperimento *long-baseline* sui neutrini, è attualmente in fase di costruzione ed avrà come obiettivo principale quello di misurare alcuni parametri delle oscillazioni ancora ignoti, come il segno di Δm_{13}^2, che definisce l'ordinamento delle masse dei neutrini, ed il valore della fase di violazione CP, δ_{CP}.

In questa tesi, è effettuato uno studio preliminare di un nuovo sistema di imaging, in grado di operare in presenza di intensi flussi di particelle. Questo sistema sfrutterà la luce di scintillazione *Vacuum Ultra Violet* (VUV) emessa dall'Argon liquido per fornire una ricostruzione completa delle tracce. La fattibilità di questa tecnica è studiata confrontando due diversi sistemi ottici: una camera basata sulla *Coded Aperture Technique* ed una tradizionale basata sulle lenti.

Abstract

In the last decades, neutrino oscillation has been one of the most important discoveries regarding neutrinos, as it implies a non-zero neutrino mass and its study could provide answers to many open questions about their nature.

DUNE, a long-baseline neutrino experiment, is currently being built and it will aim to measure some of the still unknown oscillation parameters, as the sign of Δm_{13}^2, which defines the neutrino mass ordering, and the value of the CP-violation phase δ_{CP}.

In this thesis work, a preliminary study of a new imaging system, able to operate in an high flux of particles, is performed. This system will exploit the Vacuum Ultra Violet (VUV) scintillation light emitted by liquid Argon to provide a complete event reconstruction. The feasibility of this detector is studied comparing two possible optical systems: a camera based on the Coded Aperture Technique and a traditional camera based on lenses.

Contents

Introduction

Since their discovery neutrinos played a crucial role in particle physics. In the last decades our knowledge on neutrino physics has increased remarkably and this has generated questions about Nature that are still waiting for answers. One of the most important discoveries regarding neutrinos is the neutrino oscillation phenomenon that arises from mixing between the flavor (ν_e, ν_μ, ν_τ) and mass (ν_1, ν_2, ν_3) eigenstates.

In the last years, many experiments studied neutrinos from different sources, increasing the knowledge about parameters involved in the neutrino oscillation. As of today, however, some of these parameters are still unknown and the identification of their value through the study of neutrino oscillations can be a crucial turning point in trying to answer some of the still open questions. Among these, two of the most important ones are the neutrino mass ordering and the possibility of CP violation in the leptonic sector.

The studies of those parameters are carried on with a quite wide array of experiments: solar, atmospheric, accelerator and reactor neutrino experiments are needed because of the different environment in the generation and propagation of neutrinos and, as a consequence, different sensibility to the mixing parameters. In this context, the Deep Underground Neutrino Experiment (DUNE) is currently being built and will have a key role. DUNE will be a dual-site experiment which will investigate neutrino physics aiming to answer open questions regarding them. It will be composed by a Near Detector (ND) system located few hundred meters from the neutrino source at Fermilab, and a multi kiloton Liquid Argon Time Projection Chamber (LArTPC) located 1300 Km away from the source, the Far Detector (FD). While at the FD will be performed all the measurements on the neutrino oscillations, the ND will have a dual purpose. The first scope is to perform all the measurements needed to achieve the systematic precision required in the studies on neutrino oscillation at the FD. For this reason the ND must be built with the same target of the FD (i.e. liquid Argon). At the same time, thanks to the high fluxes available at the ND site, together with the request of an high-resolution high-granularity detector, it will be able to conduct search for new physics like light dark matter candidates and heavy neutrinos.

Due to the high particle flux available at the ND and the slow time response of the LArTPC used at the FD, this type of detector is not suitable to be used at the ND and some alternative design could be necessary.

One possible solution currently being studied is to exploit the scintillation light produced by charged particles in Liquid Argon to provide a complete 4D event reconstruction in a timescale of few nanoseconds. However, Liquid Argon emits photons with wavelength in the region of the Vacuum Ultra Violet, making lenses and mirrors, commonly used as optical system, highly inefficient. A different method is thus being studied: the Coded Camera Technique, an imaging technique already well known in the X-ray and gamma astronomy. This method is an extension of the simpler pinhole system and uses a multitude of holes to form a mask. Coupling the mask with a set of photon detectors such as CCD or SiPMs one should be able to reconstruct the initial event with the advantage of a theoretically infinite Depth of Field (DOF) and high light transmission.

This thesis work aims to study the feasibility of a particle detector based on this technique. In particular, a comparison between the use of lenses and masks as optical systems is made to better understand the advantages and limitations of both the devices. To do so, a simulation of the scintillation light is performed using the Geant4 simulation toolkit. The results are then used to simulate the two optical systems, the detector response and to reconstruct the initial images. With the images being reconstructed, a study on the achievable spatial resolution of the detector is also made. This work is organized as follow:

- Chapter 1 gives an overview of the theoretical and experimental state of the art on neutrino mixing and introduces to two of the open questions: the CP violation and the mass ordering.

- Chapter 2 describes the DUNE experiment, focusing on the description of the measurements performed both at the Far and Near Detector as well as the description of the detectors themselves.

- Chapter 3 presents the concept of the detector, describes the Coded Aperture Technique and compares the advantages and limitations of both a coded camera and a traditional lens camera.

- Chapter 4 describes the detector simulation, the parameters optimization and the analyses performed for both the optical systems studied.

- Chapter 5 reports the results obtained from the simulations described in the previous chapter for both the cameras.

Chapter 1

Neutrinos

Neutrinos are the most elusive particles known. They are color-less and charge-less fermions and they only interact with charged fermions and massive gauge bosons through weak interactions. In the last decades, neutrino physics has advanced quickly and dramatically thanks to a remarkable suite of experiments and theoretical works that have made possible to reach the modern knowledge about their properties. In the Standard Model, neutrinos and antineutrinos are distinct and massless particles, and their helicity is always left-handed for the neutrinos and right-handed for the antineutrinos. These properties are well explained by the two-component model of neutrinos. The main point of this model is the massless nature of neutrinos, which implies a permanent chirality state, equal to the helicity, for both neutrinos and antineutrinos. However, in the last decades, the discovery of the neutrino oscillation phenomenon requests that the mass of both neutrinos and antineutrinos is different from zero and that the Standard Model must be extended.

1.1 The Physics of Neutrino

1.1.1 Flavor and Mass

Neutrinos and antineutrinos can be distinguished in three different types known as flavors: ν_e and $\bar{\nu}_e$ are the electron-type neutrinos, ν_μ and $\bar{\nu}_\mu$ are the muon-type and ν_τ and $\bar{\nu}_\tau$ are the tau-type. The distinction is based on the fact that the charged current (CC) interaction of one type of neutrino produces the associated lepton: electron for the electron-type, muon and tau for the others respectively:

$$\nu_e + X \rightarrow e^- + Y$$
$$\nu_\mu + X \rightarrow \mu^- + Y \quad\quad\quad (1.1)$$
$$\nu_\tau + X \rightarrow \tau^- + Y.$$

Experiment	Parameter	Limit	CL
Troitsk	$m_{\bar{\nu}_e}$	< 2.05 eV	95%
Mainz	$m_{\bar{\nu}_e}$	< 2.3 eV	95%

Table 1.1: Upper bounds on the ν_e mass obtained by the Troitsk and Mainz experiments.

In the Standard Model, neutrinos are massless particles but the phenomenon of neutrino oscillations has given evidence of a neutrino mass different from zero. Those oscillations, discussed more in detail later, are the consequence of a flavor neutrino mixing, where a left-handed flavor neutrino of the Standard Model of the Eq. (1.1), $|\nu_f\rangle$, is seen as a combination of mass eigenstates, $|\nu_j\rangle$ (with $m_j \neq 0$):

$$|\nu_f\rangle = \sum_j U_{fj}|\nu_j\rangle \qquad f = e, \nu, \tau \qquad j = 1, 2, 3 \qquad (1.2)$$

where U is the neutrino mixing matrix and $|\nu_j\rangle$ is the left-handed component of the field of $|\nu_j\rangle$. The phenomenon of oscillations and mixing can be explained only assuming that at least two neutrinos' masses are distinct and different from zero. The absolute neutrino mass, however, is still unknown, since oscillations experiments can measure only the squared mass differences between two mass eigenvalues and direct measurement experiments have reached only upper limits on neutrino mass.

There are different methods used today to estimate the absolute neutrino mass: cosmological studies, search for neutrinoless-double β-decay and direct measurements based on the kinematics of single β-decay. As of today, only upper limits are reached. For what concerns the single β-decay, the most stringent results on the effective electron anti-neutrino mass were obtained by the Troitsk[1] and Mainz[2] experiments and are reported in Table 1.1. The upcoming KATRIN experiment will push the sensitivity down to 0.2 eV[3].

Results obtained using cosmological data, such as the ones from the WMAP and Planck experiments, provide an upper limit on the sum of neutrino masses. Such results are model dependent and, in the Standard Cosmological Model ΛCDM, the typical values are: $\sum_i m_i \lesssim (0.3 - 1.3)$ eV[4].

Despite the high number of experiments and theoretical studies, the reason beyond the non-zero neutrino mass is still unknown. The Standard Model is not able to account for neutrino masses; moreover, unlike other fermions, neutrinos do not carry electric or color charge. This opens the possibility that neutrinos can be their own anti-particles. A fermion with such property is known as Majorana fermion while, in the other case, is known as Dirac fermion.

Describing the neutrinos as Dirac particles, the mass term of the Dirac equation can

be written as:

$$\mathcal{L} = m_D(\bar{\psi}_L\psi_R + \bar{\psi}_R\psi_L) \qquad \text{with} \quad \bar{\psi}_R\psi_L = (\bar{\psi}_L\psi_R)^\dagger \tag{1.3}$$

where both a left- and a right-handed Dirac neutrino and anti-neutrino are needed to produce it. Up to date, there is no experimental evidence of the existence of a right-handed neutrino. Hence, or the right-handed neutrino does not interact weakly or there is some other mass term to take into account.

A different approach is to make use of the charge-conjugation matrix $\mathcal{C}$ to rewrite the Dirac equation in term of left-handed fields only, in which the fields can be written as[5]:

$$\psi = \psi_L + \psi_R = \psi_L + \psi_L^c. \tag{1.4}$$

This result shows that the charge-conjugate of the Majorana field is the field itself or that a Majorana particle is its own anti-particle:

$$\psi^c = (\psi_L + \psi_L^c)^c = \psi_L^c + \psi_L = \psi. \tag{1.5}$$

Because of the use of the charge conjugation operator the only particle suitable to be a Majorana particle is the neutrino, the only neutral fermion in the Standard Model. For a Majorana particle, it is now possible to rewrite the mass term using only left-handed component of the field:

$$\mathcal{L}_L^M = -\frac{1}{2}m\bar{\psi}_L^c\psi_L. \tag{1.6}$$

Today, there are no observations able to claim whether neutrinos are Dirac or Majorana particles and this is one of the main open questions about their nature.

1.1.2 Neutrino mixing and oscillations

Most of the neutrino parameters known today have come from the study of neutrino oscillations with solar, reactor and accelerator neutrinos. Neutrino oscillations are flavor changes that can occur in flight because of the neutrino mixing. The fact that flavor neutrino oscillation exists means that, for example, a muon-neutrino produced in a weak interaction with energy E has, after a long enough distance L from the source, a non-zero probability to change in a neutrino of different flavor: $P(\nu_\mu \to \nu_{e,\tau}; E, L) \neq 0$.

This oscillations are a consequence of the flavor neutrino mixing where the neutrino flavor states (ν_e, ν_μ, ν_τ) are seen as a combination of mass eigenstates (ν_1, ν_2, ν_3):

$$|\nu_\alpha\rangle = \sum_j U_{\alpha j}|\nu_j\rangle \qquad \alpha = e, \nu, \tau \qquad j = 1, 2, 3 \tag{1.7}$$

where the matrix U is called the Pontecorvo-Maki-Nakagawa-Sakata (PMNS) mixing matrix. The minimal neutrino mixing scheme is in agreement with a three-flavor neutrino

mixing in vacuum and agrees with all the available data on the oscillations. In such a scheme, the PMNS matrix is a 3×3 unitary matrix that can be parametrized by three rotation angles θ_{23}, θ_{13}, θ_{12} ($0 \leq \theta_i \leq \pi/2$) and by 1 or 3 CP violation phases depending on whether the neutrinos are Dirac or Majorana particles. The mixing matrix can be represented by the matrix product

$$U = \begin{bmatrix} 1 & 0 & 0 \\ 0 & c_{23} & s_{23} \\ 0 & -s_{23} & c_{23} \end{bmatrix} \begin{bmatrix} c_{13} & 0 & s_{13}e^{-i\delta} \\ 0 & 1 & 0 \\ -s_{13}e^{-i\delta} & 0 & c_{13} \end{bmatrix} \begin{bmatrix} c_{12} & s_{12} & 0 \\ -s_{12} & c_{12} & 0 \\ 0 & 0 & 1 \end{bmatrix} \begin{bmatrix} 1 & 0 & 0 \\ 0 & e^{i\phi_2/2} & 0 \\ 0 & 0 & e^{i\phi_3/2} \end{bmatrix} \quad (1.8)$$

where c_{jk} and s_{jk} represent respectively $\cos\theta_{jk}$ and $\sin\theta_{jk}$, $\delta = [0, 2\pi]$ is the Dirac CP violation phase and ϕ_2, ϕ_3 ($\phi_i \leq 2\pi$) are the two Majorana CP violation phases. Setting both $\phi_2 = \phi_3 = 0$ the standard form of the 3×3 matrix for neutrino oscillations is obtained[6]:

$$U = \begin{bmatrix} c_{13}c_{12} & c_{13}s_{12} & s_{13}e^{-i\delta} \\ -s_{12}c_{23} - c_{12}s_{23}s_{13}e^{i\delta} & c_{12}c_{23} - s_{12}s_{23}s_{13}e^{i\delta} & s_{23}c_{13} \\ s_{12}s_{23} - c_{12}c_{23}s_{13}e^{i\delta} & -c_{12}s_{23} - s_{12}c_{23}s_{13}e^{i\delta} & c_{23}c_{13} \end{bmatrix} \quad (1.9)$$

It is now possible to determine the probability that a neutrino of a certain flavor generated at the source will oscillate in some other flavors after travelling a distance L.

Vacuum oscillations

Using the Eq. (1.7) it is possible to describe the state of a neutrino in the production point at the production time. The request of knowing the state at the distance L and after a certain time T can be resolved using the space-time translation operator $e^{\left(-i\hat{E}t + i\hat{P}\cdot L\right)}$, with $\hat{E}$ and $\hat{P}$ energy and momentum operator. Applying such operator on the state $|\nu_f\rangle$ of the Eq. (1.7) the resulting state is[7]:

$$|\nu_\alpha(L,T)\rangle = \sum_j U_{\alpha j}^* e^{-iE_j T + ip_j L} |\nu_j\rangle. \quad (1.10)$$

Inverting the Eq. (1.7) it is possible to write $|\nu_j\rangle$ in terms of the flavor neutrino states $|\nu_j\rangle = \sum_{\beta = e,\mu\tau} U_{\beta j} |\nu_\beta\rangle$ and, using this result and Eq. (1.10) one obtains:

$$|\nu_\alpha(L,T)\rangle = \sum_{\beta = e,\mu\tau} \left(\sum_j U_{\alpha j}^* e^{-iE_j t + ip_j L} U_{\beta j} \right) |\nu_\beta\rangle. \quad (1.11)$$

Equation (1.11)) shows that the state describing the neutrino at a distance L after a time T is indeed a superposition of different neutrino flavors. The probability of the transition $\nu_\alpha \to \nu_\beta$ is then given by

$$P_{\nu_\alpha \to \nu_\beta}(L;T) = |\langle \nu_\beta | \nu_\alpha(L,T)\rangle|^2 = \left| \sum_j U_{\alpha j}^* e^{-iE_j T + ip_j L} U_{\beta j} \right|^2. \quad (1.12)$$

As can be seen, the probability (1.12) depends on space and time spent from the generation of the neutrino until its detection. It can be useful to rewrite such probability as a function of phenomenological parameters. In case of ultrarelativistic neutrinos, the propagation time is equal to the traveled distance up to some corrections depending on the mass and the energy of the neutrino. This leads to the approximation

$$E_j t - p_j x \simeq (E_j - p_j)L = \frac{E_j^2 - p_j^2}{E_j + p_j}L = \frac{m_j^2}{E_j + p_j}L \simeq \frac{m_j^2}{2E}L. \tag{1.13}$$

Using this approximation the probability of the $\nu_\alpha \to \nu_\beta$ transition can be written as

$$
\begin{aligned}
P_{\nu_\alpha \to \nu_\beta}(L) &= \left| \sum_j U_{\alpha j}^* e^{-\frac{im_j^2 L}{2E}} U_{\beta j} \right|^2 \\
&= \sum_j |U_{\alpha j}|^2 |U_{\beta j}|^2 + 2Re \sum_{j>k} U_{\alpha j}^* U_{\beta j} U_{\alpha k} U_{\beta k}^* exp\left(-i\frac{\Delta m_{jk}^2 L}{2E} \right)
\end{aligned}
\tag{1.14}
$$

where m_j are the mass eigenstates and $\Delta m_{jk}^2 = m_j^2 - m_k^2$, $j \neq k$.

Neutrino oscillations are thus governed by a set of fundamental parameters:

- the three mixing angles θ_{12}, θ_{23} and θ_{13},

- one or three CPV phases depending on whether the neutrinos are Dirac or Majorana particles,

- the two squared mass differences.

The probability (1.14) is valid regardless of the process that generates the neutrino and different values of L/E can be used to investigate different Δm^2 regimes, defining two main experimental ranges. The different types of experiments are thus classified depending on the value of L/E, which determine their sensitivity to Δm^2, defined as the value of Δm^2 for which:

$$\frac{\Delta m^2 L}{2E} \sim 1. \tag{1.15}$$

Commonly, neutrino oscillation experiments are subdivided in two categories:

- Short-baseline (SBL) experiments. These experiments exploit neutrinos produced in nuclear reactors or in particle accelerators by the decay of pions, kaons and muons. In these experiments the source-detector distance is usually short, $\mathcal{O}(10\text{m} \div 1\text{km})$. The range of L/E and the sensitivity of these experiments go from

$$\frac{L}{E} \lesssim 10\text{m/MeV} \implies \Delta m^2 \gtrsim 0.1\text{eV}^2 \tag{1.16}$$

7

for the reactor experiments, to

$$\frac{L}{E} \lesssim 1 \text{ km/GeV} \implies \Delta m^2 \gtrsim 1 \text{ eV}^2 \qquad (1.17)$$

for the accelerator ones;

- Long-baseline (LBL) and atmospheric experiments. Likewise the SBL experiments, the neutrino sources used in these experiments could be nuclear reactors and accelerators but the source-detector distance is some order of magnitude larger. Despite different values of L/E for reactor and accelerator LBL experiments, their sensitivity is similar and is

$$\begin{array}{ll} \text{Reactors:} & L/E \lesssim 10^3 \text{ m/MeV} \\ \text{Accelerators:} & L/E \lesssim 10^3 \text{ km/GeV} \end{array} \implies \Delta m^2 \gtrsim 10^{-3} \text{ eV}^2. \qquad (1.18)$$

A different value can be reached with atmospheric neutrino experiments, for which L ranges from 20 km, for neutrinos coming from the upper atmosphere, to $\sim 10^4$ km, for neutrinos coming through the other side of the Earth. For these experiments thus, the sensitivity to Δm^2 is

$$\frac{L}{E} \lesssim 10^4 \text{ km/GeV} \implies \Delta m^2 \gtrsim 10^{-4} \text{ eV}^2. \qquad (1.19)$$

Neutrino oscillations experiments can also be divided in appearance and disappearance experiments. This subdivision is based on the type of measurements performed:

- Appearance experiments. They measure the transition from the neutrino's flavor produced by the source and the other ones.

- Disappearance experiments. They measure the survival probability of the neutrino flavor produced by the source by counting the number of interactions in the detector and comparing the result with the expected rate of interactions.

Two flavor case An important approximation of the three-neutrino mixing is the case in which only two different flavors are considered. This approximation simplifies the description of the neutrino oscillation phenomenon due to the smaller number of involved parameters and, since many experiments are not sensitive to all the three neutrinos, it can be used when analyzing their data.

In the two flavor case the flavor neutrinos states $(\nu_e, \nu_\mu$ or ν_e, ν_τ or $\nu_\mu, \nu_\tau)$ are the linear superposition of just two massive neutrinos (ν_1, ν_2) and the PMNS matrix simplifies to a two-dimensional rotation that can be written as

$$U = \begin{bmatrix} \cos\theta & \sin\theta \\ -\sin\theta & \cos\theta \end{bmatrix}. \qquad (1.20)$$

From Eq. (1.14) it is possible to obtain the probability of oscillation for the two-flavor case:

$$P(\nu_\alpha \to \nu_\beta) = \sin^2 2\theta \, \sin^2 \frac{\Delta m^2 L}{4E} \qquad \alpha \neq \beta. \tag{1.21}$$

The survival probability is easily obtained from Eq. (1.21) as:

$$P(\nu_\alpha \to \nu_\alpha) = 1 - P(\nu_\alpha \to \nu_\beta) = 1 - \sin^2 2\theta \, \sin^2 \frac{\Delta m^2 L}{4E} \qquad \alpha \neq \beta. \tag{1.22}$$

Equation (1.21) shows that, as written before, the oscillation amplitude depends only on the ratio L/E and not on L and E independently. It shows also that the maximal probability to find the neutrino in the $|\nu_\beta\rangle$ state can be found after a distance $L_{osc}/2 = 2\pi E/\Delta m^2$ while after a full oscillation length the system is again in the initial state $|\nu_\alpha\rangle$ (Fig. 1.1.
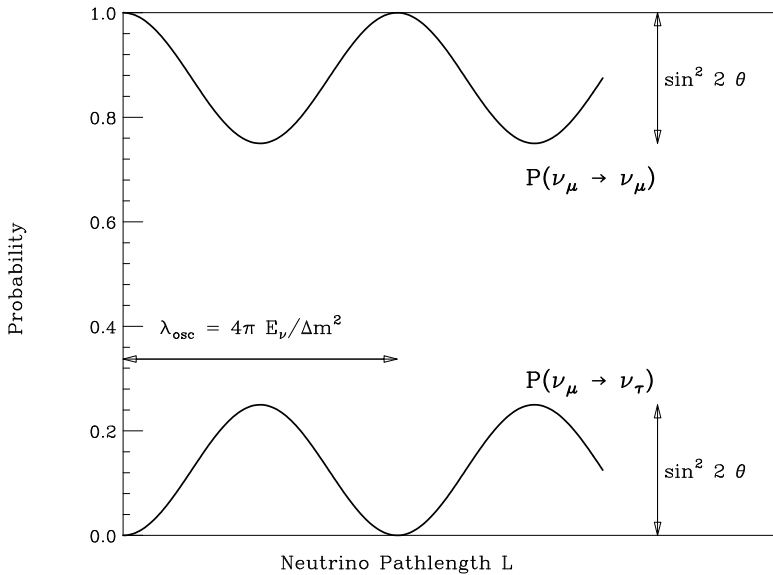

Figure 1.1: Oscillation and survival probability as function of the neutrino pathlength L in the two flavor mixing approximation[8].

Matter effect

When neutrinos propagate in matter, their propagation can be modified by the coherent forward weak charged-current (CC) and neutral-current (NC) scattering from particles they encounter along the way. As a result, the oscillation probability can be rather

different than it is in vacuum. The CC and NC potentials are given by:

$$V_{CC} = \sqrt{2}G_F N_e \qquad V_{NC} = -\frac{1}{2}\sqrt{2}G_F N_n \qquad (1.23)$$

where G_F is the Fermi constant and N_e, N_n are the electron and neutron number density respectively. The CC and NC scattering Feynman diagrams are shown in Fig. 1.2.
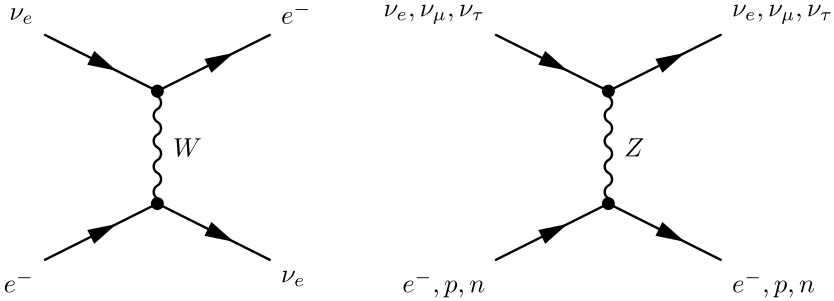

Figure 1.2: Feynman diagrams of the elastic scattering processes that generate the CC potential V_{CC} through W exchange and the NC potential V_{NC} through Z exchange.

The presence of only electrons in the matter makes the CC potential felt only by the electron neutrinos, while the NC potential is felt equally by the three flavor neutrinos. The potential felt by a generic flavor neutrino α is thus:

$$V_\alpha = V_{CC}\delta_{\alpha e} + V_{NC} = \sqrt{2}G_F \left(N_e \delta_{\alpha e} - \frac{1}{2}N_n \right). \qquad (1.24)$$

The importance of the potential felt by neutrinos in matter is evident when calculating the evolution of an ultrarelativistic neutrino state with flavor α. The neutrino evolution obeys the Schrödinger equation:

$$i\hbar \frac{d}{dt}|\nu_\alpha(p,t)\rangle = \mathcal{H}|\nu_\alpha(p,t)\rangle \qquad (1.25)$$

where $\mathcal{H}$ is the total Hamiltonian in matter:

$$\mathcal{H} = \mathcal{H}_0 + \mathcal{H}_1, \qquad \text{with} \qquad \mathcal{H}_1|\nu_\alpha\rangle = V_\alpha|\nu_\alpha\rangle \qquad (1.26)$$

and V_α is the potential (1.24) felt by the neutrino. From the amplitude of the $\nu_\alpha \to \nu_\beta$ transition it is possible to obtain the probability that a neutrino generated with an α flavor is found to have a different flavor β after the time t:

$$P_{\nu_\alpha \to \nu_\beta}(t) = |\psi_{\alpha,\beta}(t)|^2 = |\langle \nu_\beta|\nu_\alpha(t)\rangle|^2. \qquad (1.27)$$

Recalling Eq. (1.7), the time evolution of the flavor transition amplitude $\psi_{\alpha,\beta}(p,t) = \langle \nu_\beta(p)|\nu_\alpha(p,t)\rangle$ is thus, after some simplification[9]:

$$i\frac{d}{dt}\psi_{\alpha,\beta}(x) = \sum_k \left(\sum_j U_{\beta j}\frac{\Delta m_{j1}^2}{2E}U_{kj}^* + \delta_{\beta e}\delta_{ke}V_{CC} \right)\psi_{\alpha k}(x). \tag{1.28}$$

Equation (1.28) can be rewritten as

$$i\frac{\mathrm{d}}{\mathrm{d}t}\Psi_\alpha = \mathcal{H}_F\Psi_\alpha \tag{1.29}$$

where $\mathcal{H}_F$ is given by

$$\mathcal{H}_F = \frac{1}{2E}(U\mathbb{M}^2 U^\dagger + \mathbb{A}). \tag{1.30}$$

For the three-neutrino mixing one has:

$$\Psi_\alpha = \begin{bmatrix} \psi_{\alpha e} \\ \psi_{\alpha\mu} \\ \psi_{\alpha\tau} \end{bmatrix}, \qquad \mathbb{M}^2 = \begin{bmatrix} 0 & 0 & 0 \\ 0 & \Delta m_{21}^2 & 0 \\ 0 & 0 & \Delta m_{31}^2 \end{bmatrix}, \qquad \mathbb{A} = \begin{bmatrix} A_{CC} & 0 & 0 \\ 0 & 0 & 0 \\ 0 & 0 & 0 \end{bmatrix}, \tag{1.31}$$

where

$$A_{CC} \equiv 2EV_{CC} = 2\sqrt{2}EG_F N_e. \tag{1.32}$$

Experimental Results

The current status of neutrino oscillation data and the standard three-neutrino framework came from a quite different array of experiments. The most common subdivision of those experiments is based on which parameters of the PMNS matrix they can better study:

- Solar neutrino experiments, sensitive to $\sin^2\theta_{12}$ and Δm_{21}^2;

- Reactor neutrino experiments, sensitive to θ_{13};

- Atmospheric neutrino experiment, sensitive to $\sin^2\theta_{23}$ and Δm_{31}^2;

- Long-baseline accelerator experiment, used to confirm the oscillation phenomenon with an artificial neutrino source, sensitive to $\sin^2\theta_{23}$, Δm_{31}^2 and θ_{13}.

The environments are quite different in each type of experiments. Such differences manifest in the ratio L/E described in Section 1.1.2 and the conditions of neutrinos production and propagation, and act on the probability (1.14) in a way that makes some of the parameters responsible of the neutrino oscillation negligible.

Solar sector: $\sin^2 \theta_{12}$, Δm^2_{12} Solar neutrino sector includes all the solar neutrino experiments and also the reactor experiment KamLAND, as it is sensitive to the same oscillation parameters.

For solar neutrinos, the value of L/E is such that the effects of Δm^2_{31} in their oscillation is subdominant. This makes solar neutrino experiment sensitive predominantly to $\sin^2\theta_{12}$ and Δm^2_{21} and for this they are also known as solar mixing angle $\theta_{12} = \theta_\odot$ and solar mass squared difference $\Delta m^2_{12} \equiv \Delta m^2_\odot$.

Solar neutrino historical experiments were Homestake, Gallex/GNO and SAGE. Today two of the main experiments still studying solar neutrinos are Super-Kamiokande, a Cherenkov detector of 50 kton pure water in Kamioka, Japan, and Borexino, a liquid scintillator experiment at the Laboratori Nazionali del Gran Sasso, Italy. Both the experiments detect neutrinos through the elastic neutrino-electron scattering. Their purpose, beside increasing the knowledge on the Standard Solar Model, is to study the matter effect in the energy range spanning from hundreds of keV to some MeV. The same energy range is studied by KamLAND, a reactor short-baseline experiment designed to investigate neutrino oscillations through the disappearance of $\bar{\nu}_e$ produced by the inverse beta decay process in a nuclear reactor. In Fig. 1.3 the results of all the solar neutrino
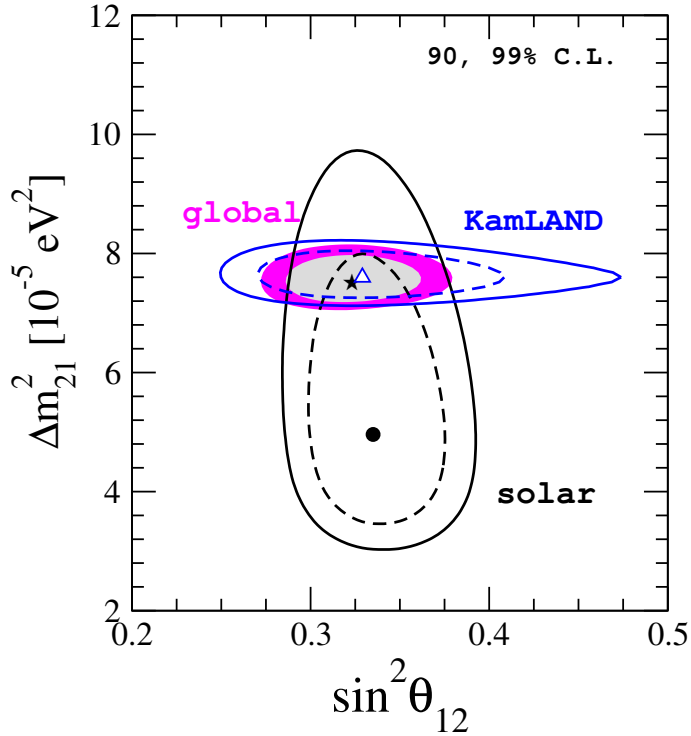

Figure 1.3: Allowed region at 90% (dashed line) and 99% (solid line) from the analysis of solar data (black), KamLAND (blue) and the global fit (colored regions)[10].

Parameter	best-fit	3σ
$\sin^2_{12}$	0.297	6.93 - 7.96
Δm^2_{12}	7.37	0.250 - 0.354

Table 1.2: Best-fit values and 3σ allowed ranges of the solar sector's parameters[11].

experiments are showed in black in the $\sin^2_{12} - \Delta m^2_{12}$ plane while the result obtained by KamLAND are shown in blue. The measurement of Δm^2_{12} has high accuracy thanks to the contribution from KamLAND while the value of θ_{12} is mostly constrained from the solar experiments results. As of today, the best-fit values are reported in Table 1.2.

Short-baseline sector: $\boldsymbol{\theta_{13}}$ The θ_{13} angle was measured very recently thanks to the new generation of reactor short-baseline experiments: Double Chooz, Daya Bay and RENO. As for KamLAND, these experiments detect antineutrinos produced in the inverse beta-decay using Gadolinium-doped liquid scintillator detectors. Thanks to the increased power of their reactors, as well as the possibility to detect antineutrinos using different detectors at $\mathcal{O}(300)$m and $\mathcal{O}(1500)$m from the reactor, these experiments were able to increase the number of total events, allowing a better study of the disappearance of the $\bar{\nu}_e$. Figure 1.4 shows the sensitivity obtained from these experiments and from a
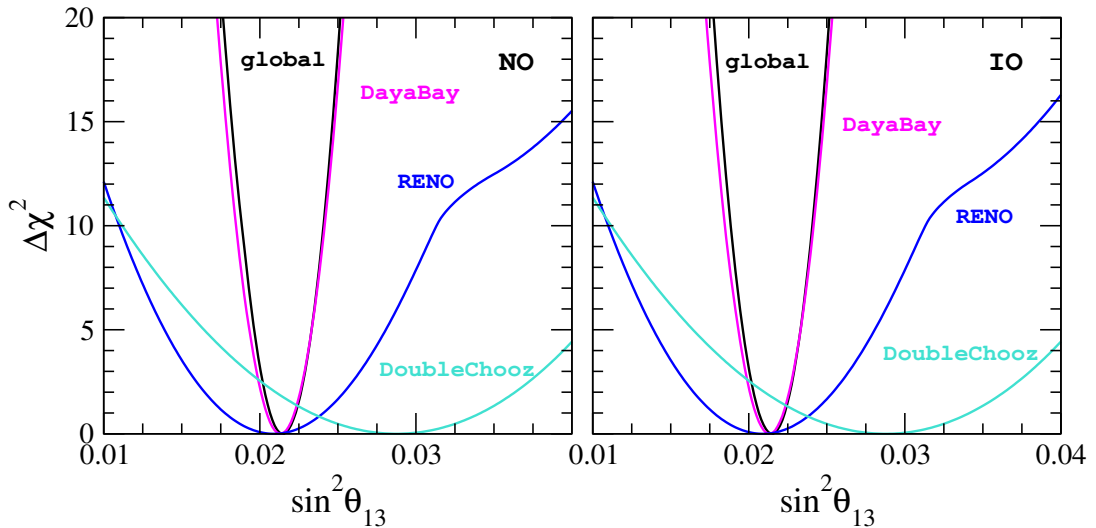

Figure 1.4: Profile of $\Delta\chi^2$ as a function of $\sin^2\theta_{13}$ from global data analysis(black line) and from separate analysis of the reactors experiments. Left panel corresponds to normal mass ordering, right panel to the inverted one[10].

Experiment	parameter	best-fit
Daya Baya	$\sin^2 2\theta_{13}$	$0.0841 \pm 0.0027 \pm 0.0019$
RENO	$\sin^2 2\theta_{13}$	$0.082 \pm 0.009 \pm 0.006$
Double Chooz	$\sin^2 2\theta_{13}$	0.119 ± 0.0016

Table 1.3: Best-fit values of $\sin^2 2\theta_{13}$ obtained by the Daya Bay[12], RENO[13] and Double Chooz[14] experiments.

Parameter	best-fit	3σ
$\sin^2_{13}$, $\Delta m^2_{31} > 0$	0.0215	0.0190 - 0.0240
$\sin^2_{13}$, $\Delta m^2_{31} < 0$	0.0216	0.0190 - 0.0242

Table 1.4: Best-fit values and 3σ allowed ranges for $\sin^2_{13}$ from a global data analysis[11].

global data analysis both for normal and inverted ordering. These orderings, discussed more in detail later, are the two possible ways to order the neutrinos' masses, since one of the two squared mass differences, Δm^2_{31}, is known only as an absolute value. The measurement of θ_{13} is constrained by the Daya Bay measurements. Tables 1.3 and 1.4 summarize the best-fit value of θ_{13} for all the experiments as well as the global fit value.

Atmospheric and Long baseline sector   In the same way as some parameters of the PMNS are related to solar neutrino oscillations, some others are related to the atmospheric ones. Those are the "atmospheric" squared neutrino mass $\Delta m^2_{31} \equiv \Delta m^2_A$ and "atmospheric" neutrino mixing angle $\theta_{23} = \theta_A$.

One of the main contributors in the definition of the value of such parameters is Super-Kamiokande, now in his fourth phase. In recent years neutrino telescope experiments (ANTARES and IceCube), whose main scope is the study astrophysical sources of high-energy neutrinos, have greatly reduced their energy threshold and are able to contribute in the study of atmospheric neutrino oscillation. Both the experiments detect neutrinos via the Cherenkov light emitted after the neutrino interaction with the medium in the vicinity of the detector.

The global-fit value is summarized in the Table 1.5 while Fig. 1.5 (left panel) shows the allowed regions in the $\sin^2 \theta_{23} - \Delta m^2_{31}$ plane obtained with atmospheric experiments.

After the discovery of oscillations in the atmospheric neutrino sector, several long-baseline accelerator experiments studied the oscillation phenomenon with artificial neutrino beam. The first two experiments trying to probe the ν_μ disappearance oscillation
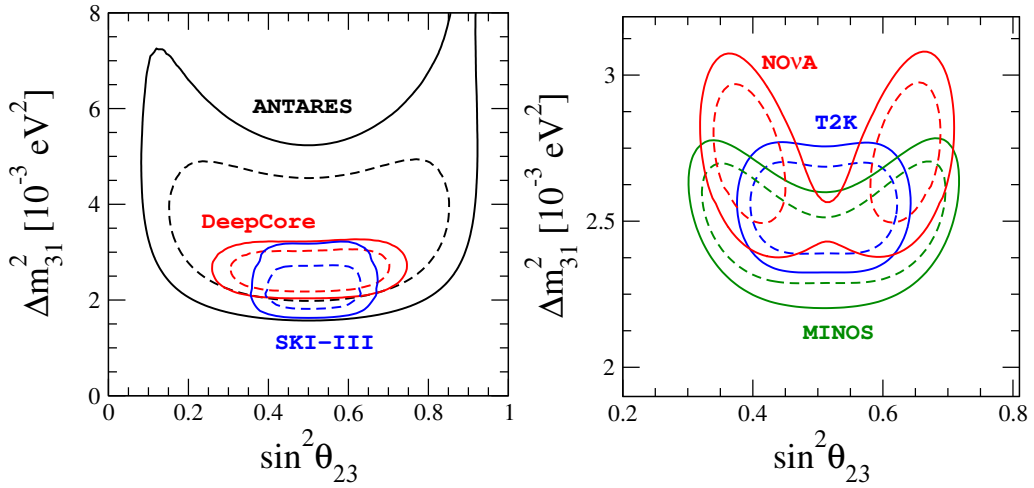
Figure 1.5: 90% and 99% C.L. allowed regions in the $\sin^2\theta_{23} - \Delta m^2_{31}$ plane obtained from the atmospheric (left panel) and long-baseline accelerator experiments (right panel). Both plots correspond to the normal ordered neutrino mass spectra[10].

Parameter	best-fit	3σ
$\sin^2_{23}$, $\Delta m^2_{32} > 0$	0.425	0.381 - 0.615
$\sin^2_{23}$, $\Delta m^2_{32} < 0$	0.589	0.384 - 0.636
Δm^2_{23}	2.54	2.45 - 2.69

Table 1.5: Best-fit values and 3σ allowed ranges of the long-baseline sector's parameters[11].

channel in the same region explored by atmospheric neutrinos were K2K and MINOS. A third experiment, OPERA, studied the appearance of ν_τ in a beam of ν_μ and reported the appearance of ten tau neutrinos. Their successors, T2K and NOνA are still at work today and other experiments, as DUNE, are being built. All this experiments use a beam of muon-neutrinos and search for oscillations in the disappearance ($\nu_\mu \to \nu_\mu$) and appearance ($\nu_\mu \to \nu_e$) channels at some hundreds kilometers of distance from the neutrino source. The results are shown in the right side of the Fig. 1.5 and are compared to the ones obtained with atmospheric experiments. They indicate a value of θ_{23} close to 45°. As of today, it is not clear whether the value of θ_{23} is in the smaller (lower octant), greater (upper octant) than 45° or exactly 45°. The determination of the exact value of this angle is therefore important, as it could be the evidence - if found to be exactly 45° - of a new symmetry.

1.1.3 CP violation

In the parametrization of the PMNS matrix (1.9), the mixing between ν_1 and ν_3 depends on the CP-violation phase δ_{CP}. With the latest results on the measurement of the mixing angles it is now known that the minimal conditions required to measure δ_{CP} are satisfied: all the three mixing angles are different from zero. The presence of a non-zero CP violation term results in an asymmetry in the neutrino versus antineutrino oscillations, the magnitude of which depends on the size of the Jarlskog invariant, $J_{\alpha\beta}$[15]:

$$\Delta P_{\nu\bar{\nu}} \equiv P(\nu_\alpha \to \nu_\beta) - P(\bar{\nu}_\alpha \to \bar{\nu}_\beta) = -16 J_{\alpha\beta} \sin \Delta_{12} \sin \Delta_{23} \sin \Delta_{31} \tag{1.33}$$

where $\Delta_{ij} \equiv \Delta m_{ij}^2 L/4E$, $P(\nu_\alpha \to \nu_\beta)$ is defined as in (1.14) and

$$J_{f\beta} \equiv \text{Im}(U_{f1} U_{f2}^* U_{\beta1}^* U_{\beta2}) = \pm J, \quad J \equiv \frac{1}{8} \sin 2\theta_{12} \sin 2\theta_{13} \sin 2\theta_{23} \cos \theta_{13} \sin \delta. \tag{1.34}$$

Differently from the quark sector, in which the Jarlskog invariant has a very small value[4]:

$$J_{CP}^{CKM} \sim 3 \times 10^{-5}, \tag{1.35}$$

the current best fit of the mixing angle results[16] is a J_{CP}^{PMNS} value in the leptonic sector of:

$$J_{CP}^{PMNS} \sim 0.033 \sin \delta_{CP}. \tag{1.36}$$

Depending on the value of δ_{CP}, the leptonic CP violation effect could then be quite large. The importance of the discovery of CP violation in the leptonic sector is due to the possible explanation for the matter-antimatter asymmetry in the Universe.

Due to the CPT symmetry, the asymmetries in neutrino versus antineutrino oscillation can only be observed in appearance experiments, in which the flavor of the neutrino changes after the oscillation. The most commonly used channel for the search of CP violation in the leptonic sector is the oscillation between muon- and electron-type neutrinos: $\nu_{\mu,e} \to \nu_{e,\mu}$. Taking into account the matter effect and keeping constant the density of the medium, the probability of oscillation for such channel can be written as[17]:

$$P(\nu_\mu \to \nu_e) \cong P_0 + P_{\sin \delta} + P_{\cos \delta} + P3. \tag{1.37}$$

where

$$P_0 = \sin^2 \theta_{23} \frac{\sin^2 2\theta_{13}}{(A-1)^2} \sin^2[(A-1)\Delta], \tag{1.38}$$

$$P_3 = \alpha^2 \cos^2 \theta_{23} \frac{\sin^2 2\theta_{12}}{A^2} \sin^2(A\Delta), \tag{1.39}$$

$$P_{\sin \delta} = \alpha \frac{8 J_{CP}}{A(1-A)} \sin \Delta \sin(A\Delta) \sin[(1-A)\Delta], \tag{1.40}$$

$$P_{\cos \delta} = \alpha \frac{8 J_{CP} \cot \delta_{CP}}{A(1-A)} \cos \Delta \sin(A\Delta) \sin[(1-A)\Delta], \tag{1.41}$$

16

and where

$$A = \frac{\sqrt{3} G_F N_e 2E}{\Delta m_{31}^2},$$
$$\Delta = \frac{\Delta m_{31}^2 L}{4E}, \tag{1.42}$$
$$\alpha \equiv \frac{|\Delta m_{21}^2|}{|\Delta m_{31}^2|}.$$

Here the contribution of the terms P_0 and P_3 is independent from the CP phase and can be ignored. The other two terms, $P_{\sin \delta}$ and $P_{\cos \delta}$ depend on the δ_{CP} phase via J_{CP} and are known as the CP-odd term and CP-conserving terms respectively. This means that the term $P_{\sin \delta}$ changes sign going from $\nu_\mu \to \nu_e$ to the $\bar{\nu}_\mu \to \bar{\nu}_e$ and can be used to study the CP violation with the neutrino oscillations. Recalling that the CP phase appears in the mixing of ν_1 and ν_3 states, the baseline and neutrino energy at which their mixing in maximal determine the characteristics of an appearance experiment as follow:

$$\frac{L(\text{km})}{E_\nu(\text{GeV})} \approx (2n - 1) \times 510 \text{ km/GeV} \tag{1.43}$$

where $n = 1, 2, 3...$ represents the nodes with maximal appearance probability. Fig. 1.6 shows the oscillation probability as a function of both the baseline and neutrino energy as well as the projection of the oscillation probability for a fixed baseline. The fact that different values of δ_{CP} produce differences in the oscillation probabilities makes possible to measure the value of the CP phase using the shape of the $\nu_\mu \to \nu_e$ signal for a full oscillation interval. If the phase δ_{CP} is found to be different from $0°$ and $\pm 180°$ then CP violation occurs.

Moreover, it is possible to define the CP asymmetries as:

$$\mathcal{A}_{CP} = \frac{P(\nu_\mu \to \nu_e) - P(\bar{\nu}_\mu \to \bar{\nu}_e)}{P(\nu_\mu \to \nu_e) + P(\bar{\nu}_\mu \to \bar{\nu}_e)} \tag{1.44}$$

that can be approximated in the three-flavor model as[18]:

$$\mathcal{A}_{CP} \sim \frac{\cos \theta_{23} \sin 2\theta_{12} \sin \delta_{CP}}{\sin \theta_{23} \sin \theta_{13}} \left(\frac{\Delta m_{21}^2 L}{4E_\nu} \right) + \text{matter effects} \tag{1.45}$$

where it is clear that, independently from the value of δ_{CP}, the observation of asymmetries in the neutrino versus antineutrino oscillation probabilities implies the CP violation in the leptonic sector.

The latest results in the measurement of the CP-phase δ_{CP} are obtained by T2K. The experiment made different measurements using $\nu_\mu \to \nu_e$ appearance or joint analyses of ν_e appearance and ν_μ disappearance. In the latter the value of θ_{13} was constrained
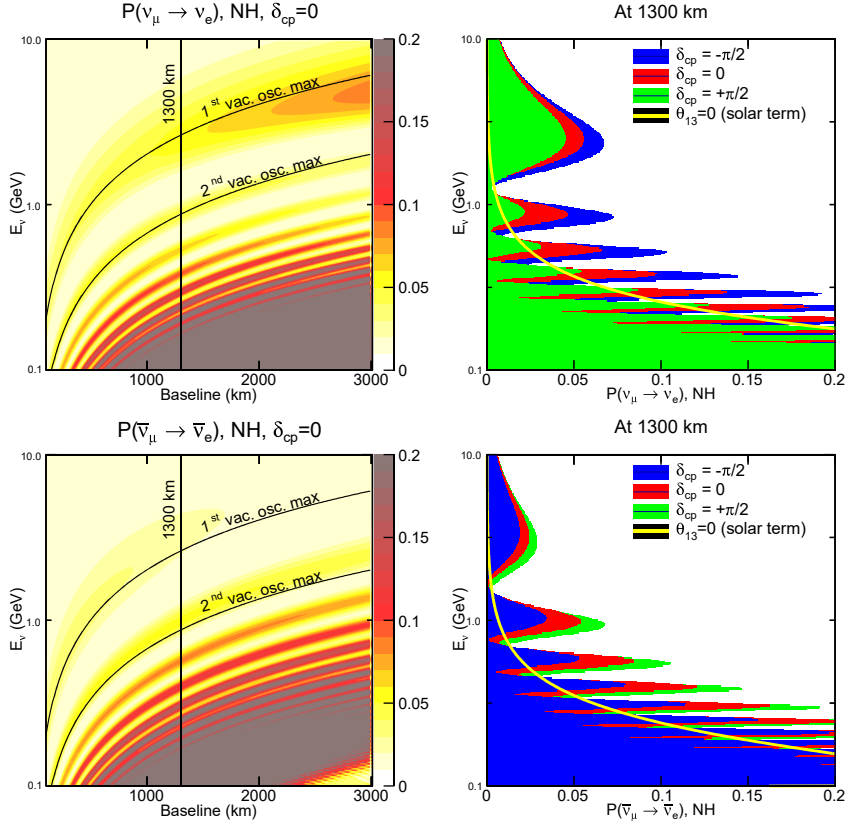
Figure 1.6: (Left) $\nu_\mu \to \nu_e$ oscillation probabilities as a function of baseline and energy for neutrinos (top left) and antineutrinos (bottom left) with $\delta_{CP} = 0$. (Right) show the projection of the oscillation probability on the neutrino energy axis at a baseline of 1,300 km for different values of the CP phase for neutrinos (top right) and antineutrinos (bottom right). Here the baseline of 1300 km is chosen as this will be the baseline of the DUNE experiment, discussed in the next chapter.

by reactor measurements. T2K switched then to a $\bar{\nu}_\mu$ source and performed the same measurement with antineutrinos. In Fig. 1.7 are shown the results of the analysis of the T2K experiment, in which a value of $\delta_{CP} = 0, \pi$ is excluded at 90% CL. The last results from T2K, improved with a better event selection thanks to Super-Kamiokande, exclude a value of $\delta_{CP} = 0$ and π with 2σ CL for both the normal and inverted mass orderings.

Similar results are obtained by the NOνA experiment. NOνA used combined analysis of ν_e appearance and ν_μ disappearance and, since NOνA measurement of $\sin^2 \theta_{23}$ has two statistically degenerate values, there are four possible combinations of mass ordering and θ_{23} octant as in Fig. 1.8. There are two best-fit points for normal mass ordering: $\sin^2 \theta_{23} = 0.404$ and $\delta = 1.48\pi$ and $\sin^2 \theta_{23} = 0.623$ and $\delta = 0.74\pi$. The inverted mass ordering is disfavored for all the value of δ at $> 93\%$[20].
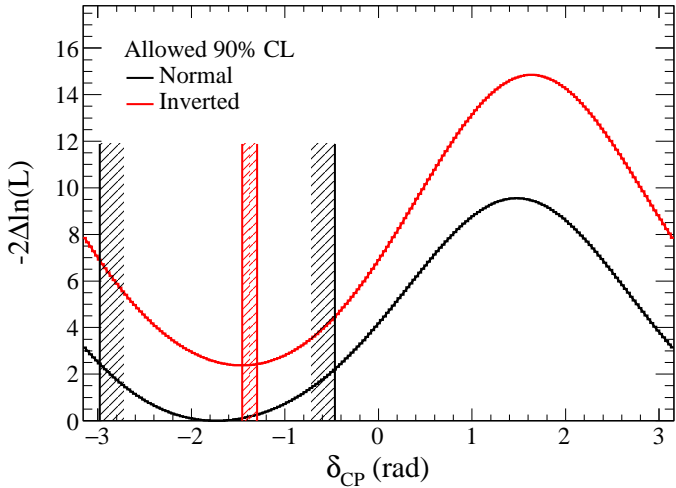
Figure 1.7: Log-likelihood as a function of δ_{CP} for both normal (black) and inverted (red) mass ordering for the T2K experiment. The vertical lines correspond to the allowed 90% confidence interval[19].
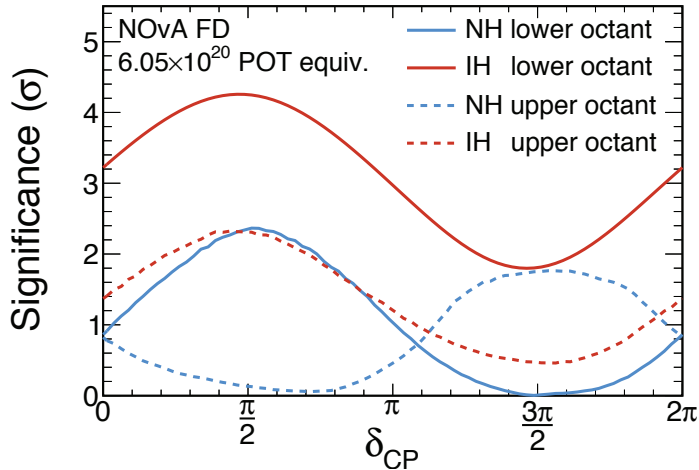

Figure 1.8: Significance at which δ_{CP} is disfavored for all the possible combinations of mass ordering and θ_{23} octant.

1.1.4 Mass Ordering

As anticipated before, neutrino oscillation experiments are only able to measure the squared mass difference between two different mass eigenstates: $\Delta m_{ij}^2 = m_i^2 - m_j^2$ with $i, j = 1, 2, 3$. In the existing model there are only two independent neutrino squared mass differences commonly referred as Δm_{21}^2 and Δm_{31}^2. From neutrino oscillation experiments, only Δm_{21}^2 and $|\Delta m_{31}^2|$ are known. This allows two different spectra of neutrino

masses based on the sign of Δm_{31}^2:

- spectrum with normal ordering (NO):

$$m_1 < \ m_2 < m_3 \tag{1.46}$$
$$\Delta m_{31}^2 > 0 \tag{1.47}$$
$$\Delta m_{21}^2 > 0 \tag{1.48}$$

- spectrum with inverted ordering (IO):

$$m_3 < \ m_1 < m_2 \tag{1.49}$$
$$\Delta m_{31}^2 < 0 \tag{1.50}$$
$$\Delta m_{21}^2 > 0 \tag{1.51}$$

The two different ordering options are shown in Fig. 1.9. At present time it is not known whether the ν_3 is heavier or lighter than ν_1 and ν_2. The two different spectra generate huge differences on the neutrino models. Therefore, the mass ordering is one of the prime model discriminator for the neutrino physics.
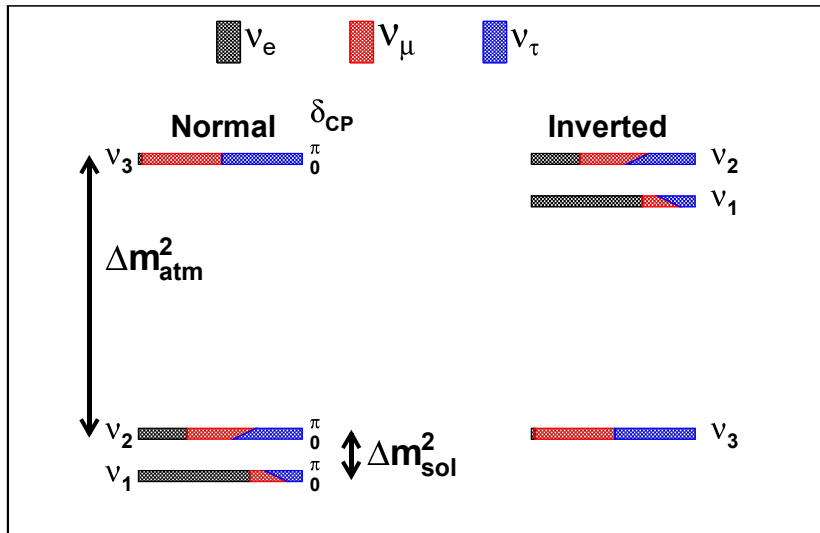
Figure 1.9: Pattern of neutrino masses for the normal and inverted ordering. Flavor composition of the mass eigenstates is shown with different colors as the function of the CP phase δ_C.

The best way to experimentally determine the mass ordering is using the matter effect that happen when neutrinos travel in a medium. Recalling equation (1.29), one

can determine the matrix (1.30) to describe the two flavor oscillation case described in Section 1.1.2[7]:

$$\mathcal{H}_F = \frac{1}{4E} \begin{bmatrix} -\Delta m^2 \cos 2\theta + A_{CC} & \Delta m^2 \sin 2\theta \\ \Delta m^2 \sin 2\theta & \Delta m^2 \cos 2\theta - A_{CC} \end{bmatrix}, \tag{1.52}$$

where $\Delta m^2 \equiv m_2^2 - m_1^2$ and θ is the mixing angle of Eq. (1.21). From this matrix, one can obtain the relation between the vacuum and the matter parameters of the oscillation as follow[21]:

$$\Delta m_{mat}^2 = \Delta m_{vac}^2 \xi, \qquad \sin 2\theta_{mat} = \frac{\sin 2\theta_{vac}}{\xi} \tag{1.53}$$

$$\xi = \sqrt{(\cos 2_{vac} - \hat{A})^2 + \sin^2 2\theta_{vac}} \tag{1.54}$$

with

$$\hat{A} = \pm \frac{A_{CC}}{\Delta m^2} = \pm \frac{2\sqrt{2}EG_F N_e}{\Delta m^2} \tag{1.55}$$

the matter potential. In Eq. (1.55) there is a dependency on the particle being a neutrino (+) or an anti-neutrino (-) and on the sign of the Δm^2. Since ξ in (1.53) vanishes for short distances, matter effect may be used to solve the problem of the mass ordering in two ways. The first is to use an accelerator neutrino source and study the appearance of a new type of neutrino at a long distance, with ν_μ as source and ν_e as new flavor as the most used configuration. Alternatively one can use atmospheric neutrinos exposed to the matter effect by their propagation through the Earth.

The matter effect could determine the neutrino mass ordering studying the appearance of electron neutrinos in a beam of muon neutrinos. Equation (1.55)) shows that replacing neutrinos with antineutrino, the sign of δ_{CP} and of the matter effect are reversed. Selecting a precise value of L/E_ν, knowing the values of the mixing angles, it is possible to disentangle the CP violation and the matter effect from the sign of the mass difference, allowing to define the correct neutrino mass ordering (Fig. 1.10).

The present global fit obtained from long-baseline experiments (NOνA, MINOS, T2K), reactor neutrino experiments (Daya Bay, RENO, Double Chooz) and solar neutrino experiments (SNO, Super-Kamiokande, Borexino), shows a growing significance toward the normal mass ordering. As can be seen in Fig. 1.11, 1.12, 1.13, there is a difference in the χ^2 that favors normal mass ordering. This difference varies from one experiment to another but the variation can be traced back to a slight difference in the determination of the δ_{CP} for the normal ordering. The results of all the experiments combined show a $\Delta\chi^2$ of about 2.

Another hint for the preference of the normal mass ordering can be seen in Fig. 1.13, where the results from the above mentioned experiments are shown. This results are further enhanced by atmospheric neutrino data coming from Super-Kamiokande and
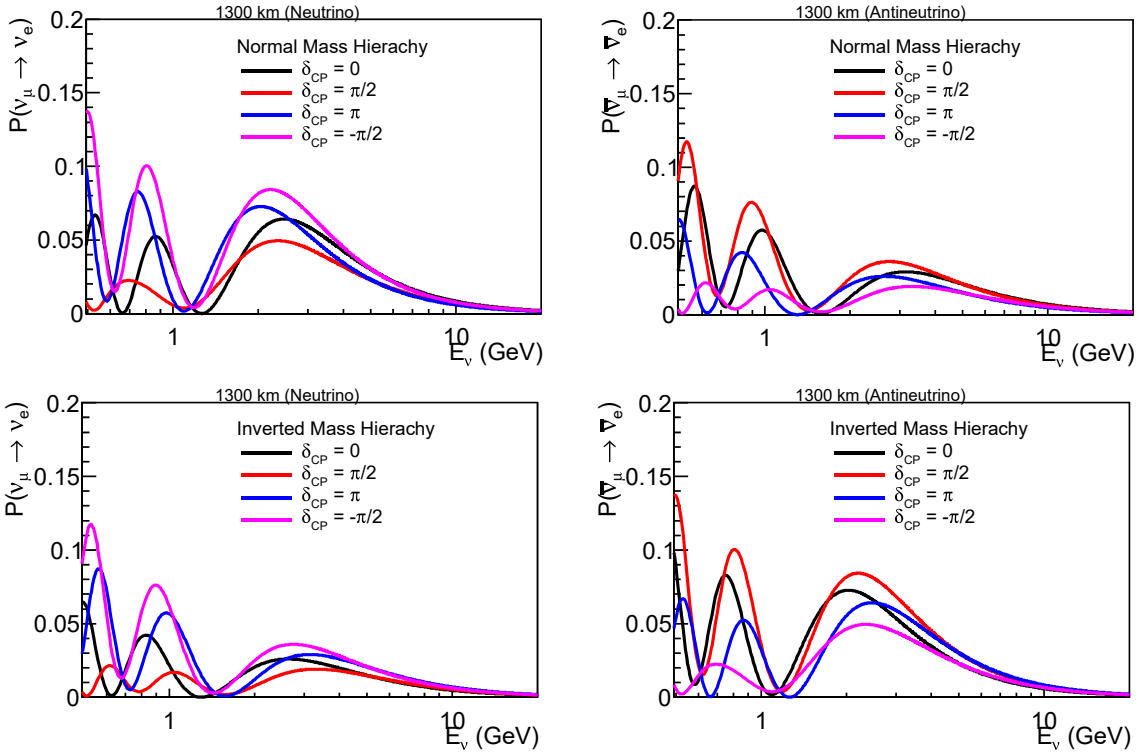
Figure 1.10: Electron neutrino and antineutrino appearance probabilities as a function of the neutrino energy at L = 1300 km for different values of δ_{CP}[22].

IceCube. While the contribution of Deep-Core of IceCube is very marginal, as can be seen in Fig. 1.14, the result obtained by Super-Kamiokande has a big impact in the χ^2 information as it increases by almost 5 units, from 4.7 to 9.3. The final results are showed in Fig. 1.15[23], where the contribution of Super-Kamiokande is more clear.

1.2 Pending Questions

As shown in the previous sections, there is a big effort in the understanding of neutrino physics. In the last years a lot of progress has been made in our understanding of neutrino oscillations, but many questions are still unanswered. The high precision measurements of the $\sin^2 2\theta_{13}$ and θ_{13}, discussed in Section 1.1.2, have big implications and opened up new possibilities in the neutrino physics research. Some of the most crucial goals of this research include:

- Determination of the sign of Δm_{31}^2 to solve the problem of the neutrino mass
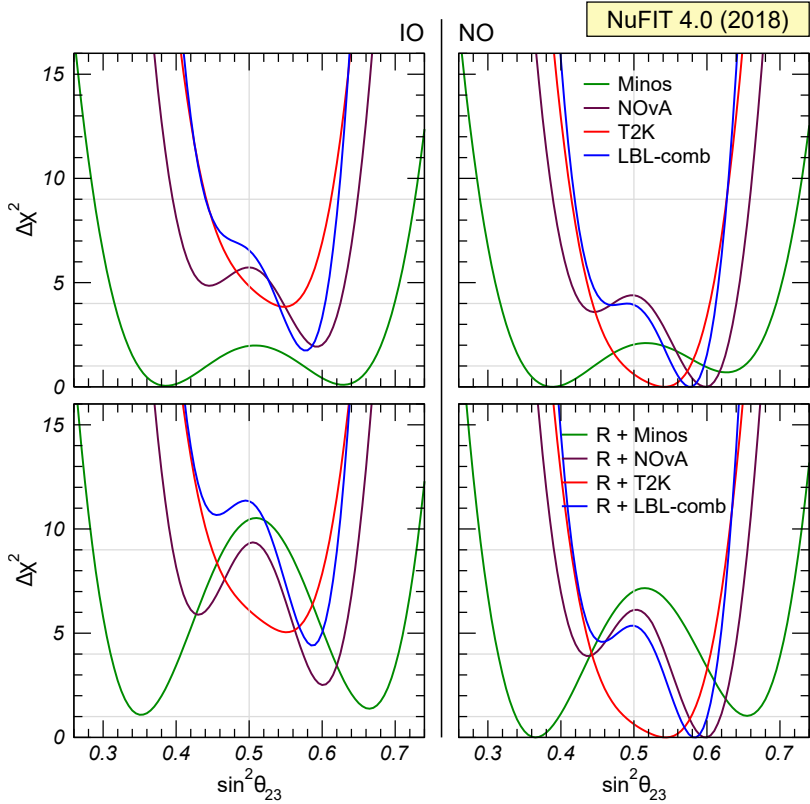
Figure 1.11: Result of the determination of θ_{23} from long-baseline, reactor and their combination. The upper panels show the $\Delta\chi^2$ from LBL experiments after constraining only θ_{13} from reactor experiments. The lower panels show the same results using all the information from LBL and reactor experiments combined. In all panel Δm^2_{21}, $\sin^2\theta_{12}$ are fixed to the global best fit values.

  ordering;

- Measurement of the δ_{CP} in the leptonic sector;

which can be studied with neutrino oscillations experiments, but also:

- Determination of the nature of massive neutrinos (Dirac or Majorana);

- Measurement of the absolute scale of neutrino mass,

which instead can be studied with different types of experiments, like the neutrinoless double beta decay experiments. Because of this, new and upgraded experiments aim to better measure the already known parameters and to answer the open questions of neutrinos. To allow such extensive research program, new experiments in every field of neutrino physics - long-baseline, atmospheric, reactor - are needed.
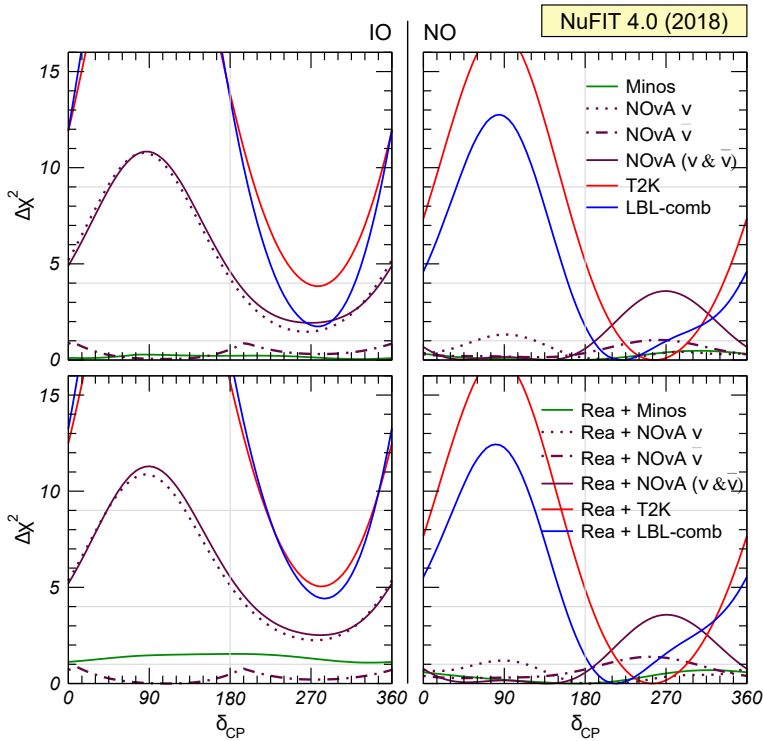
Figure 1.12: Result of the determination of δ_{CP} from long-baseline, reactor and their combination. The upper panels show the $\Delta\chi^2$ from LBL experiments after constraining only θ_{13} from reactor experiments. The lower panels show the same results using all the information from LBL and reactor experiments combined. In all panel Δm_{21}^2, $\sin^2\theta_{12}$ are fixed to the global best fit values.

In the long-baseline domain, the Deep Underground Neutrino Experiment (DUNE) will be a next-generation neutrino oscillation experiment which will try, among other things, to solve the first two goals of the ones listed above. It will be described in details in the next chapter.
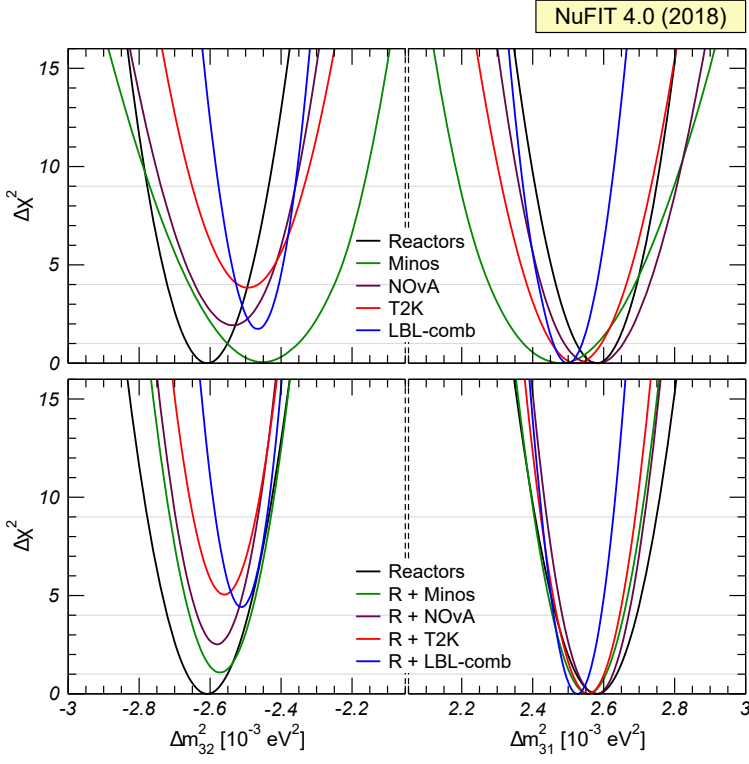
Figure 1.13: Result of the determination of Δm^2 from long-baseline, reactor and their combination. The upper panels show the $\Delta \chi^2$ from LBL experiments after constraining only θ_{13} from reactor experiments. The lower panels show the same results using all the information from LBL and reactor experiments combined. In all panel Δm^2_{21}, $\sin^2 \theta_{12}$ are fixed to the global best fit values.
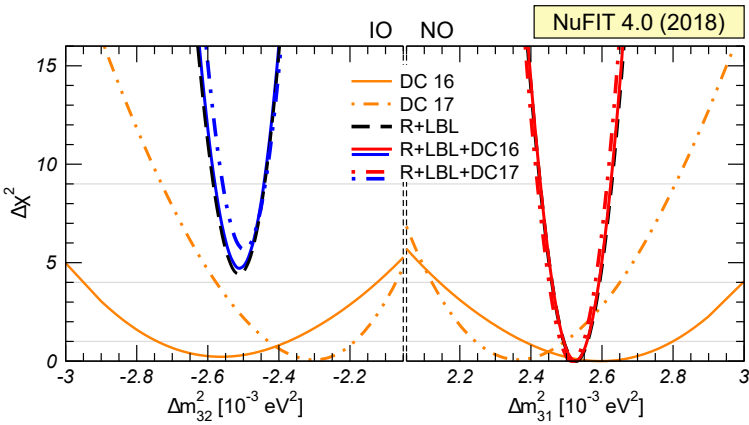
Figure 1.14: $\Delta \chi^2$ as a function of Δm^2_{3l} for the analysis of Deep-Core 3-years data (orange line) and its combination with the global analysis (red and blue lines).
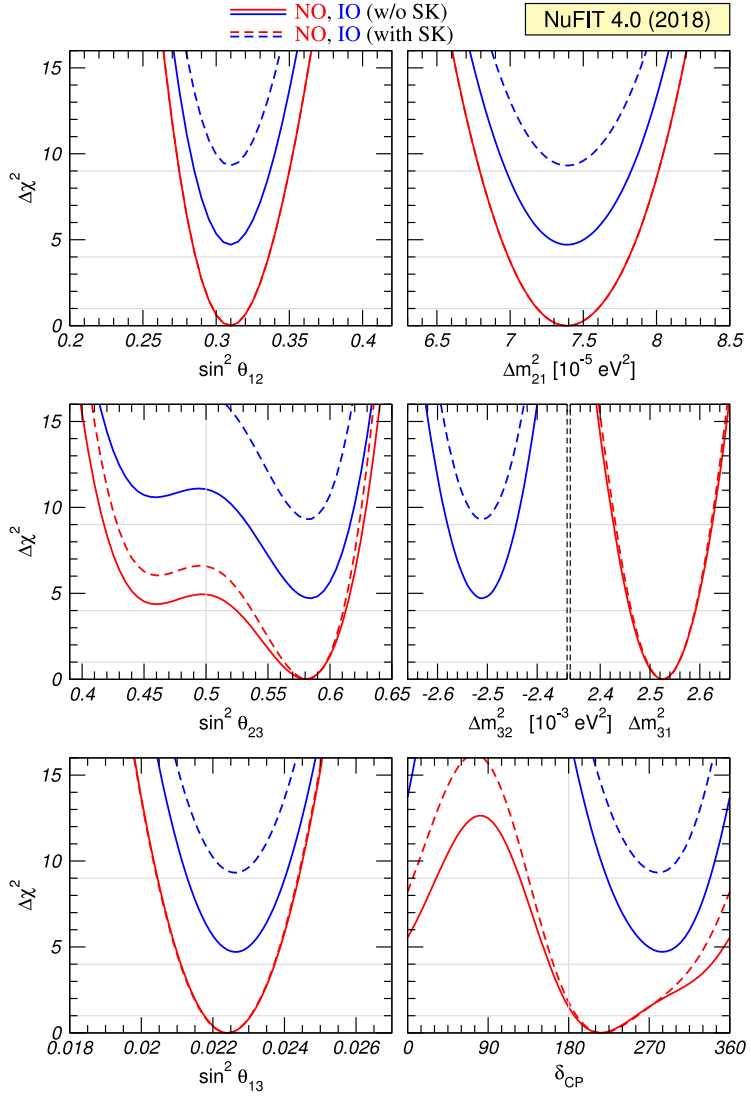
Figure 1.15: Global three-neutrino oscillation analysis. In red the result corresponding to Normal Ordering, in blue the ones corresponding to the Inverted Ordering. The dashed line are the result considering the data from Super-Kamiokande. The $\Delta\chi^2$ is minimized with respect to all the undisplayed parameters.

26

Chapter 2

The DUNE experiment

The Deep Underground Neutrino Experiment (DUNE) will be an experiment aiming to study different aspect of neutrino physics. DUNE will be composed by two detectors at two experimental sites. The first at Fermilab, where the facility required to support this experiment (LBNF) and a high precision Near Detector (ND) will be hosted. The second at the Stanford Underground Research Facility (SURF), 1300 km away from the neutrino source, where the Far Detector (FD) will be installed ~ 1500 m underground.

2.1 DUNE's physics

As anticipated in the previous Chapter, the studies of neutrino physics will be able to provide answers to some still open fundamental questions. To answers these questions, DUNE will study neutrino and astroparticles physics, trying to probe new regions of parameter space for both the accelerator-based and astrophysical frontiers.

Some of the fundamental questions that DUNE aim to solve are the following:

- Why is there asymmetry between matter and antimatter in the Universe? It is clear that matter dominates over antimatter in the Universe despite being equally created in the Big Bang. DUNE will try to determine the CP violation in the leptonic sector through the study of neutrino oscillations as this is the current most promising avenue for understanding this asymmetry.

- Are there other fundamental symmetries? Despite the existence of a mixing in both the quark and the neutrino sector, the pattern of mixing and masses are very different. Precise measurements of the neutrino mixing could reveal new symmetries of the Universe.

- What new physics is possible to learn from neutrino burst and supernova explosion? DUNE will be able to reveal neutrinos generated in possible core-collapse supernova

in our galaxy. Measurements of neutrinos generated this way will be critical for understanding the dynamics of this important astrophysical phenomenon.

- Is there a Grand Unified Theory? It is supposed that the force observed today were originally unified in one force. Grand Unified Theories (GUTs) that attempt to describe this unification predict the possibility of the proton to decay. DUNE will search such decay in a range of lifetime predicted by a large number of GUT models.

To address all of these questions, DUNE will pursuit a long-term scientific program categorized into different branches: *primary* science program and *ancillary* science program.

The primary science program of DUNE aims to investigate the fundamental questions in neutrino physics that were described in the previous chapter: the measurement of the CP violating phase δ_{CP}; the determination of the neutrino mass ordering; as well as precision test of the three-flavor neutrino oscillation model, with the measurement of the θ_{23} angle. These objectives will be carried on through the precise measurements of the parameters involved in the $\nu_\mu \rightarrow \nu_e$ and $\bar{\nu}_\mu \rightarrow \bar{\nu}_e$ oscillations. In addition to this measurements, DUNE will search for proton decay in many important decay channels, allowing a ground-breaking discovery if one of those decay is observed. Finally, the detection and measurements of the neutrino flux coming from core-collapse supernova are also part of the primary program.

The design of the DUNE detector, both at the Near and at the Far Detector, will permit a rich research program beyond the main objectives of the experiment already mentioned: the ancillary program. Exploiting the massive target of the FD it is possible to measure the neutrino mixing parameters using atmospheric neutrinos and search for signals of new neutrinos states and interaction. Moreover, the high precision of the ND will make possible a wide range of measurements, like neutrino interaction's cross sections, nuclear effects and final states.

2.1.1 Long-baseline neutrino oscillation physics

One of the main strength of DUNE is that, thanks to the 1300 km baseline, the experiment is sensitive to the matter effect. As described in Section 1.1.4, the matter effect causes an asymmetry in the $\nu_\mu \rightarrow \nu_e$ versus $\bar{\nu}_\mu \rightarrow \bar{\nu}_e$ oscillation probabilities. In Fig. 2.1 are shown the asymmetries in the neutrino oscillations generated separately by the matter effect and CP violation ($\delta_{CP} = \pm\pi/2$). The asymmetry's dependence can be approximated as follow:

$$\mathcal{A}_{CP} \propto L/E \tag{2.1}$$

$$\mathcal{A}_{matter} \propto L \times E \tag{2.2}$$
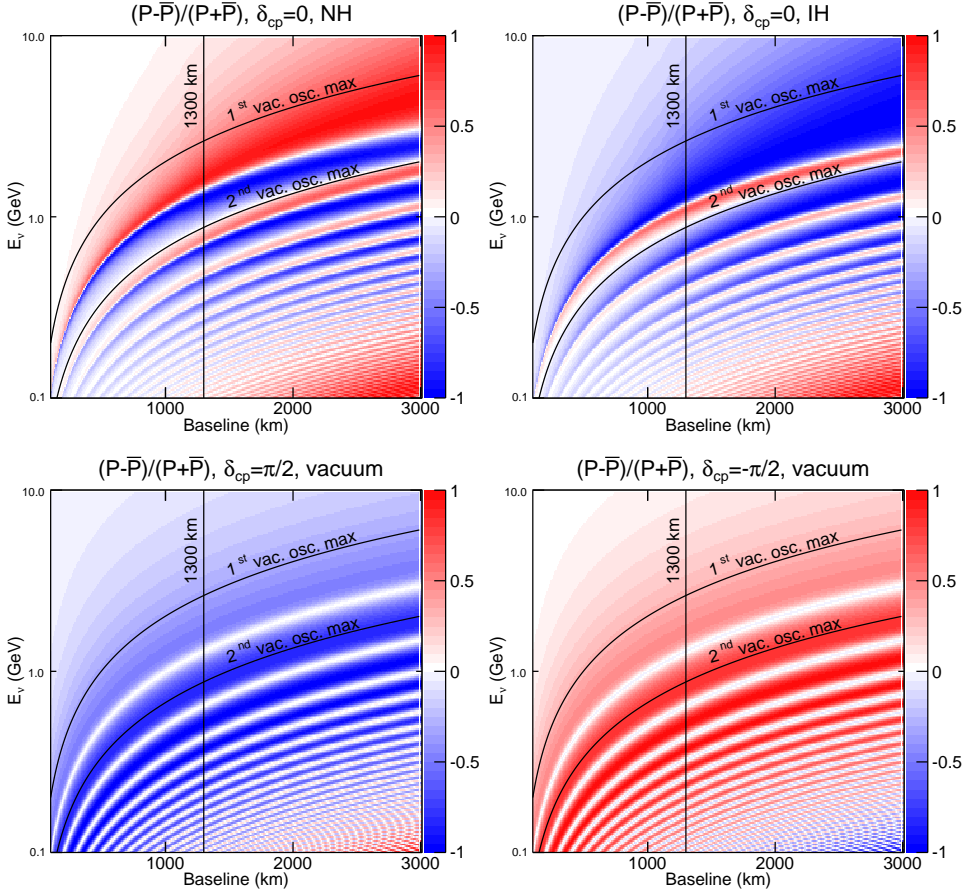
Figure 2.1: $\nu/\bar{\nu}$ oscillation probabilities asymmetries as a function of energy and baseline. Top row shows the effect of the matter effect for normal (left) and inverted (right) mass ordering. Bottom row shows the effect of the CP-violation phase δ_{CP} in vacuum for $\delta_{CP} = +\pi/2$ (left) and $\delta_{CP} = -\pi/2$ (right)[24].

It is clear then that a baseline of several hundreds kilometers is needed to make the matter asymmetry significant. The knowledge of the mixing parameters allows the estimation of the matter asymmetry magnitude but leaves unknown the sign of it, making possible to know a priori the needed baseline to separate the effect of CP and matter asymmetries.

The DUNE baseline makes possible to have an asymmetry of approximately $\pm 40\%$[24], a value larger than the maximum possible asymmetry associated with δ_{CP}, and makes possible to determine unambiguously both the mass ordering and the CP-violation asymmetry. The need of a long baseline is clearly visible in Fig. 2.2, where the asymmetry in (1.44) as a function of δ_{CP} is showed. Indeed, a short baseline could cause an ambiguous results in regions in which the matter and CP asymmetries cancel each others. The top row of Fig. 2.2 shows that the value of δ_{CP} is ambiguous if the mass ordering is unknown

while longer baselines allow the discrimination of both the phase value and the mass ordering.
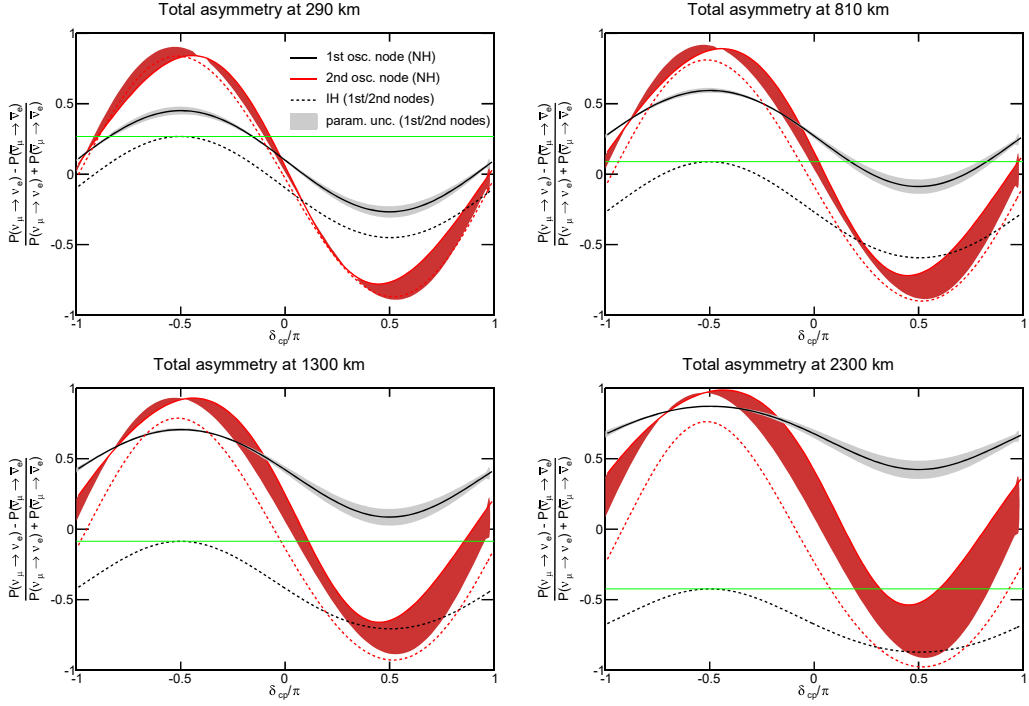
Figure 2.2: Oscillation probability asymmetries as a function of δ_{CP} for different baselines. The solid and dashed black lines are the total asymmetries for the normal and inverted orderings at the first node respectively. The red lines are the asymmetries at the second node[24].

Mass Ordering and CP violation measurements The sensitivities to Mass Ordering (MO) and CO violation measurements are obtained fitting the simulated $\nu_\mu \to \nu_\mu$, $\bar{\nu}_\mu \to \bar{\nu}_\mu$, $\nu_\mu \to \nu_e$, $\bar{\nu}_\mu \to \bar{\nu}_e$ spectra at the same time. The sensitivities are then quantified using $\Delta\chi^2$ parameters defined for MO and CP as follows:

$$\Delta\chi^2_{MO} = |\chi^2_{MO^{test}=IH} - \chi^2_{MO^{test}=NH}| \tag{2.3}$$

$$\Delta\chi^2_{CPV} = min(\Delta\chi^2_{CP}(\delta^{test}_{CP} = 0), \Delta\chi^2_{CP}(\delta^{test}_{CP} = \pi)) \tag{2.4}$$

where $\Delta\chi^2_{CP} = \chi^2_{\delta^{test}_{CP}} - \chi^2_{\delta^{true}_{CP}}$.

For what concerns the MO, DUNE aims to determine the correct ordering with a significance of at least $\sqrt{\Delta\chi^2} = 5$ for every value of δ_{CP}. In Fig. 2.3 it is shown the significance reachable by DUNE as a function of the exposure - defined as kilotonnes of active volume $\times$ megawatts of beam's power $\times$ years. Approximately 200 to 400 kt $\cdot$

MW · years of exposure are needed to obtain the required significance for all the values of δ_{CP}. Figure 2.4 shows the significance with which the MO can be determined as a
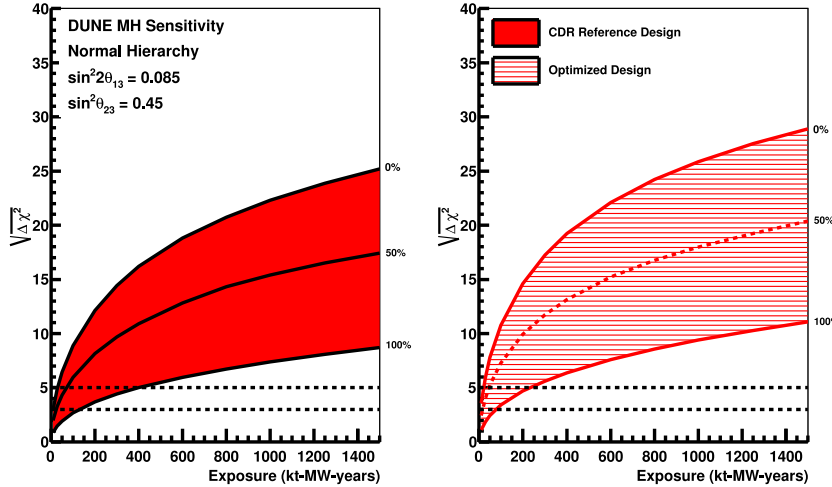
Figure 2.3: Mass ordering's significance as a function of exposure for 100%, 50% and 0% values of δ_{CP}. Normal mass hierarchy is assumed[25].
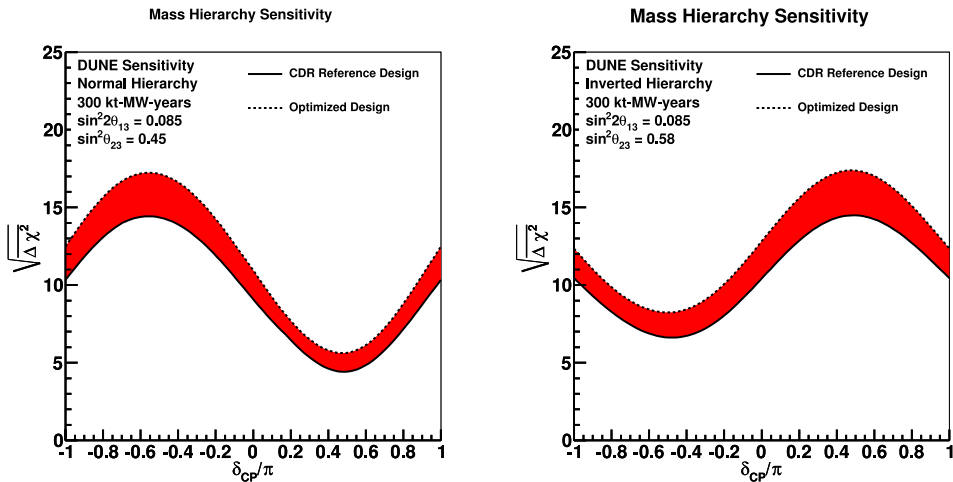

Figure 2.4: Mass ordering significance as a function of δ_{CP} for an exposure of 300 kt · MW · years. The red band is due to different design of the beam[25].

function of the value of δ_{CP} with an exposure corresponding to seven years of data (300 kt · MW · years) while Fig. 2.5 shows how the significance is influenced by the values of different mixing parameters.

In addition to MO, DUNE aim to measure the CP-violation in the leptonic sector. Differently from the MO determination, the significance of a CP violation measurement

31
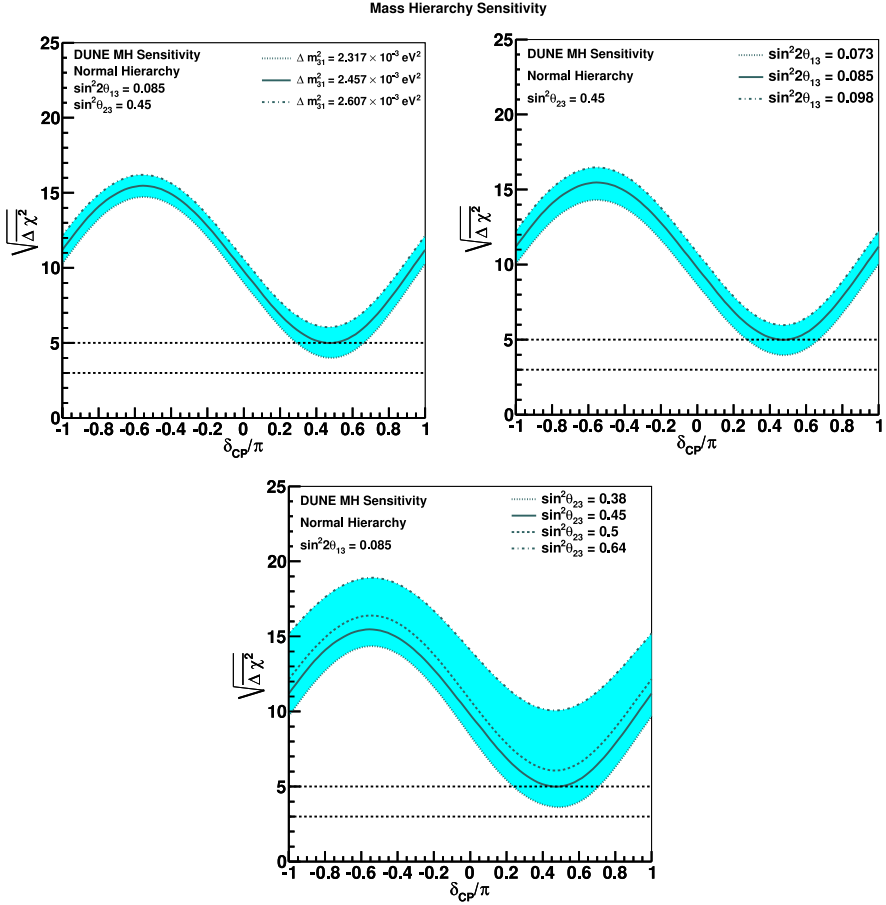
Figure 2.5: Variation of the MO sensitivity due to different values of Δm_{31}^2 (Upper left), θ_{13} (upper right) and θ_{23} as a function of different values of δ_{CP}. The solid line in each panel indicates the nominal value for each parameter able to provide a significance of at least $\sqrt{\Delta\chi^2} = 5$ for all the values of δ_{CP}[25].

cannot be granted to be higher than a minimum value for all the values of δ_{CP}. This arises from the definition of the CP asymmetry in Eq. (1.44): for $\delta_{CP} = 0$ and π, the CP violation effect vanishes and the significance of the measurements drops to zero. This effect is clear in Fig. 2.6, where a double peak structure is present in the plot of the significance for the determination of the CP violation as a function of the value of δ_{CP}, for an exposure of 300 kt · MW · year.
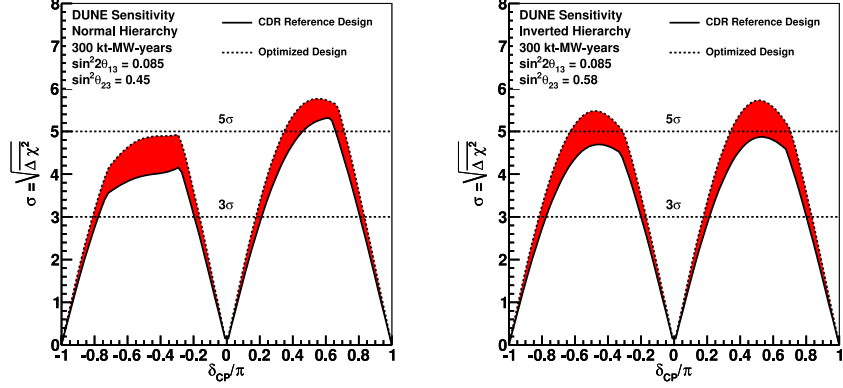
Figure 2.6: CP violations' significance as a function of δ_{CP} for an exposure of 300 kt $\cdot$ MW $\cdot$ years. The red band is due to different design of the beam[25].
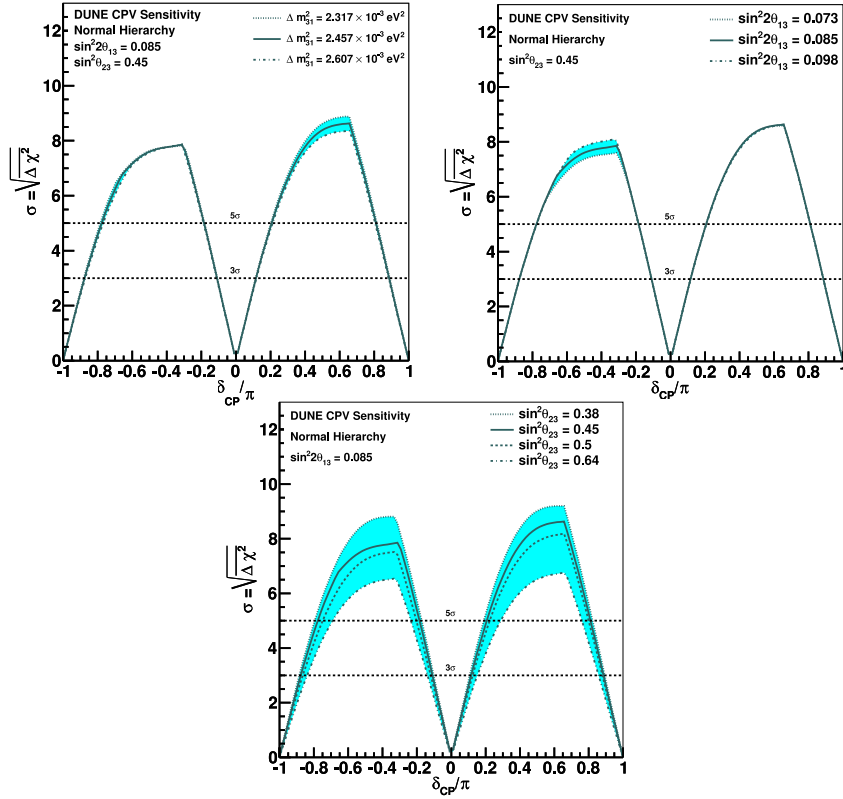
Figure 2.7: Variation of the CP violation sensitivity due to different values of Δm_{31}^2 (Upper left), θ_{13} (upper right) and θ_{23} as a function of different values of δ_{CP}. The solid line in each panel indicate the nominal value for each parameter able to provide a significance of at least $\sqrt{\Delta \chi^2} = 3$ for 75% $of \delta_{CP}$ values[25].

As for the MO determination, Fig. 2.7 shows how different values of θ_{23}, θ_{13} and Δm^2_{31} cause a variation in the sensitivity of the CP violation. It is clear, specifically watching the variation of the significance due to different values of θ_{23}, that precision measurements of all the parameters involved in the neutrino oscillation need to be performed, as their values can have a big impact in both the MO's and CP violation significance.

Oscillation Parameters Measurements and test of the three-flavor model As showed in Fig. 2.5 and 2.7, the exact value of the oscillation parameters can cause big variations in the sensitivity to CP violation and MO determination. Moreover, higher-precision measurements of these parameters can be used to improve sensitivity to models beyond the three-neutrino framework. The LArTPC used in DUNE will provide excellent particle identification capability and it will be possible to measure all the parameters involved in the $\nu_1 - \nu_2$ and $\nu_2 - \nu_3$ mixing: $\sin^2 \theta_{23}$ and the octant of θ_{23}, δ_{CP}, $\sin^2 2\theta_{13}$ and Δm^2_{31}. One of the objectives of the experiment will be to reach a resolution on the measure of such parameters comparable to the one of other experiments planned in the next years. Figure 2.8 shows the expected resolution on the different parameters that DUNE will measure as a function of the exposure.

Beside the measurements of the parameters in the three-neutrino framework, DUNE should provide high sensitivity to new physics phenomena, like nonstandard interactions in matter or sterile neutrino states; which would imply a very small perturbation in the neutrino oscillations.

2.1.2   Atmospheric Neutrinos

Thanks to the large mass of the Far Detector and the $\sim$1500 meters of soil above it, DUNE should be an ideal site to study neutrino oscillations using atmospheric neutrinos. This measurements will be complementary to the one performed with the neutrino beam and because of the wide range of L/E of atmospheric neutrinos, all the mixing parameters could be measured.

Figure 2.9 shows the sensitivity to the MO discrimination as a function of the exposure with atmospheric neutrinos. The sensitivity goes like the square root of the exposure, meaning that it is not limited by the systematic uncertainty. This, together with the fact that the MO sensitivity with atmospheric neutrinos is almost independent on CP-violation and strongly dependent on the exact value of $\sin^2 2\theta_{23}$, will provide an additional measurement to solve the ambiguity of the θ_{23} octant.
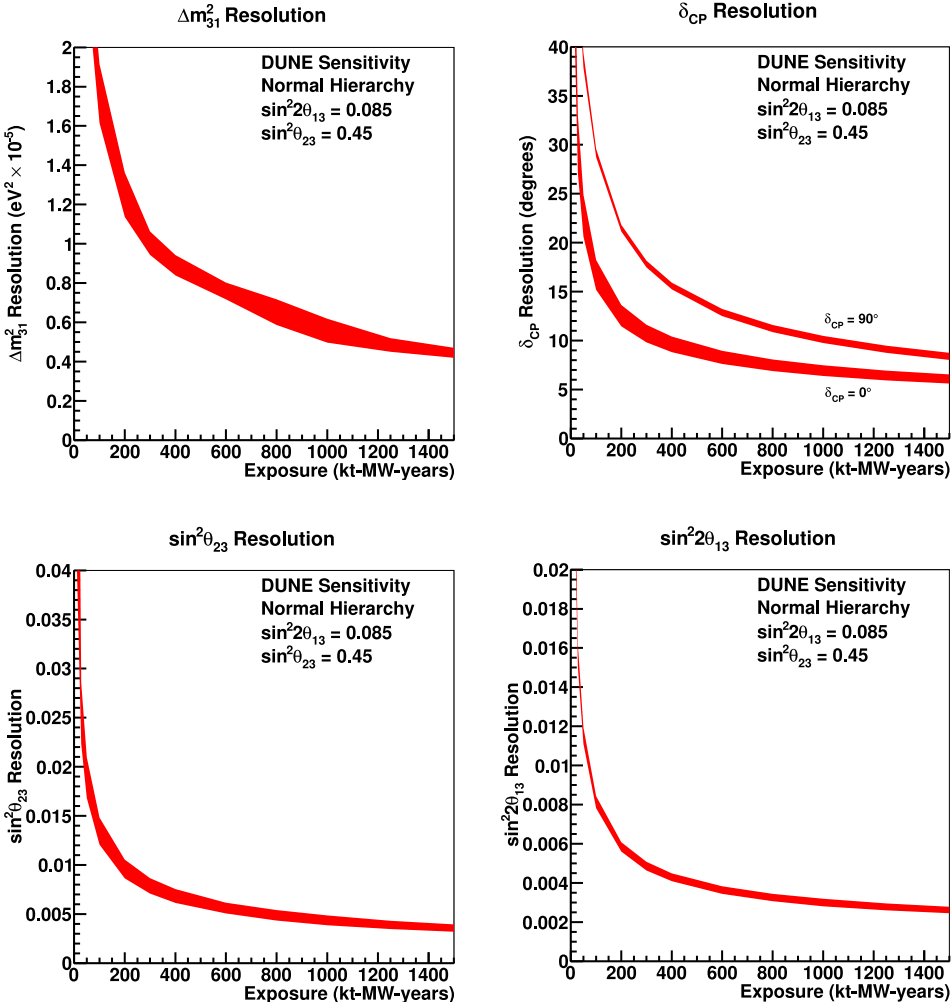
Figure 2.8: Resolution of a measurements of Δm_{31}^2 (upper left), δ_{CP} (upper right), $\sin^2 \theta_{23}$ (bottom left) and $\sin^2 2\theta_{13}$ (bottom right) as a function of the exposure. The red region is related to the change in sensitivity for different beam designs[25].

2.1.3 Near Detector Physics

Systematic uncertainties in the measurements of neutrino oscillations can imply substantial degradation in the sensitivity to both the CP-violation and mass ordering. To achieve the required precision in the Far Detector, it is necessary to characterize the expected unoscillated neutrino flux with high precision. Neutrino fluxes, energy and shape composition have to be known and, at the same time, characterization of the neutrino interaction and cross section on liquid argon should be studied to estimate the systematic in the oscillation measurements. The Near Detector will perform all these measurements to allow the flux extrapolation to the FD and to constrain the systematic uncertainties
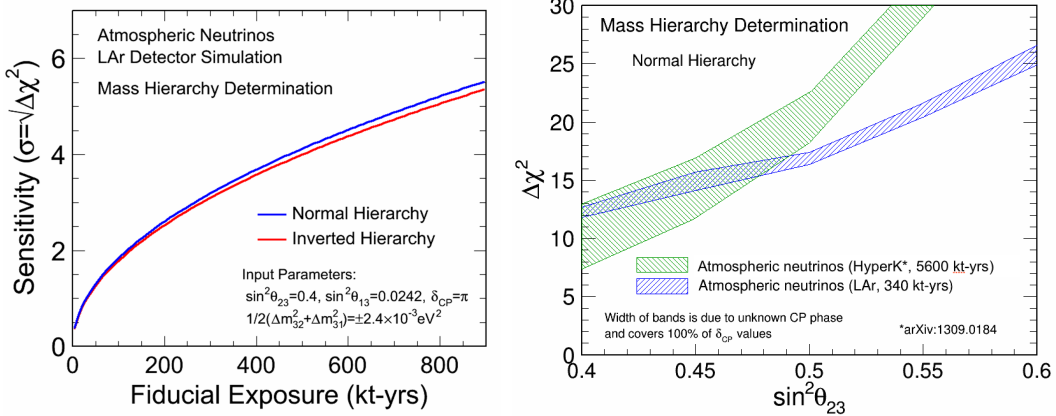
Figure 2.9: Mass Ordering sensitivity as a function of exposure (left) and of the real value of θ_{23} (right) using atmospheric neutrinos. For comparison the Hyper-K sensitivities from [26] are also shown.

under the required level.

Precision Measurements Related to Oscillation Physics One of the method to determine the ν_μ and $\bar{\nu}_\mu$ flux is measuring the CC event in which the hadronic-energy deposition - the difference between the energy of the incident neutrino and the energy of the lepton produced in the interaction - in small. To do so it is possible to count the number of CC events below a certain hadronic energy. The total events count is then, up to some correction, proportional to the relative flux:

$$\mathcal{A}(\nu < \nu_0) \simeq C\Phi(E_\nu)\nu_0 \left[\mathcal{A} + \left(\frac{\nu_0}{E_\nu}\right)\mathcal{B} + \left(\frac{\nu_0}{E_\nu}\right)^2 \mathcal{C} + \mathcal{O}\left(\frac{\nu_0}{E_\nu}\right)^3 \right] \tag{2.5}$$

where ν_0 is the maximal value of hadronic energy taken in account for the measurement of the relative flux at certain energy. This method permits the reconstruction of the flux for neutrino with energy spanning from 1 to 50 GeV with a precision $\leq 2\%$.

Beside the relative flux, an important prediction that the ND will perform is the composition, in terms of neutrino flavor, of the beam. Measuring the CC interaction of the ν_{μ^-}, $\bar{\nu}_{\mu^-}$, ν_{e^-} and $\bar{\nu}_{e^-}$ is essential for the systematics on $\nu_\mu \to \nu_e$ and $\bar{\nu}_\mu \to \bar{\nu}_e$ oscillation measurements, and to this extend the ND will have high tracking capability in a magnetic field, allowing a precise extrapolation of the different component of the flux to the FD. Finally, the ND will have to perform all the measurements needed for the evaluation of the neutrino-Argon cross section and the characterization of other interaction channels, such as resonance, deep-inelastic- and quasi-elastic-scattering. This requirements suggest the need of a high resolution detector, whose design will be discussed in a next section, that can be exploited not only for precision oscillation studies but also to search for new physics like heavy neutrinos and dark matter candidates.

New Physics Search   Thanks to the baseline of some hundred meters of the Near Detector and the mean neutrino beam energy, the ratio L/E will have a value of about 1. This has the important consequence of making the ND sensitive to possible neutrino oscillations with large Δm^2. Different experiments have already pointed toward the existence of these so called sterile neutrinos, which mass should be in the 1 eV^2 range. The Near Detector thus, should be able to study these neutrinos.

The Near Detector of DUNE will also search for WIMP-like candidates. To do so, since the signature of the DM will look like the one of neutrinos, the neutrino beam will be the biggest background source. One way to distinguish neutrino and dark matter could be the fact that dark matter's particles, due to the bigger mass, travel slower than neutrinos. With a fine timing, the ND could then be able to distinguish DM signature from neutrinos. Thanks to the fine angular resolution of the detector, one could use also information of the direction of electron struck by DM particles, that will be in a much forward direction compared with the one produced by neutrinos.

2.2   Neutrino Beam

To fulfill the physics program of DUNE, a neutrino beam of sufficient intensity and appropriate energy range is needed.

The neutrino beam for the DUNE experiment will be produced at Fermilab and the design, sketched in Fig. 2.10, is a conventional horn-focused, sign selected neutrino beam. This design uses an accelerated proton beam produced in the Fermilab Main Injector that is left to impinge on a fixed target. The secondary particles produced in the strike of the protons, mainly $\pi^\pm, K^\pm$, are focused using the horns by means of magnetic fields and left to decay in a decay pipe. An absorber at the end of such pipe removes the hadrons still in the beam leaving only neutrinos. Using the magnetic field polarity of the horns allows to focus only positive (or negative) particles, allowing to produce a beam of neutrinos (or antineutrinos) only with a small contamination of ν_e and $\bar{\nu}_e$. The beam composition is of fundamental importance for the studies that the DUNE experiment will performs. The beam characteristics are reported in Table 2.1.

The horns will select a range of neutrino energies between 0.5 and 5 GeV. This energetic range will cover the first two oscillation maximum described in the previous section[24]. In Fig. 2.11 the unoscillated fluxes of neutrinos and antineutrinos expected with the 120 GeV proton beam are shown.

2.3   The DUNE detectors

The dual site configuration of the DUNE experiment and the different types of measurements performed in each site make the choice of the detector and the physics requirements
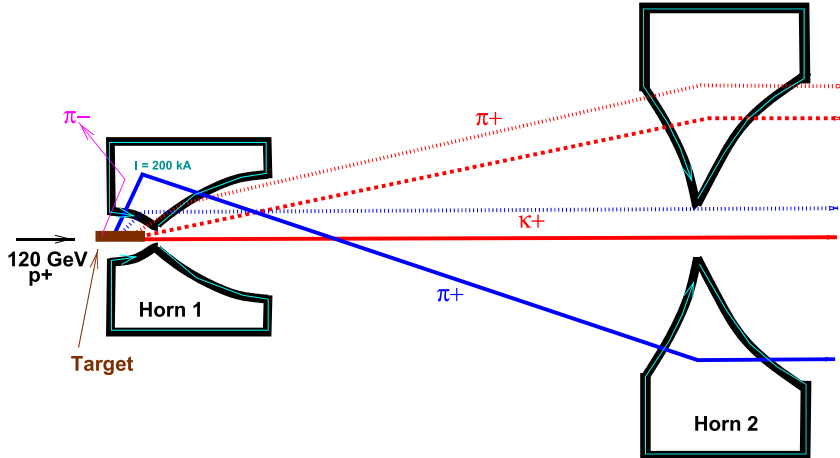
Figure 2.10: Scheme of functioning of the horns when focusing positive particles[27].

	Beam's parametesr	
Energy	60 GeV	120 GeV
Protons per cycle	7.5×10^{13}	7.5×10^{13}
Spill duration (s)	1.0×10^{-5}	1.0×10^{-5}
Protons on target per years	1.9×10^{21}	1.1×10^{21}
Beam Power	1.03 MW	1.2 MW

Table 2.1: Expected beam design parameters for two primary proton beam momenta[25].

for the near and far site very different.

2.3.1 Far detector

The Far Detector will be built about 1500 meters underground and will be composed by four Liquid Argon Time Projection Chamber (LArTPC). This technology is able to provide the needed tracking and calorimeter's capability to perform the measurement of neutrino oscillations over a wide range of energies. The design of each single module of the Far Detector consists of a 10-kt, single-phase or/and dual-phase LArTPC in which the generation, drift and collection of the charge is performed completely in liquid argon. To do so, different components are needed:

- Time Projection Chamber (TPC)

- Data Acquisition System (DAQ)

38
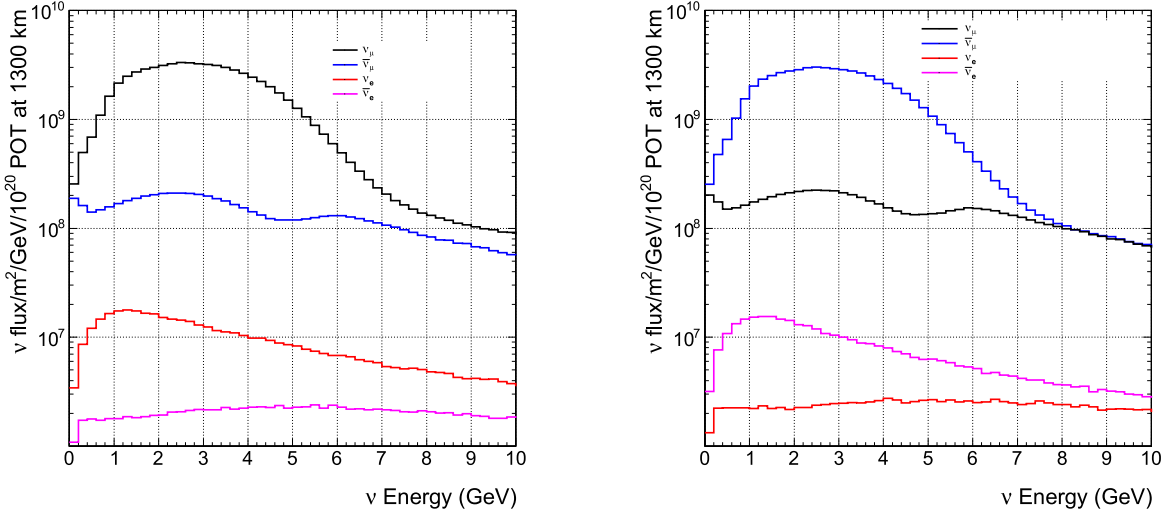
Figure 2.11: Unoscillated neutrino fluxes at the Far Detector as a function of energy with horn focusing negative particles (left) and positive particles (right).

- Cold Electronics (CE)

- Photon Detector System (PD).

The expected performance of the Far Detector, needed to meet the minimum requirements to fulfill the physics goals described in the previous section, is based on Monte Carlo simulations and on the performance of similar detectors. Table 2.2 is a summary of the needed performances of the Far Detector while Fig. 2.12 shows a representation of it.

The Time Projection Chamber

The TPC is the active part of the far detector modules. It is 12 m high, 14.5 m wide and 58 m long along the beam direction and it is submerged in liquid argon at 88 K. Neutrino interaction in the active volume produces both the ionization of the liquid argon atoms and the emission of scintillation light. The scintillation light is detected by the Photon Detector and it is used to provide the timing of the events. The electrons produced with the ionization will instead drift toward an anode plane thanks to a uniform electric field and produce a current-signal. Both the timing and the current signal are then used to reconstruct the event.

To create the required electric field in the volume of liquid argon, different anode (APA) and cathode (CPA) planes are assembled along the length of the detector. There are a total of three rows of APA alternate with two rows of CPA, as showed in Fig. 2.13. With this configuration, the maximum drift distance of an electron is 3.6 m. Since the

Parameter	Requirement	Expected Performance
Signal/Noise Ratio	9:1	9:1
Electron Lifetime	3 ms	> 3 ms
Uncertainty on Charge Loss due to Lifetime	$< 5\%$	$< 1\%$
Vertex Position Resolution	(2.5, 2.5, 2.5) cm	(1.1 1.4, 1.7) cm
$e - \gamma$ separation γ rejection	>0.9	0.99
Multiple Scattering Resolution on muon momentum	$\sim 18\%$	$\sim 18\%$
Electron Energy Resolution	$0.15/\sqrt{E \text{ (MeV)}} \oplus 1\%$	From Prototype
Energy Resolution for Stopping Hadrons	$< 10\%$	From Prototype

Table 2.2: Summary of the requirement and expected performance for some of the most important parameters of the DUNE Far Detector[28].
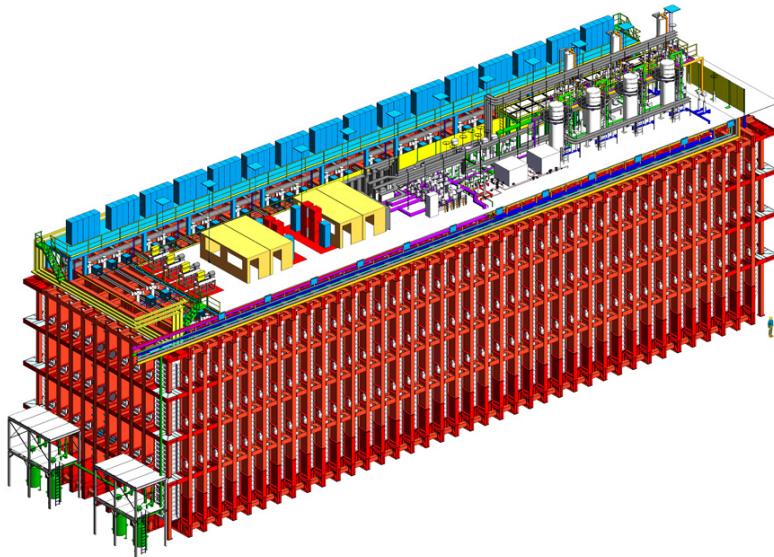
Figure 2.12: Illustration of one of the four modules that will compose the Far Detector.

electron drift time requirement is set at 3 ms, an electric field of 500 V/cm is needed and a -180 kV bias voltage has to be applied on the cathode plane.

Each APA is 2.3 m wide, 6.3 m high, and 12 cm thick and it is composed by four
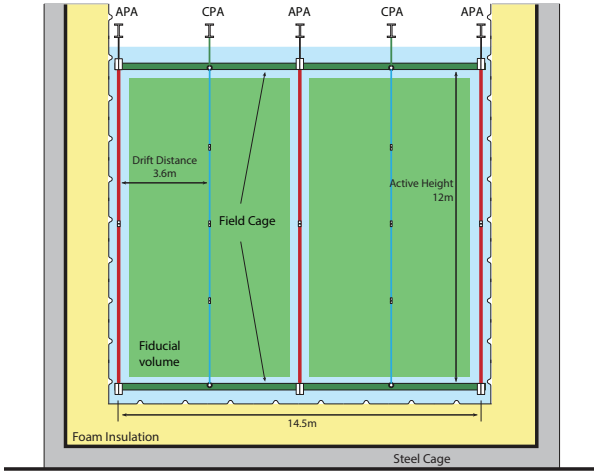
Figure 2.13: Front view of the DUNE TPC.

layers of wires: G, U, V and X starting from the outside. They are arranged as shown in Fig. 2.14 and are biased to a specific voltage in order to allow the ionization electrons to drift past the first three layers and be collected by the collection wires X. The G plane
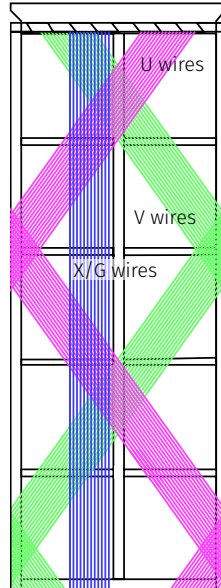
Figure 2.14: Illustration of the wire wrapping scheme. The colors represent different wire planes: red (U), green (V), blue (X). The G plane is parallel to the X one and above these three.

wires have the purpose of shielding the other planes from distant moving charges. A summary of the key parameters of the wire planes is in Table 2.3. A setup of two APAs,

Label	Function	Orientation	Bias Voltage [V]
G	Shield plane	0°	-665
U	1st induction plane	+35.7°	-370
V	2nd induction plane	-35.7°	0
X	Collection plane	0°	+820

Table 2.3: Parameters of the four planes of wires on an APA[29].

one above the other, repeated 25 times along the beam direction, constitutes one of the three APAs planes used in the TPC.

One of the requirements of the FD is a very high uptime of data collection (>99%) for beam and atmospheric neutrino and for proton decay candidates. The DAQ of each module of the far detector is thus completely independent from the other. This allows the detector to reduce by a big amount the dead time when none of the four modules is working.

Using this method is possible to obtain a similar multi-level trigger typical of collider experiments with only one level of trigger.

The Photon Detection System

As anticipated before, the scintillation light emitted by the liquid argon is exploited in the Far Detector for the determination of the time of emission of the events in the active volume. Liquid argon emits about 40000 photons every MeV of deposited energy with emission time, for about 1/4 of the emitted photons, of about 7 ns and wavelength of 128 nm. The Photon Detection System (PD) will measure emitted photons to provide timing information with a resolution better than 1 μs[25]. Due to the wavelength of the emitted photons being in the region of the Vacuum Ultraviolet (VUV), the detection efficiency of the available photosensors is low. Different designs are currently being tested in order to improve the performance of the PD. In the firs design, a single PD module is composed by a light guide and 12 SiPMs. Ten modules are mounted on each APA's frame as in Fig. 2.15 (b). The light guide re-emits the incident light emitted by the argon with a shifted wavelength whose intensity peak is around 430 nm. The re-emitted light is then transported through the light guide to the 12 SiPMs at the end of the bar thanks to a coating of TPB (Fig. 2.15 (a).

A second possibility, currently being tested in a single-phase DUNE Far Detector prototype (protoDUNE-SP)[30], is to use a new type of device able to detect the liquid argon scintillation light: the ARAPUCA (Argon R&D Advanced Program at UniCAmp)[31]. The basic idea behind an ARAPUCA is to use an high reflective material to trap the
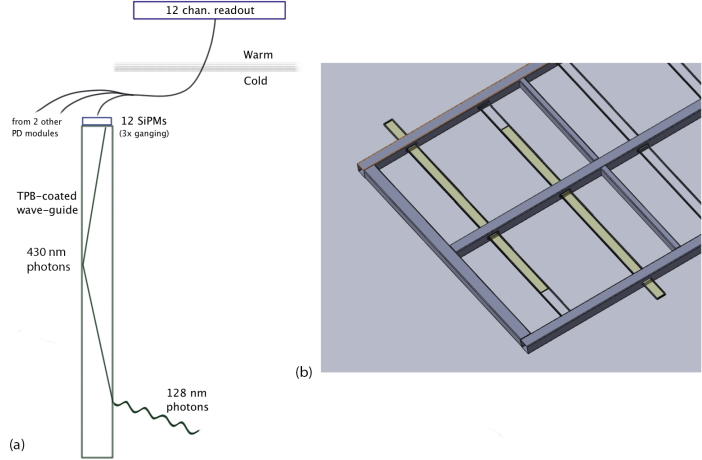
Figure 2.15: a) Schematic view of a single module of the Photon System. b) Example of mounted PD modules into an APA frame.

photons inside a box ($5 \times 5 \times 1$ cm^3). Doing so, the detection efficiency of the trapped photons remains high even with limited active area inside the box. Figure 2.16 shows a sketch of an ARAPUCA device. Photons trapping is achieved using a dichroic shortpass
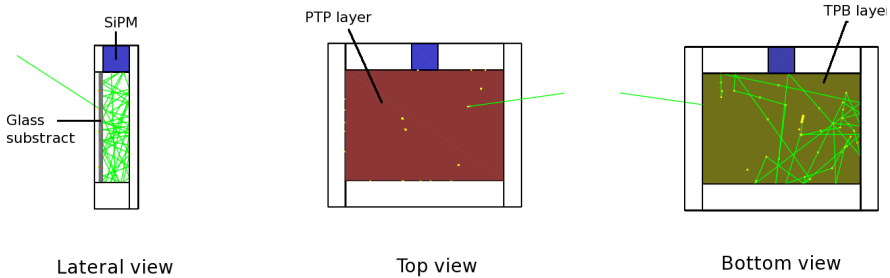

Figure 2.16: Lateral, top and bottom view of a simulated arapuca design[32].

optical filters. This is a film highly transparent to photons with wavelength below a cut-off value while it is almost perfectly reflective to photons above that value (Fig. 2.17). A filter of this type, coupled with two different wavelength shifters (one on each side) is used as acceptance window for the device, with the other internal faces covered with highly reflective material. On one internal surface is placed a Silicon Photomultiplier used to detect the trapped photons.

As for the first design, the ARAPUCA devices will be mounted on the APA frame as in Fig. 2.18.
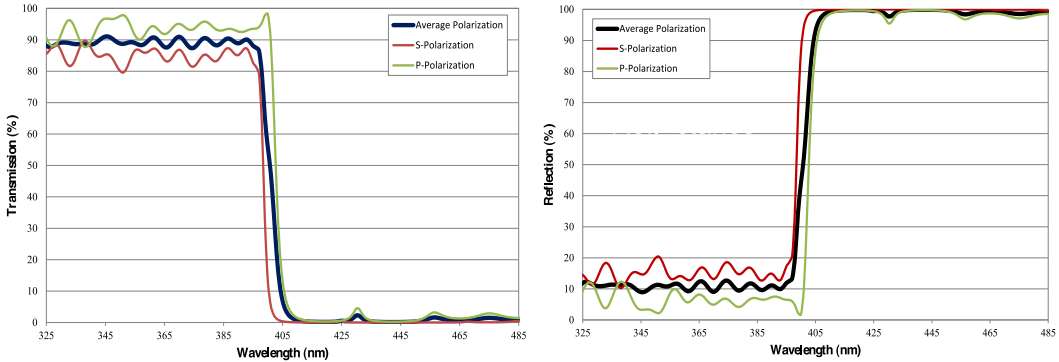
Figure 2.17: Reflectivity of the shortpass dichroic filter (left) and transmissivity of the same.
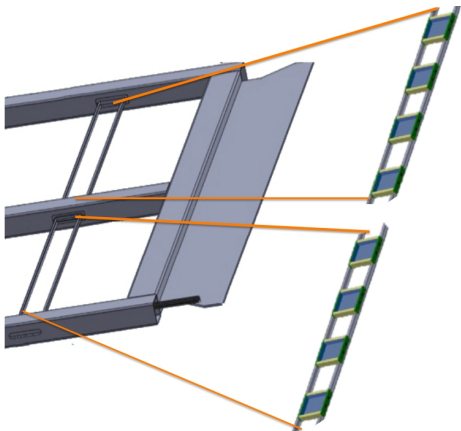
Figure 2.18: Representation of one array of 8 ARAPUCA devices installed in a APA frame.

Dual Phase LArTPC

Despite the first of the four modules of the Far Detector will use the design described above, an alternative design is considered for the other modules.

The design consists in a dual-phase LArTPC in which a volume of gas argon is used to extract, amplify and collect the ionization electrons. This technique, similar in many ways to the single-phase LArTPC, has different advantages over it, like a lower detection threshold, a larger fiducial volume and an higher gain.

With this design, the ionization electrons drift upwards vertically towards an extraction grid. This is used to extract the electrons from the liquid argon to the gas argon and is performed using an electric field of 2 kV/cm applied between the extraction and an amplification grid, with the first submersed in the liquid phase. After the extraction some devices, called Large Electron Multipliers (LEMs), produce the amplification of the

44

ionization electrons by avalanches, increasing the signal to noise ratio and improving the event reconstruction capability. The charge is collected using a segmented readout anode plane at the top of the gas volume. Differently from the single phase design, the dual
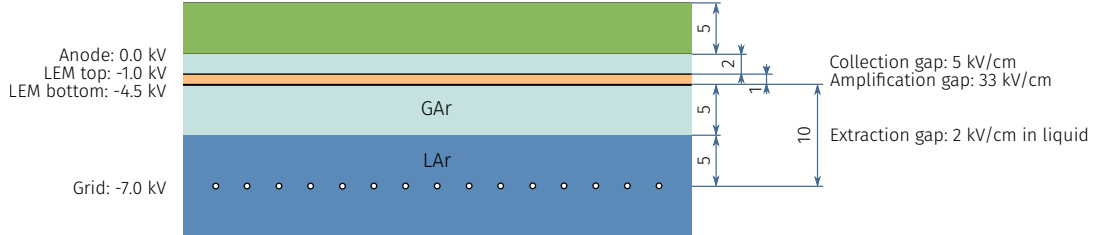
Figure 2.19: Schematic view of the thickness and voltage for the extraction and amplification of the electron.

phase LArTPC is not subdivided by cathode and anode planes. This makes the drift paths of the electrons much longer than the one in the single phase design and an higher electric field is thus needed to guarantee the correct functioning of the TPC. Moreover, due to the higher drift paths, the charge losses that occur in volume is higher compared to the one of the single phase design. However, the amplification of the signal improves the signal to noise ratio and compensates the charge losses and the same level of Argon purity is thus required for both the designs.

2.3.2 Near Detector

The Near Detector will be located underground at few hundred meters downstream of the neutrino source. It will be composed by two systems, one able to move from an on-axis position to an off-axis one and one with a fixed on-axis position. The final design of the mobile system is not yet finalized but it will be composed by a LArTPC, an high precision tracker inside of a magnet and Electric Calorimeter (ECAL). For the fixed system, some of the components previously used in the KLOE experiment will be used. These include the magnet and the electromagnetic calorimeter to which a second high precision internal tracker will be added. Table 2.4 summarizes the performance requirements of the Near Detector. As anticipated in Section 2.1.3, one of the main objectives of the ND is to perform all the measurements needed to constrain the systematic uncertainties for the signal and background events in the Far Detector. To do so, the neutrino interaction need to be studied with the same target used in the Far Detector. In addition to the LArTPC of the mobile Near Detector system thus, the possibility to add a second volume of Argon in the fixed system is currently being studied.

Parameter	Requirement
Dipole Magnetic Field	0.4 T
Average target/tracker density	$\rho \sim 0.1 \mathrm{g/cm}^3$
Target/tracker Mass	8 t
Vertex Resolution	0.1 mm
Angular Resolution	2 mrad
E_μ Resolution	5%
$\nu_\mu/\bar{\nu}_\mu$, $\nu_e/\bar{\nu}e$ ID	Yes

Table 2.4: A summary of the required performance for the FGT[28].

Movable Detector

The main components of the movable system of the ND will be a LArTPC, the central tracker, an electromagnetic calorimeter and a muon identifier. With the exception of the LArTPC, these components will be enclosed in a dipole magnet and together will compose the so called Fine-Grained Tracker (FGT). As of today, a final design of the FGT is not yet defined but, independently from its design, it should be able to perform all the measurements needed at the Near Detector. The most significant ones being the measurement of particles' momentum and charge, the e^+/e^- separation for absolute and relative flux measurements, the identification of π^0 and γ and studies to quantify the impact of nuclear effects in $\nu(\bar{\nu})$-nucleus cross sections. Figure 2.20 shows a sketch of one of the proposed designs.

Externally to the dipole magnet, a LArTPC will be installed upstream of the FGT. The design of this TPC cannot be identical to the one of the Far Detector's TPC due to the event-pileup that could arise because of the high intensity of the neutrino beam. The current design is shown in Fig. 2.21 and it consists of an array of 5×7 modules[33]. Each module consists of two TPCs. This type of design reduces the drift distances to about 50 cm, also reducing the electrons drift time and the events pileup. Combining the LArTPC and the FGT it should be possible to enhance the detector capability and to provide a means to accurately validate the FGT predictions before the extrapolation to the FD.

KLOE

At a fixed on-bean position, a compact multipurpose detector will be placed. As for the movable system, it should be capable of precision tracking, charge discrimination and calorimetry as well as be able to detect events of different target materials. The detector
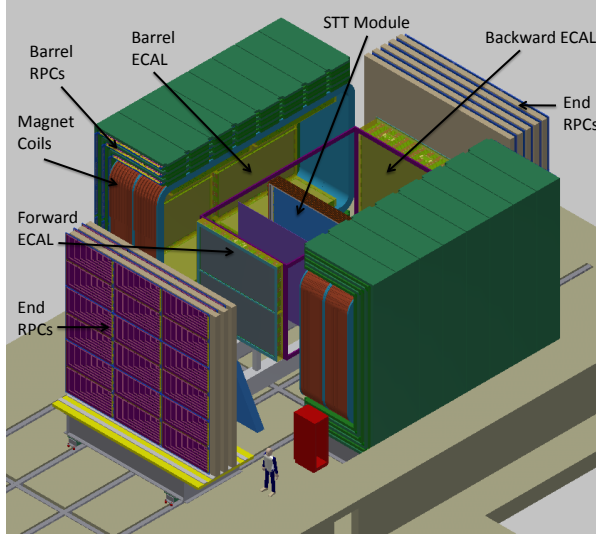
Figure 2.20: A schematic drawing of the fine-grained tracker design.
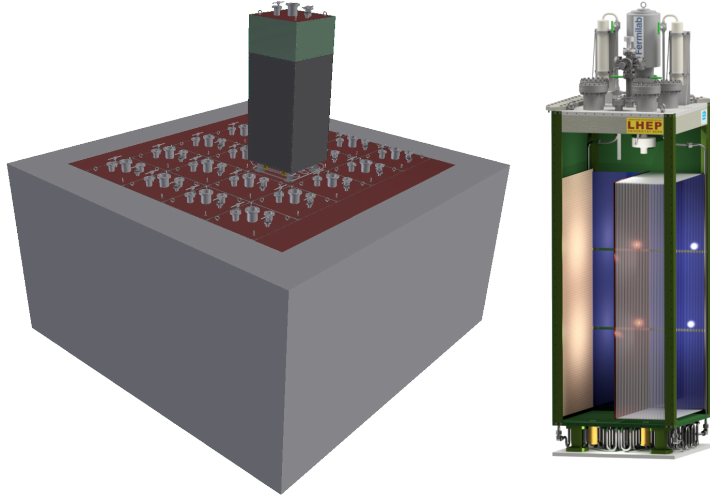
Figure 2.21: Sketch of the current design of the ND LArTPC (left) and of a single module of the same (right)[34].

will re-use the magnet and electromagnetic calorimeter of the KLOE experiment[35] which will be complemented with an high precision internal tracker. Figure 2.22 shows a section of the KLOE detector.

Calorimeter The KLOE calorimeter is a sampling calorimeter composed by lead and scintillating fiber. It is subdivided in an almost cylindrical barrel calorimeter and two additional calorimeters used as end-cap, all enclosed inside the magnet. The barrel
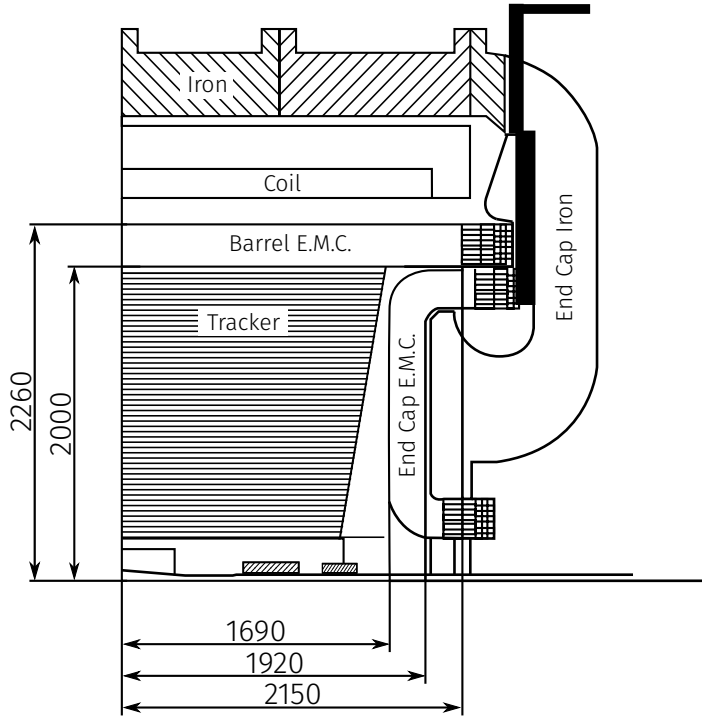
Figure 2.22: Vertical cross section of the KLOE detector. Units are in mm.

calorimeter consists of 24 trapezoidal modules 4.3 m long while the end-cap consists of 32 vertical modules of different length, as shown in Fig. 2.23. Each module is a stack of about 200 lead foils 0.5 mm thick alternated with 200 layers of 1 mm diameter scintillating fibers. The energy and time resolution were obtained during the running phase of KLOE and and their values are[35]:

$$\text{Energy resolution: } \frac{\sigma}{E} = \frac{5\%}{\sqrt{E(\text{GeV})}} \tag{2.6}$$

$$\text{Time resolution: } \frac{54}{\sqrt{E(\text{GeV})}} \text{ ps} \tag{2.7}$$

Inner Trackers As for the tracker of the movable system, the KLOE inner tracker should offer a target for the neutrinos interactions and provide the capability to reconstruct the momenta of all charged particles.

The chosen design of this component is based on the straw tube technology and its main component is the Straw Tube Tracker (STT). The STT is composed by straw tubes with an outer diameter of 5 mm. Each module of the STT is composed by a double

48
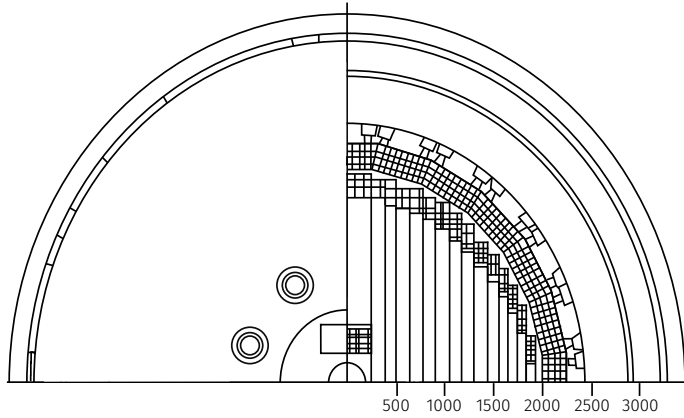
Figure 2.23: Front view of the KLOE calorimeter showing the trapezoidal and vertical modules. Units are in mm.

layer of tubes staggered by a half-diameter. Two modules are assembled together, one vertically (YY) and one horizontally (XX), to form a double-module (XXYY). The tubes are filled with a mixture of 70% Xe and 30% CO_2 at about 1.9 atmosphere of pressure.
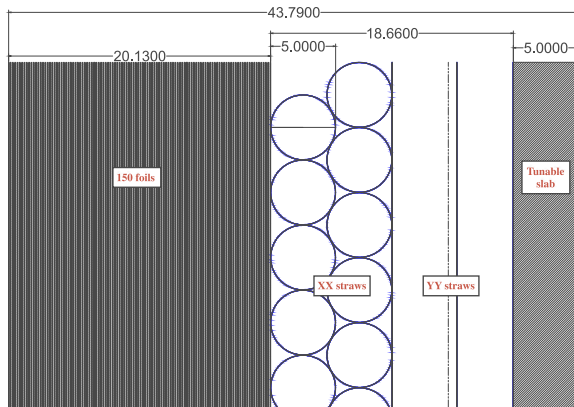
Figure 2.24: A schematic drawing of the Straw-Tube Tracking Detector (STT) design.

Before each double-module a radiator of 150 polypropylene Ch_2 foils is used for the e/π differentiation through the Transition Radiation. A polypropylene CH_2 target slab follows the four straw layer to achieve the desired target mass and detector density (Fig. 2.24).

Both the radiator and the polypropylene slab can be removed and replaced with different nuclear targets. These targets are made by plates with tunable thickness in order to provide the same fraction of X_0 as the configuration with the radiator. Two of the most important materials that could be used as target are graphite and calcium.

49

The first one is used to perform background measurements while a Ca target, having the same atomic weight as Argon, allows a complete characterization of the A = 40 nucleus.

Argon Target   As mentioned before, it is of fundamental importance to understand the nuclear effects of different nuclear targets. In particular, it is important to study these effects in Argon as it is the material used in the Far Detector.

The design of KLOE and its inner tracker allows to fill part of the KLOE inner volume with a liquid Argon target in direct contact with the calorimeter, at the entrance of the tracking volume. With such configuration, neutrino interactions could be studied on different materials (Argon, Hydrogen and Carbon) within the same detector.

Due to the event pileup and the presence of a magnetic field in the inner volume of KLOE, this volume cannot be used as a LArTPC. To detect and reconstruct neutrino interactions within this region, a different detection method is thus needed. This system should provide the same tracking precision of the inner tracker and be fast enough to avoid the event pileup. Moreover, it should works in a magnetic field.

The study of a detection system able to fulfill all the above requirements is the main objective of this thesis and will be carried on in the next chapters.

Chapter 3

An Innovative Detector

3.1 Concept

As seen in Section 2.3.1, the LArTPC technology uses both the scintillation light emitted by the argon and the electrons produced by ionization.

At the Far Detector, the Vacuum Ultra Violet (VUV) scintillation light is shifted by means of a wavelength shifter and collected to provide information on the deposited energy and the timing of the event, while the drift of the ionization charges is used for the topological reconstruction of the event.

Because of the relatively slow drift of the electrons, a setup similar to the one of the Far Detector will have a time response of the order some milliseconds and could be not suitable for an high rate of particles due to the pileup of the events. To solve this problem, an alternative and innovative approach, able to provide a much faster response could be to use the scintillation light not only for calorimetric measurements, but also to provide the spatial reconstruction of the event.

This could be possible thanks to the scintillation properties of the Argon. Liquid Argon emits about 40000 photons per MeV of deposited energy for electrons or m.i.p. particles[36], with the intensity peak around 128 nm,as shown in Fig. 3.1, and with a decay time of the fast component of 7 ns. In addition to this, the Rayleigh scattering length is about 95 cm at 128 nm[37] and the attenuation length of the light is of the order of one meter[38], making liquid Argon quite transparent to its own light and making possible to exploit the scintillation light for imaging purposes.

Exploiting the liquid argon properties then, one could theoretically cut the response time to some nanoseconds instead of some milliseconds while still obtaining high spatial resolution. To do so, an optical system able to collect the light, as well as a fast, segmented photon detector with which collecting the light, is needed.

Usually, optical system are made using lenses and mirrors. The liquid argon scintillation light, however, is emitted with a wavelength in the Vacuum-Ultra-Violet region,
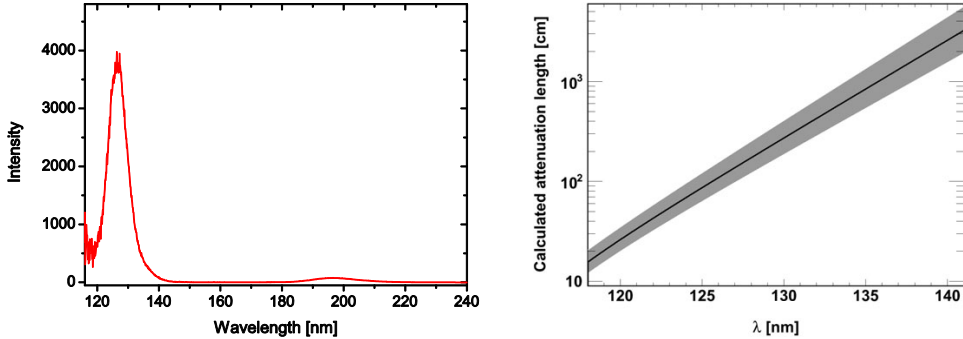
Figure 3.1: Spectrum of the emitted scintillation light of liquid argon (left) and attenuation length as a function of wavelength (right).

for which lenses' and mirrors' transmission is highly inefficient. Another complication resides in the fact that the distance of the event's tracks, depending on the application, can be up to several meters, making necessary a large field of view and depth of field to allow the focusing of the higher number of tracks possible. Finally, because of the use of liquid argon, the system must be maintained at cryogenic temperature, making even more difficult to achieve the above conditions.

A different approach is thus needed. A possible alternative could be the use of a technique already known in the X-ray and gamma-ray astronomy but never studied for particle physics applications, the Coded Aperture Mask. This technique, described more in detail in the next section, should act as an high luminosity lens with the advantage of an infinite Depth of Field (DOF) and a large Field of View (FOV). However, as it will be discussed later, both the use of the tradition lenses and the coded aperture have some limitations that don't make one indisputably better than the other one.

Using an optic-sensor system one could take a 2D picture of the tracks of the events and, using multiple systems arranged in a stereo view, one could be able to perform a complete 3D reconstruction of the event.

The aim of this thesis is to study the feasibility of a detector based on this concept both for the Coded Aperture technique and also for the lenses.

3.2 Coded Apertures Technique

The first coded aperture concept was first introduced in the late '70[39] and, since then, it was used mainly in astronomy and space applications. This technique was first developed to overcome some problems of the simpler pinhole camera. The most important advantage of coded aperture is an improvement of the Signal To Noise (SNR) ratio, that allows an higher resolution and less exposure time. To introduce the idea of this technique, one can thus start from the description of the pinhole camera.

3.2.1 Pinhole and Coded Aperture Cameras

A pinhole, the simplest imaging device, is basically a slab of opaque material with a very small hole, ideally dimensionless, and a photon detector behind it. With a setup of this type, every photon emitted by an object have to pass through the hole along a straight line (Fig. 3.2). As a consequence, the signal recorded by the detector is an inverted picture of the object with a one-to-one correspondence between the twos. In the pinhole
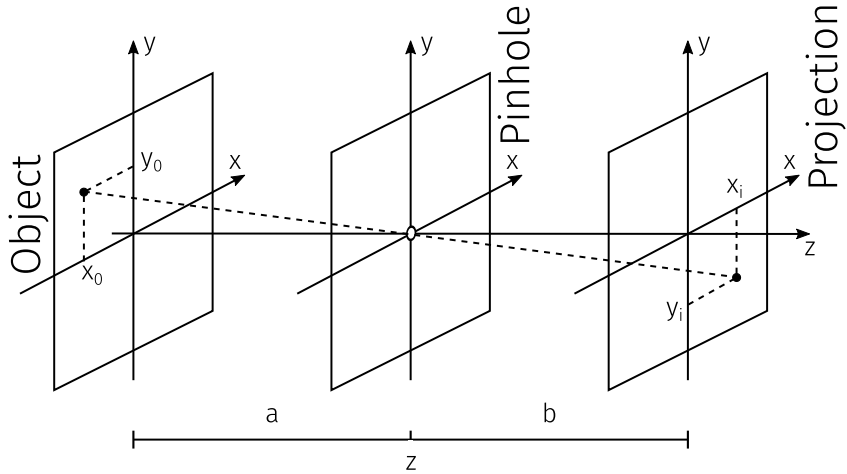

Figure 3.2: Scheme of a pinhole camera.

camera therefore, the detector response on a certain position $R(x_i, y_i)$ is caused only by a source point (x_0, y_0) and must be proportional to its irradiance:

$$R(x_i, y_i) \propto O(x_0, y_0). \tag{3.1}$$

Another contribution on the detector response comes directly from the size of the hole, with bigger holes letting more light pass through and increasing the SNR.

An ideal pinhole camera, i.e. a dimensionless pinhole coupled with an ideal detector, should provide a perfect reconstruction of the image as two point sources will always be separated on the detector. Real pinholes however, are not dimensionless and a point source will be detected as an extended circular source, as in Fig. 3.3, decreasing the resolution. The size of the pinhole then cannot be increased indefinitely to increase the detector response due to the decreasing in the resolution. This is one of the main problems that lead to the formulation of the Coded Aperture Technique: the need of resolution like the one obtained with small pinholes while maintaining an high light signal.

The fundamental idea of coded aperture is to open a large number of pinholes instead of one. These pinholes, placed with a specific order, are called a *mask*. Each hole of the mask will then generate an image of the object on the detector.
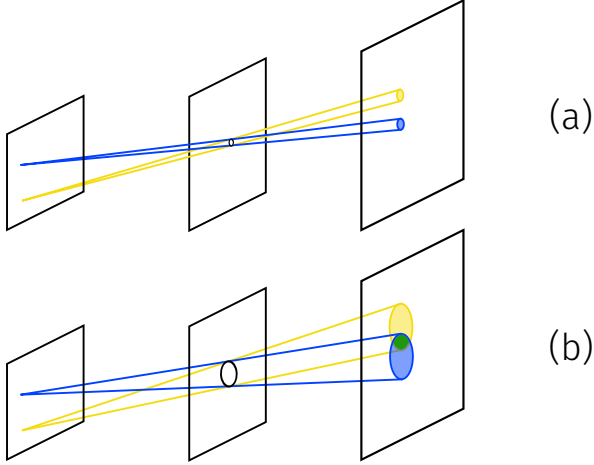
Figure 3.3: Degradation of the resolution of a pinhole camera due to the finite size of the hole. In case of infinitesimal hole (a), two point sources are projected as two, flipped, points on the detector. Finite size of the hole (b) cause the points to be projected as circles.

The detector response at the position $\vec{r_i}$ using this technique will then be proportional to the irradiance $O(\vec{r_0})$ modulated by the transmission of the mask at the point of intersection with the ray going from $\vec{r_0}$ to $\vec{r_i}$[40]:

$$R(\vec{r_i}) \propto O(\vec{r_0})A(\vec{r_0} + \frac{\vec{r_i} - \vec{r_0}}{z}a). \tag{3.2}$$

To obtain the total detector response one can simply integrate over the object plane:

$$R(\vec{r_i}) \propto \int_{\vec{r_0}} \int O'(\vec{r_0^i})A'(\vec{r_i} - \vec{r_0^i})d^2\vec{r_0} = O' * A' \tag{3.3}$$

where

$$O'(\vec{r}) \equiv O(-\frac{a}{b}\vec{r}) \qquad A'(\vec{r}) \equiv A(\frac{a}{b}\vec{r}) \qquad \vec{r_0^i} = -\frac{b}{a}\vec{r_0} \tag{3.4}$$

with a the object-mask distance and b the mask-sensor distance. The detector response is thus:

$$R \propto O' * A'. \tag{3.5}$$

Comparing Eq. (3.5) with Eq. (3.1), one can clearly see that in the case of the coded aperture the response does not resemble the object directly as for the pinhole but depend upon both the emissivity of the source and the mask transmittance. The mask is thus encoding the signal from the source due the superposition of the many shifted copies of the image produced by the holes and projected on the detector. A decoding process is thus needed to obtain the starting image. Figure 3.4 shows a simplified scheme of how the technique works.

The reconstructed image can be obtained using the correlation method, in which the reconstructed object is defined as[39]:

$$\hat{O} = R \otimes G = (O' \times A') \otimes G = O' * (A' \otimes G) \tag{3.6}$$

where G is a decoding array called kernel and $\otimes$ and $*$ indicate the correlation and the convolution respectively. Equation (3.6) shows that the choice of A and G is crucial. If
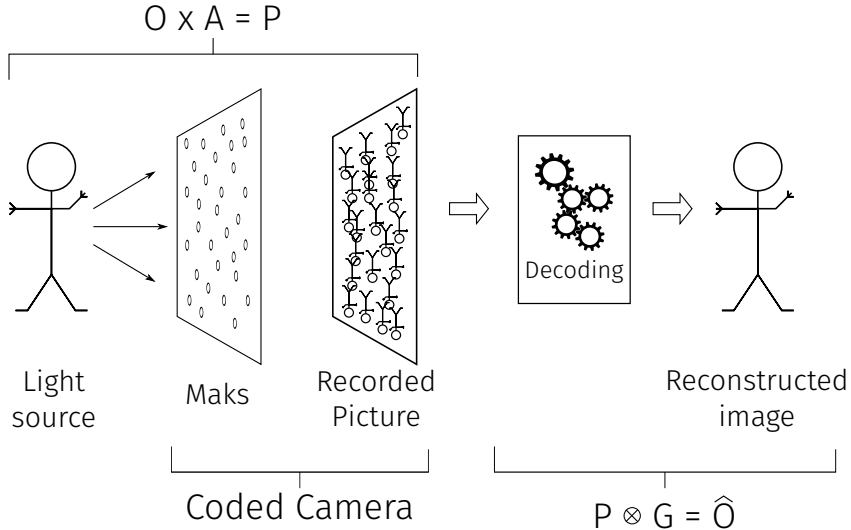

Figure 3.4: Scheme of the encoding and decoding of the signal of a coded aperture camera.

for the couple it is valid:

$$A' \otimes G = \delta \tag{3.7}$$

Eq. (3.6) becomes:

$$\hat{O} = O' * \delta = O'. \tag{3.8}$$

and the system has perfect imaging properties, as it can reconstruct the exact initial image. Since A and G can be chosen a priori, it is possible to generate pairs able to satisfy the condition (3.8). Many different families of (A, G) are known in literature. The most common choice is to get A as a 2-D array of 0 or 1, that represent the opaque or transparent region of the mask and G varying from family to family.

The decoding technique here described is valid as long as the source is distant from the mask in the so called Far Field approximation. As it will discussed later, for sources at short distance from the mask, Eq. (3.5) is no longer valid and the decoding process will generate artifacts, making the use of this technique more challenging.

3.2.2 MURA: Modified Uniformly Redundant Arrays

The masks used in this thesis are part of the MURA, Modified Uniformly Redundant Arrays, family. These are a modification of the URA mask[39], whose name shows that the holes of the mask are separated from each other with a distance that occurs a constant number of times.

The mask A described above, in the case of an URA mask, is generated as follow:

$$A_{i,j} = 0 \text{ if } i = 0 \tag{3.9}$$
$$1 \text{ if } j = 0, i \neq 0$$
$$1 \text{ if } C_i^r C_j^s = +1$$
$$0 \text{ otherwise}$$

with

$$C_i^r = +1 \text{ if } i \text{ is a quadratic residue modulo r} \tag{3.10}$$
$$-1 \text{ otherwise}$$

and r and s prime numbers and $|r - s| = 2$. For the URA masks, the kernel G is equal to the mask, G = A. The MURA masks are an extension of the URA in which the distance that separates the holes can occur multiple times and in which different values of the difference $|r - s|$ modify the properties of the mask. The array for which $r - s = 0$ has important properties and is the one used in this thesis. The generation of the mask is performed according to Eq. (3.9) but the different value of $|r - s|$ implies the need to modify the kernel, as the autocorrelation function - the result obtained from the reconstruction of a point source - is not a delta function. The kernel is then generated as follow[41]:

$$G_{ij} = 1 \text{ if } i + j = 0 \tag{3.11}$$
$$1 \text{ if } A_{i,j} = 1, \ i + j \neq 0$$
$$-1 \text{ if } A_{i,j} = 0, \ i + j \neq 0.$$

An important property of these arrays is that the open fraction, i.e. the number of open elements respect to the total number of elements of the array, is always:

$$N_{open} = \frac{N_{total} - 1}{2} \tag{3.12}$$

hence the open fraction is always about 50%. Figure 3.5 shows some examples of MURA masks, generated by Eq. (3.9), used in the simulation of the detector while Fig. 3.6 shows the autocorrelation function, exhibiting how the procedure of generation described in (3.11) produces a kernel that respect the condition $A \times G = \delta$.

Figure 3.5: Examples of MURA masks of different ranks.
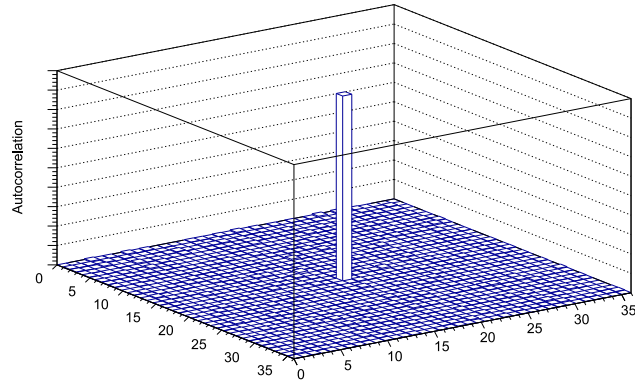
Figure 3.6: Autocorrelation function of a 37×37 MURA mask.

3.2.3 Signal to Noise Ratio

As anticipated before, the main reason behind the development of the coded aperture technique is the higher SNR that can be achieved compared to the one obtained with a pinhole camera.

A pinhole camera counting a number s of events will have, statistically, a noise equal to $\sqrt{s}$. The SNR of a pinhole camera is then equal to $\sqrt{s}$[40].

Increasing the number of holes one can also increase the signal. Using a mask with N holes, the final number of events will be $N*s$ while the noise $\sqrt{Ns}$. The SNR increase using a coded aperture camera instead of a pinhole one is then $\sqrt{N}$.

It is possible to demonstrate that this assumption is valid only for point sources or for masks whose autocorrelation function is a delta function. As showed before, this is the case of the MURA mask family. Using a 20×20 MURA mask one obtains an increase of the SNR of about $\sqrt{N} = 14$, making clear the advantage of the coded aperture camera

57

with respect to the simpler pinhole camera.

3.2.4 Geometry Arrangements, Field of View and Resolution

Different arrangements between mask and detector are possible. To better understand the advantages of one over the other it is necessary to distinguish two regions of the FOV of the detector: one in which the sources project a complete shadow of the mask on the detector, called Fully-Coded Field of View (FCFV), and one in which the projection is not complete, called Partially-Coded Field of View (PCFV), as shown in Fig. 3.7.

Since a perfect imaging can be obtained only if all the mask's shadow is projected on the detector, the arrangements with the larger FCFV are the more suitable for a detector based on this technique. The most simple arrangement is with mask and detector having the same size (Fig. 3.8a). An arrangement of this type has a limitation on the fact that only sources on the instrument axis and at great distance from the mask project a full mask's shadow, limiting the FCFV, while all the sources off-axis project a partial shadow and lie in the region of PCFV. The sources in the PCFV cannot be reconstructed perfectly and should be avoided when possible. To increase the number of sources included in the
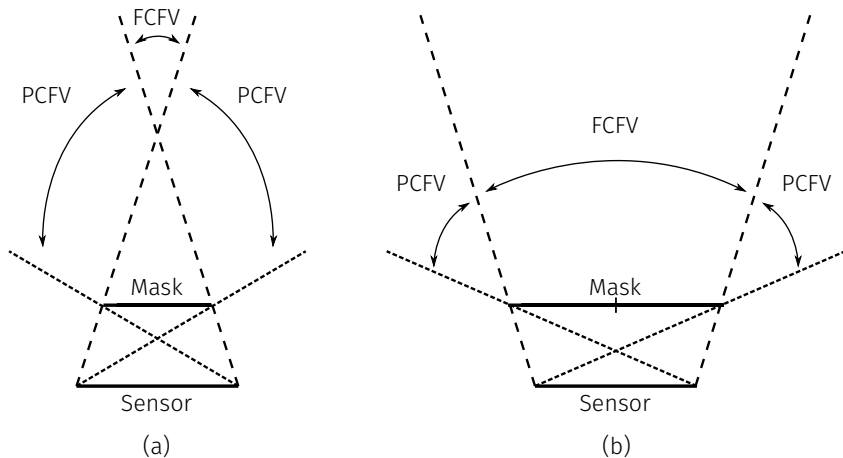
Figure 3.7: Scheme of the FCFV and PCFV for a camera with a single mask (left) and for one with a mask composed by a 2×2 mosaic (right).

FCFV, the easiest solution is to increase the size of the detector as in Fig. 3.8b. This will increase the FCFV but comes at the price of more expensive detectors. The most common alternative is then to enlarge the mask, using a mosaic composed by 4 masks arranged in a 2×2 grid and keeping the detector of the same size of the first arrangement. Using this arrangement, the shadow of the mask could be shifted depending on the source position (Fig. 3.8c) but the condition in Eq. (3.7) is still valid. Despite increasing the FCFV, none of this arrangements solves the problem of sources in the PCFV; the only possible solution could be to shield these sources, but it's not viable for this application.
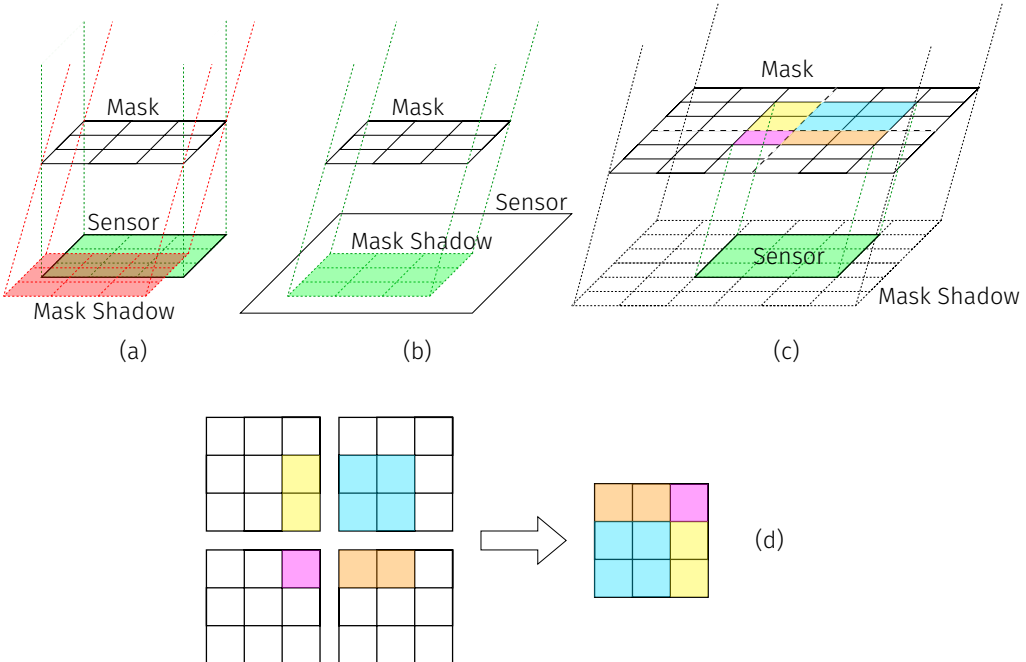
Figure 3.8: Comparison of three different coded camera arrangements. a) Mask and detector have the same size and only the sources on the optical axis project the full mask shadow on the sensor. b) The sensor is larger than the mask, allowing more sources to project the full mask shadow on the sensor. c) The mask is composed by a 2×2 mosaic of the mask in a) and b) while the sensor has the same dimension of the one used in a). In this configuration only a part of the mask is projected on the sensor. d) The combination of the projected parts on the sensor of the mask in c) is the full shadow of one of the mask composing the mosaic.

The field of view of the coded aperture camera is influenced not only by the chosen arrangement but also by the geometric resolution of the system, i.e. the reachable resolution of the system due to the geometric design. Defining the magnification of the mask as the ratio of the projection of the mask to the mask itself:

$$m = 1 + \frac{b}{a} \tag{3.13}$$

one can write[40]:

$$FoV = \frac{d_d}{m - 1} \tag{3.14}$$

with d_d the lateral dimension of the detector. At the same time, the FoV is in relation with the resolution λ of the camera as follows:

$$\frac{FoV}{\lambda} = \frac{d_m}{p_m} \tag{3.15}$$

where d_m, p_m are the lateral dimension and the holes' dimension of the mask respectively and λ is defined as:

$$\lambda = \frac{m}{m-1}p_m.$$ (3.16)

Combining these equations one obtains the final equation for the resolution of a coded camera:

$$\lambda = p_m\left(1 + \frac{FOV}{d_d}\right).$$ (3.17)

Field of view, resolution and magnification of the system are thus coupled together in a way that makes difficult to find a stable configuration due to the different distances between the mask and the event tracks that can occur in the detector. As it will be shown later, some constrains will be used on some of this quantities, limiting the potentiality of a detector of this type.

3.3   Coded Camera and Lens Comparison

As stated before, there are some limitations for both lenses and masks that can influence their feasibility in some situations. While more rigorous results will be discussed later in this thesis, some qualitative analyses of the advantages and disadvantages of both methods are described here. In the following, the results of these analyses are obtained using the same simulation described in Section 4. The only difference is in the generation of the photons, here generated ad hoc for the analyses instead of through the simulation of real particles.

3.3.1   Artifacts

While the condition (3.7) is crucial to obtain perfect imagining properties using masks, it is also the main reason why coded aperture is affected by non-idealities. When the projection of the mask doesn't resemble exactly the mask itself, different types of artifacts arise.

Sampling artifacts

The first type, the Sampling artifact, arises when the number of pixels on which the shadow of a single element of the mask is projected is not an integer. Defining this number as:

$$\alpha = \frac{mp_m}{p_d} = \frac{(1 + \frac{b}{a})p_m}{p_d}$$ (3.18)

with m defined as (3.13), only specific configurations allow α to be an integer. While for integer value of α the kernel can be rescaled to match the size of the shadow, non-integer

values make the scaling impossible and the condition (3.7) not valid. To evaluate the importance of this type of artifacts a simulation of a point source has been performed several times, changing the value of α using different dimensions of the mask's hole. Figure 3.9 shows the reconstruction of the point source obtained with these simulations. As can been seen, a 10% variation of α is enough to make the reconstruction almost dominated by the artifacts while, for variation up to about 5%, the reconstruction is still good.
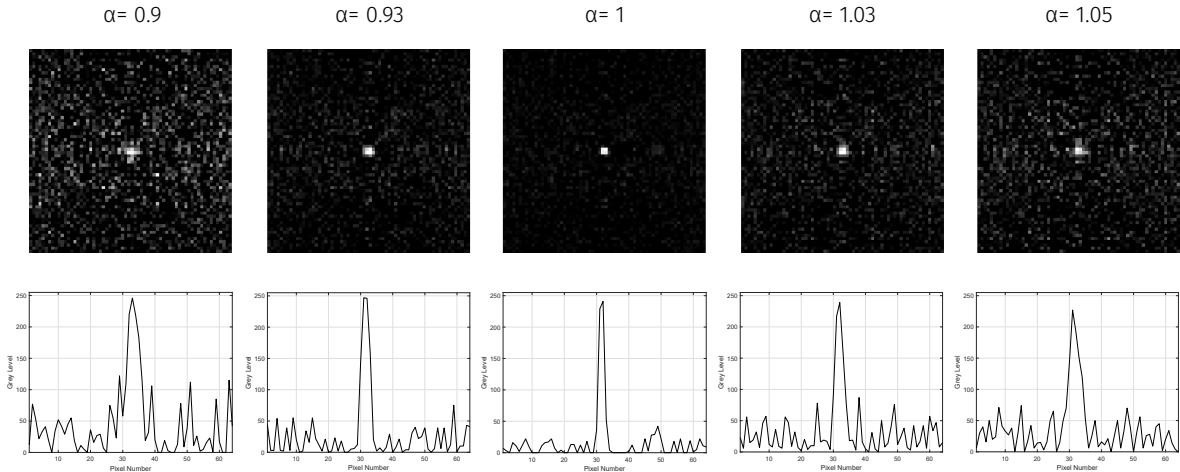
Figure 3.9: Results of the simulation of a point source for different values of α (top) and gray-levels of the row passing through the center of the images (bottom).

Because of the nature of this artifact, its completely remotion is challenging. In applications in which the distance of the source is known, one could change the other parameters of Eq. (3.18) to make α an integer. In a particle detector that uses this technique, however, the distance cannot be known a priori, making this artifact almost impossible to remove.

At small distances however, another type of artifacts arises. These artifacts, known as Near-field artifacts, dominate over the sampling artifact and their removal is of fundamental importance.

Near-field Artifacts

These artifacts are a consequence of the dependence of detector counts on the position on the detector itself. The detector's response at the position $\vec{r_i}$ can be expressed as[42]:

$$R(\vec{r_i}) \propto \int_{\vec{r_0}} O(\vec{r_0}) A(\frac{a}{z}\vec{r_i} + \frac{b}{z}\vec{r_0}) \cos^3(\theta) d^2\vec{r_0} \tag{3.19}$$

with $\theta = \text{atan}(|\vec{r_i} - \vec{r_0}/z)$ and $z = a + b$.

When the object is at large distance from the mask, the condition $|\vec{r_i} - \vec{r_0}| << z$ $\forall (r_i, r_0)$ is valid and

$$cos^3(\theta) \simeq 1. \tag{3.20}$$

This is the far-field approximation used in Section 3.2.1. It is possible to demonstrate that, under this approximation, Eq. (3.19) is reduced to the convolution in (3.5), while for distance for which $|\vec{r_i} - \vec{r_0}| \simeq z$, Eq. (3.20) doesn't hold and the near-field artifact arises.

Figure 3.10 shows the effect of the modulation due to the distance of the source from the mask.

| a = 20 cm | a = 10 cm | a = 5 cm | a = 2 cm |
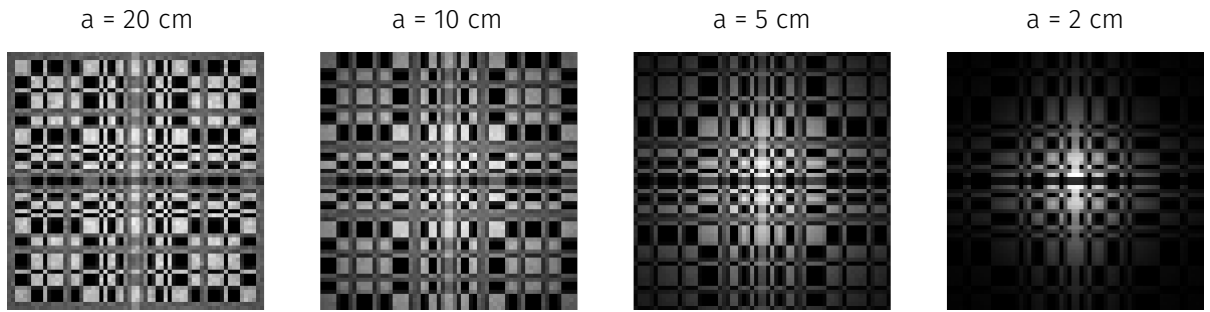
Figure 3.10: Modulation of the detector counts due to the source-detector distance.

To study the problem of near-field artifacts, one can expand the near field term in Eq. (3.19) in Taylor series and examine the contribution of each decomposed part. The majority of near-field artifacts can be avoided studying correction up to the second order of the Taylor expansion.

Zero order correction   Rewriting Eq. (3.19) as:

$$R(\vec{r_i}) \propto \int \int_{\vec{\xi}} O'(\vec{\xi}) A'(\vec{r_i} - \vec{\xi}) \cos^3 \left[\text{atan} \left(\frac{|\vec{r_i} + \frac{a}{b}\vec{\xi}|}{z} \right) \right] d^2\vec{\xi} \tag{3.21}$$

and expanding it at the zero order, one obtains:

$$R(\vec{r_i}) = \cos^3(\text{atan}(\frac{|\vec{r_i}|}{z})) \int \int_{\vec{\xi}} O'(\vec{\xi}) A'(\vec{r_i} - \vec{\xi}) d^2\vec{\xi}. \tag{3.22}$$

Here the condition in Eq. (3.5) is not valid anymore and the convolution with the kernel is not able to produce the initial image. As can be seen however, the zero order artifact is generated due to a prefactor in the detector response determination. One could then divide the detector's counts to obtain again the condition in (3.5) as for the far field approximation. Figure 3.11 shows the reconstruction of two different simulated sources, one squared and one linear, and their reconstruction with the first order correction applied.

62

| Simulated | No correction | Zero-order correction |
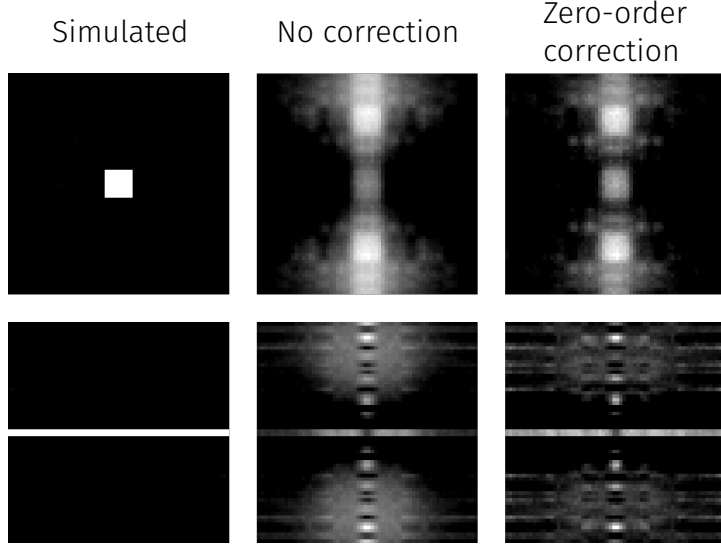
Figure 3.11: Results of the simulation of a squared and linear source with and without zero-order correction.

As can be seen, despite being still dominated by other artifacts, a small improvement appears and the sources can be better distinguished. To get rid of the remaining artifacts one has to extend Eq. (3.21) to a higher order.

First order correction Expanding equation (3.19) to the first order, and excluding the zero order term, one obtains:

$$R(\vec{r_i}) \propto \frac{\vec{r_i}}{z^2 + |\vec{r_i}|^2} \int\int_{\vec{\xi}} \vec{\xi} O'(\vec{\xi}) A'(\vec{r_i} - \vec{\xi}) d^2\vec{\xi}. \tag{3.23}$$

It is possible to demonstrate that, if A' covers the FOV uniformly and the source is also uniform, the integral is almost constant and one can write the reconstructed image in equation (3.6) as:

$$\hat{O} \propto O' \int\int \frac{\vec{r_i}}{z^2 + |\vec{r_i}|^2} G'(\vec{r_i} + \vec{\eta}) d^2\vec{r_i} \tag{3.24}$$

where O' is the constant result of (3.23). Equation (3.24) is an important result as it shows that the reconstructed image, and thus the first order artifact, depends on G only. Figure 3.12 shows the results of the integral in Eq. (3.24) for a MURA mask. As can be seen there is a sharp discontinuity at the center that could generate the first order artifact as a modulation of the reconstructed image's intensity. To avoid these artifacts two solutions are possible: the easiest solution is to change the algorithm with which one generates the mask (and thus also the kernel) so that the discontinuity is shifted to the side of the reconstruction. In the cyclic arrangement used in this thesis and discussed
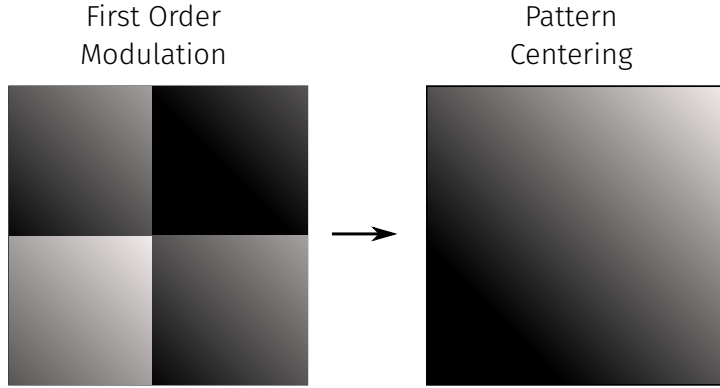
Figure 3.12: Expected form of first-order artifacts for a MURA mask (left) and result of the pattern centering correction (right).

in Section 3.2.4, this is done by rotating the copies of the mask to merge each first row and column in the center of the mosaic, as in Fig. 3.13. This process is called centering of the pattern.
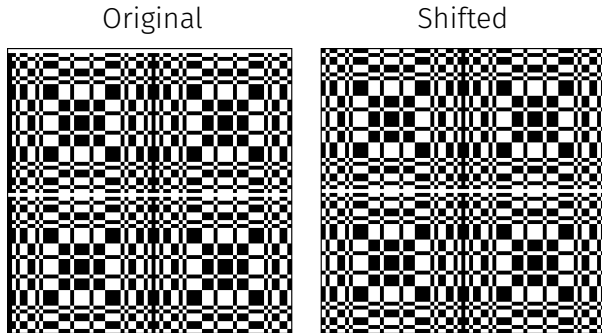
Figure 3.13: Pattern centering for a 2×2 MURA mosaic.

A second approach is to center the object in the FOV of the camera. From Eq. (3.23) indeed, one can see that if the object is centered with respect to the FOV, $\vec{O'}$ would be zero, and the artifacts will disappear. As for the Sampling artifact, this solution is not easy to apply due to the fact that the particles track will be at random positions in the detector volume.

Figures 3.14 and 3.15 show the reconstruction results obtained with a squared and a linear source at two different positions, both with and without first-order corrections. As can be seen, without first order corrections, the reconstructed images present a modulation that recall the one generated by the kernel in Fig. 3.12, and that it is more evident when the source is off-center. It is also clear how better results are obtained, as expected, with a source in the center of the image, while the off-center sources are still dominated by the artifacts. For the centered sources, however, a new type of artifacts
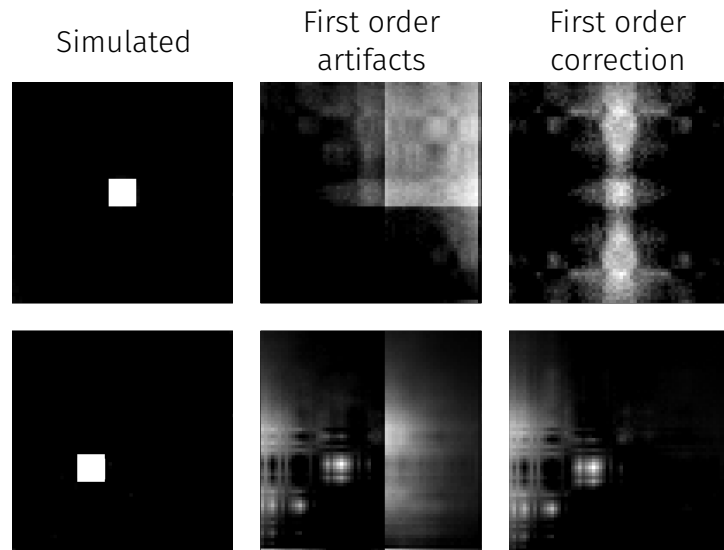
Figure 3.14: Results of the simulation of a squared source with and without first-order correction.

becomes visible: the second-order near field artifact. These artifacts are the symmetrical halos on the top and bottom of the image and become visible when the first two order are suppressed.
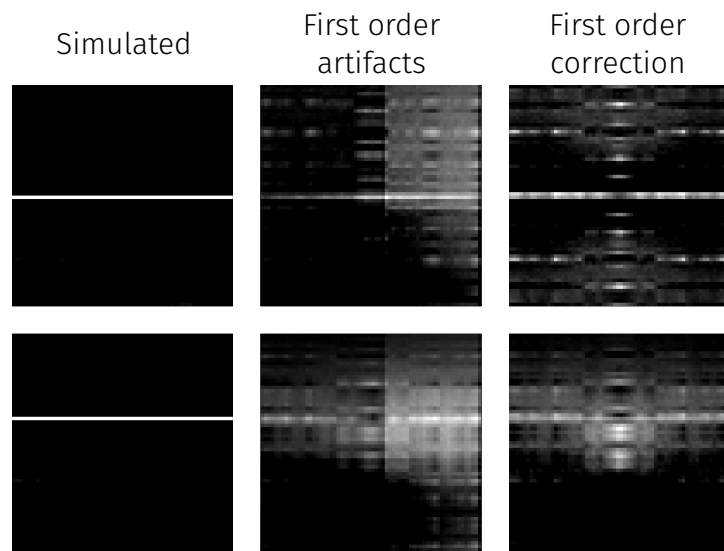
Figure 3.15: Results of the simulation of a linear source with and without first-order correction.

Second order correction   When first order artifacts disappear, the second order artifacts become visible. To study these artifacts one can expand Eq. (3.21) to the second order and neglect the first two orders. As for the first order artifacts, it is possible to demonstrate that the reconstructed image $\hat{O}$ depends again on G only, with the dependence of the object influencing that can be considered almost a constant the majority of the times. The reconstructed image, in the second order approximation, can then be written as:

$$\hat{O} \propto \rho I \int \int_{\vec{r_i}} \frac{|\vec{r_i}|^2}{(z^2 + |\vec{r_i}|^2)^2} G'(\vec{r_i}) d^2 \vec{r_i} \tag{3.25}$$

where ρ is the opening fraction of the mask and I the object moment of inertia. For the MURA mask family, this equation makes the artifacts appearing as the symmetrical halos visible in Fig. 3.14 and 3.15. Their reduction is possible thanks to the ideal correlation properties of the (A,G) pair and its negative (1-A, -G). Here, 1-A is a mask, called anti-mask, in which the open elements are replaced with closed one and vice versa, while -G is the kernel generated from the anti-mask, which can be obtained by simply changing the sign in the generation algorithm. Recalling equation (3.6) and substituting (A,G) with its negative, one obtains:

$$
\begin{aligned}
\hat{O} &= [O' * (1 - A')] \otimes (-G) \\
&= O' * [(-G) \otimes (1 - A')] \\
&= O' * [1 \otimes (-G) + G \otimes A] \\
&= O' * (const + \delta) \\
&= O' + const.
\end{aligned}
\tag{3.26}
$$

The anti-mask, despite a constant term, can thus be used as a system with perfect imaging capabilities. The importance of this results is that, while the reconstruction of the image using the anti-system is the same, the artifact in Eq. (3.24) and (3.25) depends on G only and thus changing its sign also changes how the artifacts are generated. Using a combination of two optical systems in which one uses the anti-mask instead of the mask, one should be able to enhanced the object reconstruction while the artifact should cancel each other. Figure 3.16 shows the results obtained from the simulation of a squared and linear source. The simulations were performed with the optical systems in the same position, making the setup impracticable but useful in the understanding of these type of artifacts. The final result of the combination of the simulations is also visible, where the intensity of each pixel of the final image is calculated as the product of the intensity of each pixel of the image obtained using the mask with the same pixel of the image obtained using the anti-mask.

Simulated	Mask	Anti-Mask	Combined
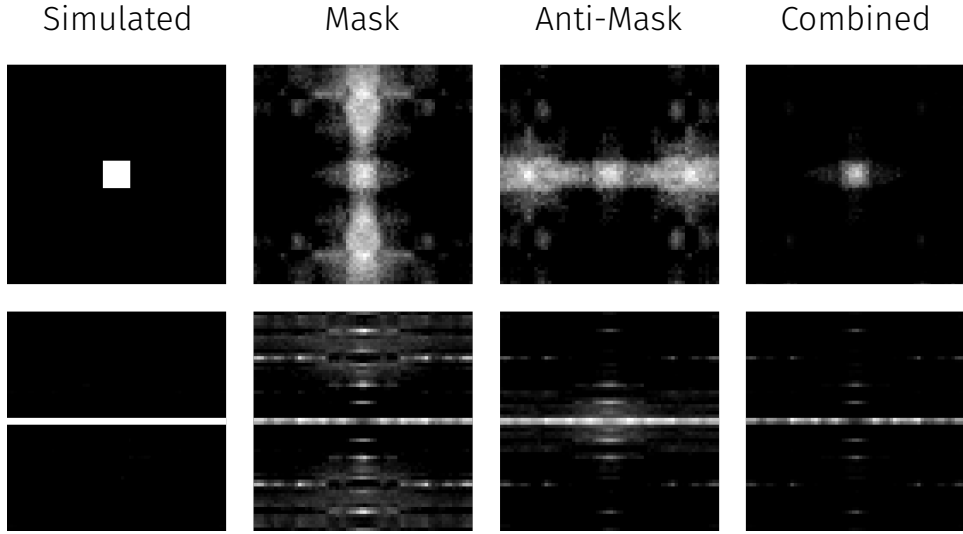
Figure 3.16: Results of the simulation of a squared and a linear source with and without second-order correction.

3.3.2 Depth of Field

Differently from the lenses, whose focal length is defined by construction, a coded aperture camera should provide an infinite depth of field. This should permit to focus tracks at every distance and allows a more easy reconstruction compared to the lenses. In reality, the presence of the sampling artifacts described above limits the reconstruction capability of a coded aperture camera, acting like a limitation of the depth of field.

Recalling the fact that these artifacts arise for value of α different from an integer (commonly 1), one could build a camera with a defined distance at which $\alpha = 1$ and, studying the variation of α respect to the variation of a, one could define the region in which the camera is still able to reconstruct the image. This region can then be seen as the DOF of the coded camera. The variation of α respect to the variation of a is defined as:

$$\frac{d\alpha}{da} = -\frac{p_m b}{p_d a^2} \tag{3.27}$$

with p_m, p_d the dimension of the mask's elements and detector's pixel respectively.

As can been seen, since p_m, p_d are commonly similar to each other, these variations are really small for a camera with $\alpha = 1$ at large distance from the mask (large alpha) while they are bigger for a camera with $\alpha = 1$ at small distance from the mask (small alpha). One could then expect a coded camera with large alpha to have an almost infinite DOF and a camera with a small alpha to act as a camera with a really small DOF. To test this property, two simulations have been performed: one using a camera with small alpha and one with large alpha. For both the simulations a track contained in a plane parallel to the one of the optical system, and at different distances from it, has been generated

67

(Fig. 3.17a). For the simulation with large alpha, a second track contained in plane oblique with respect to the optical system's plane has been also generated (Fig. 3.17b). In addition, every simulation has been performed using a traditional lens camera, to evaluate the differences of the DOF from one system to the other.
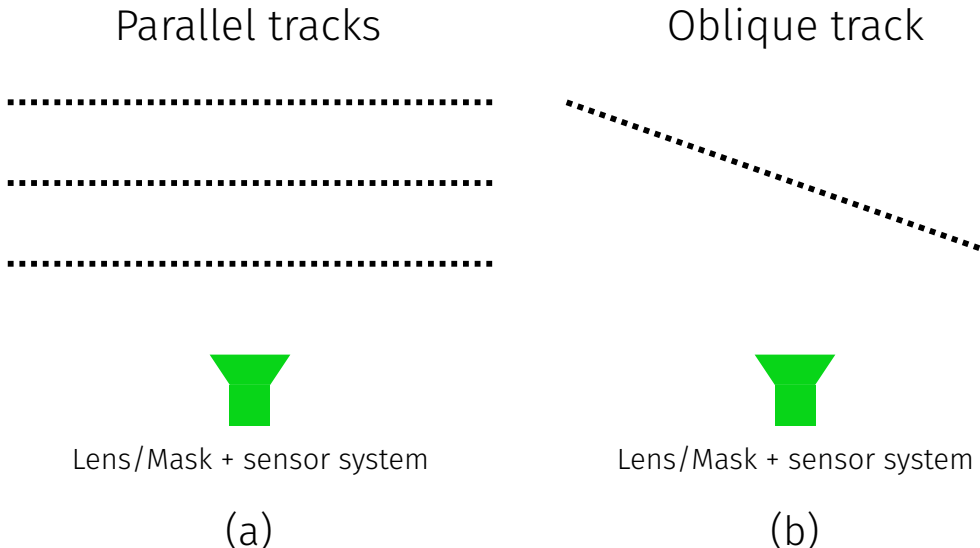

Figure 3.17: Schemes of the simulated tracks.

The results are showed in Fig. 3.18, 3.20 and 3.19. As can be seen, using lenses, the limited depth of field makes possible to correctly reconstruct the tracks only in the cases in which the track is near the focus distance. Differently, using the large alpha camera, the tracks can be reconstructed independently from the distance from the detector, confirming the hypothesis of almost infinite depth of field of this configuration (Fig. 3.18). At the same time, small variations of the distance of the source make the small alpha camera unable to reconstruct the track, confirming the limited DOF of this configuration (Fig. 3.19). From Eq. (3.27) one can see that the distance b, the mask-sensor distance, influences also the depth of field of the coded camera. To maximize the DOF one should then minimize such distance. Small values of b, however, make the reconstruction capability of the camera drop. This is due to the fact that at small values of b, the projected shadow of the mask generated by every source is similar to the one generated by a centered point source at infinite distance. As a result, small values of b make every track to be reconstructed as a point in the center of the sensor. At the same time, an increase of the value of b makes the sampling artifacts more evident, limiting the DOF. The minimal value of b for which the reconstruction could occur is then the value for which the maximal DOF of the camera is achieved. This behavior can be seen in Fig. 3.21, where a track at different distances from the mask is reconstructed using a camera in which only the mask-sensor distance changes from one case to the other.
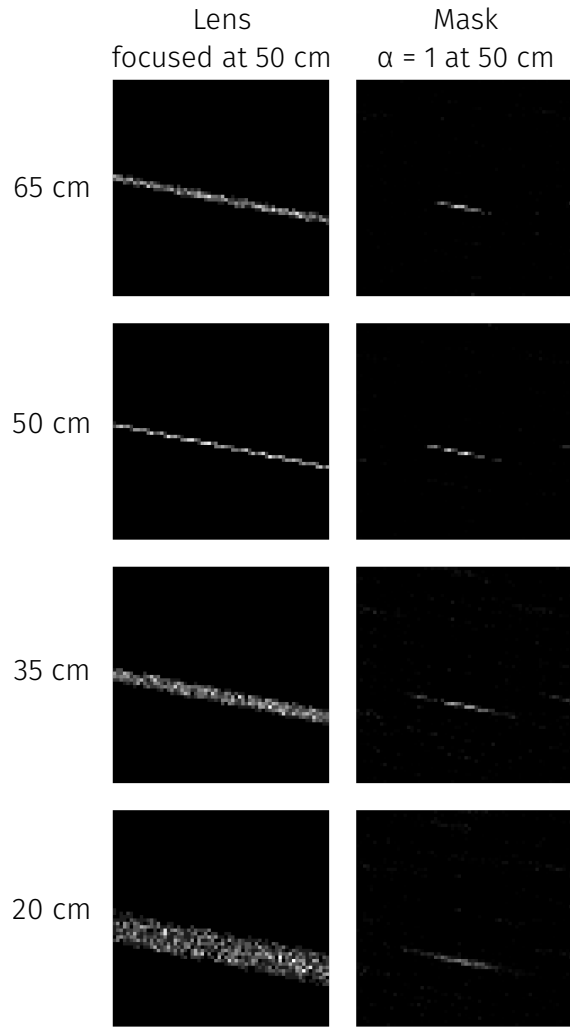
Figure 3.18: Results of the simulation of a track contained in a plane parallel to the plane of the optical system at different distance from it: 65 cm, 50 cm, 35 cm and 20 cm from the top to the bottom respectively. The left column shows the results obtained using a lens camera arranged to focus object at 50 cm from the lens while the right column shows the results obtained with the coded camera arranged to have $\alpha = 1$ at 50 cm from the mask. The different length of the track is due the different FOV of the two cameras.

To disentangle the problem of the depth of field, the same correction of the Near-Field Artifact, with the mask and anti-mask systems in the same position, has been performed. Due to the impossibility to use the systems in the same position, Fig. 3.18, 3.20, 3.19 and 3.21 represent an ideal scenario not completely reproducible when simulating and reconstructing real events.
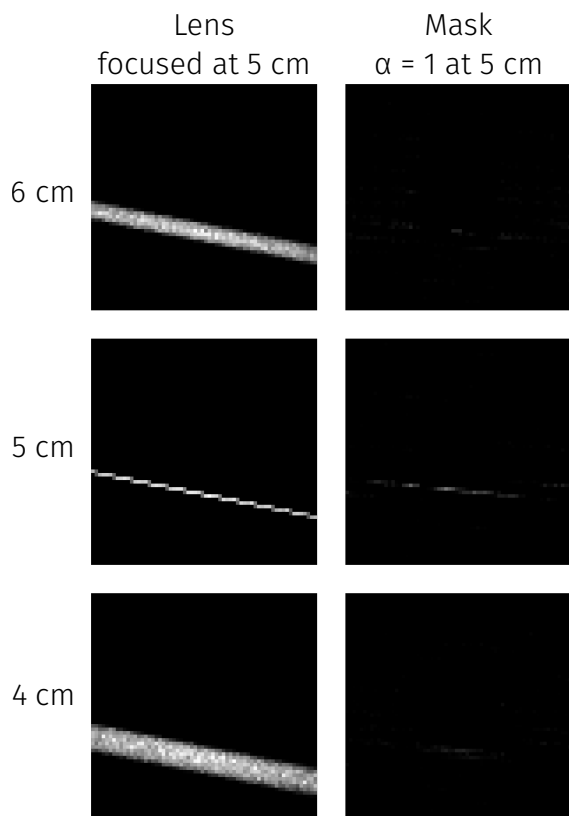
Figure 3.19: Results of the simulation of a parallel track at different distance from the camera: 6 cm, 5 cm, 4 cm from the top to the bottom respectively. The left column shows the results obtained using a lens camera arranged to focus object at 5 cm from the lens while the right column shows the results obtained with the coded camera arranged to have $\alpha = 1$ at 5 cm from the mask. The different length of the track is due the different FOV of the two cameras.
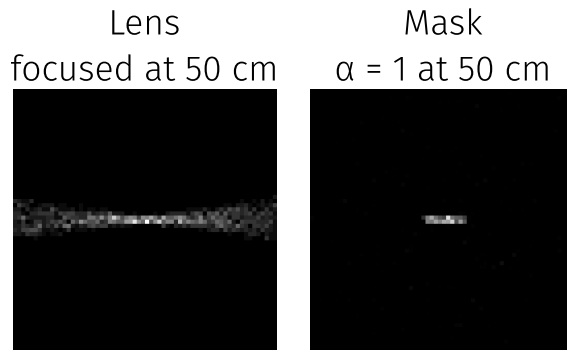
Figure 3.20: Results of the simulation of a track contained in a plane oblique with respect to the plane of the camera. On the left is showed the result obtained using a lens camera arranged to focus object at 50 cm from the lens while on the right is showed the result obtained with the coded camera arranged to have $\alpha = 1$ at 50 cm from the mask. The different length of the track is due the different FOV of the two cameras.
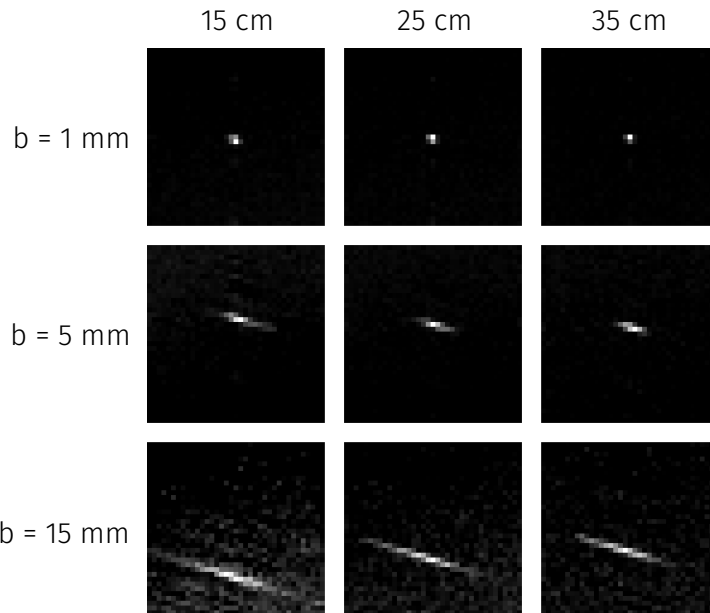
Figure 3.21: Results of the simulation of a parallel track at different distances from the camera: 15 cm, 25 cm, 35 cm from the left to the right respectively for a camera with b = 1 mm (top row), 5 mm (central row) and 15 mm (bottom row). The camera is arranged to have $\alpha = 1$ at 25 cm from the mask. The different length of the track is due the different FOV of the configurations.

71

3.3.3 Granularity

As already mentioned, to obtain perfect image capabilities using the coded aperture, one needs to project the full shadow of the mask on the detector. This has the implication that every pixel beyond an hole of the mask should be illuminated. If this is not the case, Eq. (3.7) is not valid anymore as A' is not correctly projected and the reconstruction capabilities drop.

Two main parameters can influence the correct projection of the mask: the intensity of the source and the granularity of the detector. These are actually connected to each other, as the intensity of the source puts a limit on the maximal allowed granularity and, vice versa, the granularity puts a limit on the minimal intensity of the source.

In fact, keeping constant the number of the emitted photons, the count on each pixel beyond an hole decreases as the size of the pixel also decreases. When the size is too small, some pixels could start to not count any photon, making the hole above it act like an opaque region of the mask and making the condition (3.7) not valid anymore. The reconstruction capability for a coded camera then decreases as the number of unlit pixels increases. A similar result is obtained keeping constant the size of the pixels and decreasing the source intensity.

Unlike the coded camera, a camera based on the use of lenses doesn't have this kind of limitations. This is possible due to the absence of a decoding process and due to the converging power of the lenses. This makes possible to increase the granularity of the sensor and to detect low intensity sources.

Figures 3.22 and 3.23 show the behaviors of a coded camera and of a traditional one based on lenses. Figure 3.22 shows the results obtained from the simulation of a linear source of different intensity for both the systems. It is possible to see how the coded camera results, even after the artifact corrections, rapidly deteriorate as the intensity of the source decreases. The system using lenses, however, is able to correctly reconstruct the source, even with a small number of illuminated pixels, for every simulated source intensity. Figure 3.23 shows the results obtained keeping constant the source intensity and the detector dimension and changing the size and number of the pixels. It is easy to see the differences of the two systems discussed above: while for the coded camera the increased granularity makes impossible to reconstruct the source, for the lens based camera the reconstruction is almost unaffected by the increased granularity, with the only consequence as the presence of some unlit pixels. In some situations then, the lens camera could be a better option compared to the coded camera, thanks to the absence of the artifacts and the possibility to increase the granularity of the sensor.
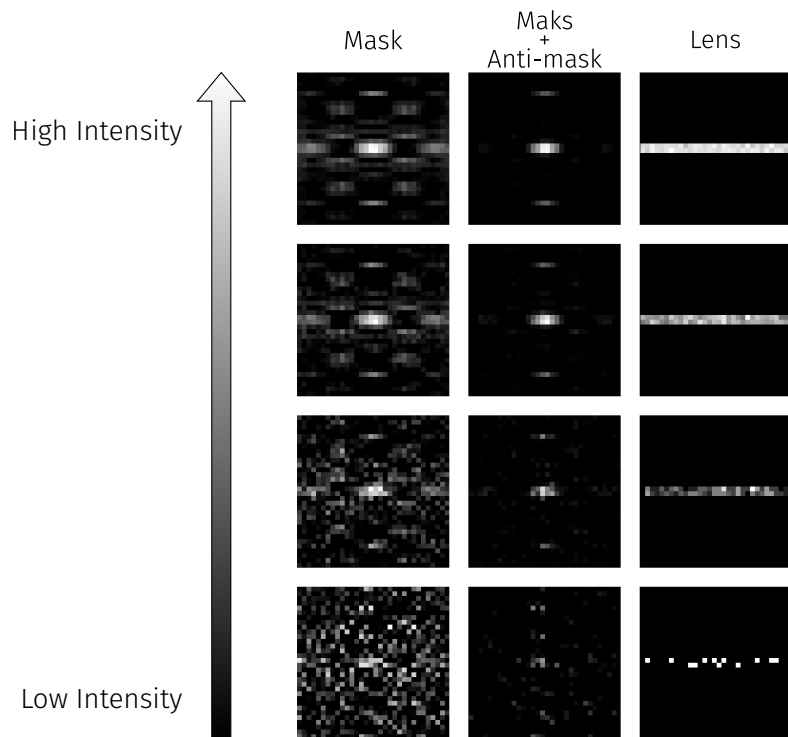
Figure 3.22: Results of the simulation of a linear source with decreasing intensity from the top to the bottom. The different length of the track is due the different FOV of the two cameras.
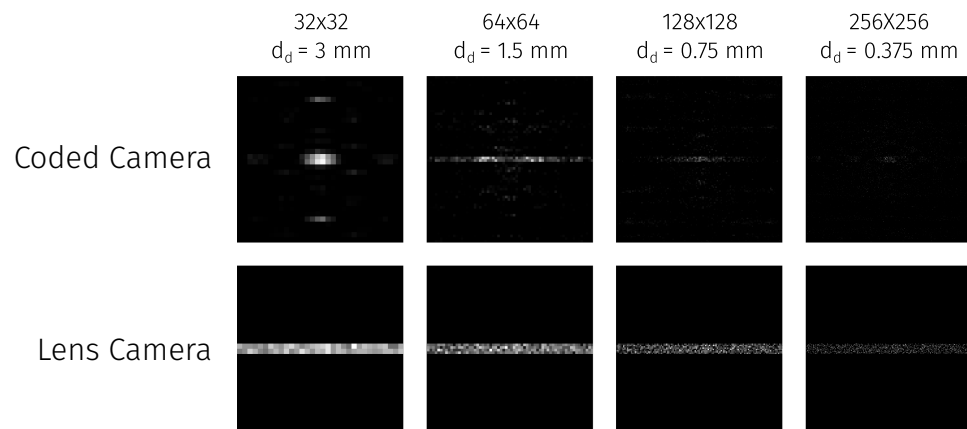

Figure 3.23: Results of the simulation of a linear source with sensors of same active area and different granularity. The different length of the track is due the different FOV of the two cameras.

Chapter 4

Simulation and Analysis

In this chapter the simulation used to study the feasibility of a detector as described in the previous chapter is presented, together with the optimization of the parameters and the analysis of the reconstruction capability of the detector.

4.1 The detector simulation

The detector simulation is composed by different steps, from the simulation of the geometry and the emission of scintillation light to the image reconstruction. The geometry and emission are simulated using the Geant4 toolkit[43], a toolkit for the simulation of the detector geometry and the passage of particles through matter frequently used in high energy, nuclear and accelerator physics.

4.1.1 Geometry and scintillation

The geometry of the detector is quite simple and it consists of a cubic box of Liquid Argon whose dimension will be discussed later in this chapter. The Liquid Argon is the scintillator material used to produce the light needed by the camera and its properties are summarized in Table 4.1.

The complete simulation of the emission and propagation to the faces of the box of the scintillation light requires high computational time due to the high number of photons emitted. For this reason, some approximations are used during this phase: the most important one is to not propagate each emitted photon using Geant4 but to save the position and direction of each photon to later perform the propagation. This has the consequence of not taking into consideration the photon's processes that could occur during the propagation time and that could change the result of the simulation. The dominant effect that should be taken into account is the photon absorption, which could decrease the number of photons able to reach the sensor on the faces of the detector.

Light yield	40 photons/keV
Photon's energy	[4.1, 10.61] eV
Refractive index	1.23
Fast time constant	7 ns
Slow time constant	1600 ns

Table 4.1: Properties of the liquid Argon used for the Geant4 simulation.

Simulation	Propagation	Photon Number
Geant4	Geant4	$1.62 \cdot 10^7$
Geant4	External without absorption	$1.74 \cdot 10^7$
Geant4	External with absorption	$1.67 \cdot 10^7$

Table 4.2: Comparison of the number of photons that reach the faces of the LAr box for the three different tested propagation methods.

To take this into account, the simulation of the photons' absorption is performed during the propagation with a hit-or-miss selection. Table 4.2 shows some results obtained from three different simulations: one in which emission and propagation are performed in Geant4, one in which the propagation is performed in a second time without the photons' absorption and the last one in which the absorption is also simulated. In the work presented for this thesis, the third approach is used.

After this first phase of the detector simulation, the position on the faces of the LAr box is known and could then be used to study the response of the sensor in the second phase. Figure 4.1 shows the projection of the trajectory of a simulated particle and the position of the scintillation photons on a lateral face of the box.

4.1.2 Optical system and sensor response

After the propagation of the scintillation photons, the second phase consists on the simulation of the optic-sensor system. The optical systems used in this thesis are a MURA mask in a 2×2 arrangement as described in Section 3.2.4 and a traditional converging lens. Both optical systems could be placed on every faces of the box and possibly repeated in a N×M grid on each face, as per Fig. 4.2.

Masks When the mask is used, for each propagated photon, its position is checked whether it passes or not through an open region of the mask. Every photon that reaches
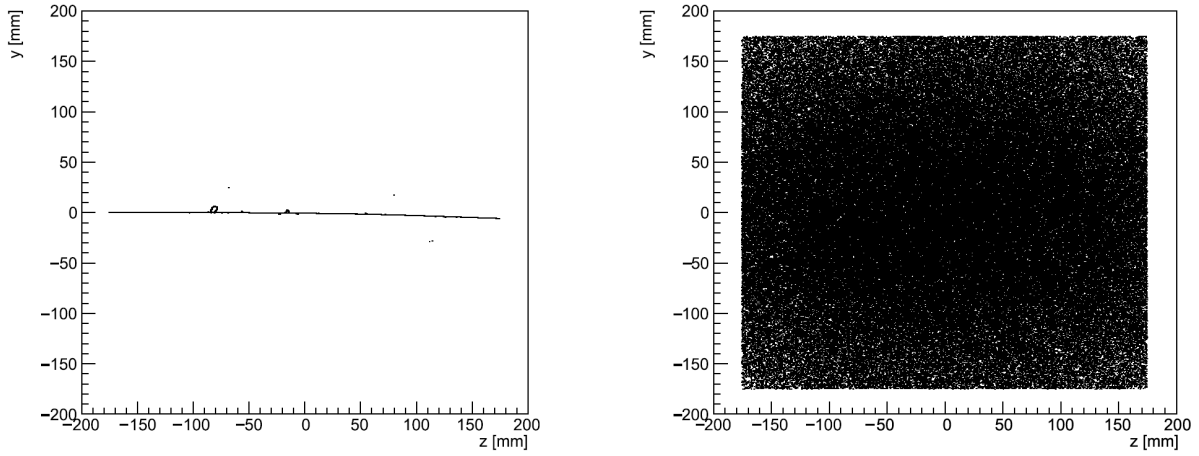
Figure 4.1: Lateral view of the origin points for the scintillation photons (left) and their position on a lateral face after the propagation (right).
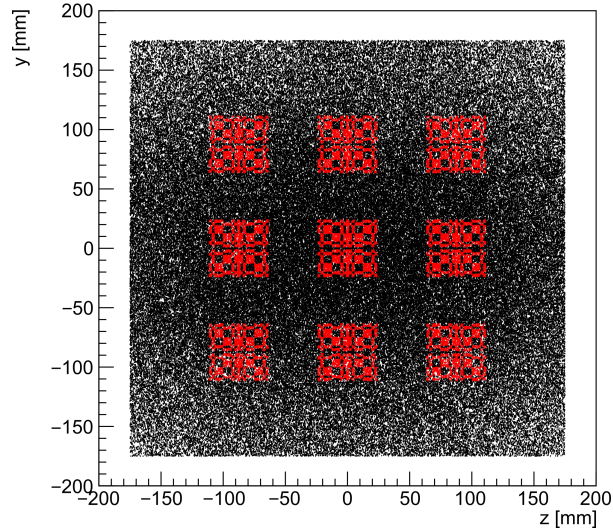

Figure 4.2: Example of a 3×3 grid of masks on one lateral face of the LAr box.

a face of the box outside the mask or that impinges a closed region of it is rejected. Figure 4.3 shows the result of this first cut.

The photons passing through the mask are propagated along the direction obtained from the Geant4 simulation to reach the sensor plane. The sensor is subdivided in a N×N grid of pixels and for every hit pixel the number of photons is counted. Figures 4.4 shows the photons survived at the first cut that reach the sensor as well as the number of the photons counted by each pixel respectively. When possible, a complementary system composed by an anti-mask and a second sensor is placed right on the side of the
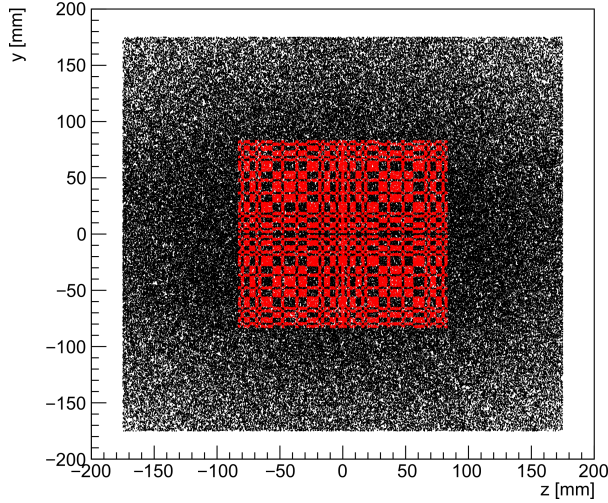
Figure 4.3: Position of the photons on a lateral face of the LAr box after the propagation (black) and photons that pass through the mask and survive the first cut (red).
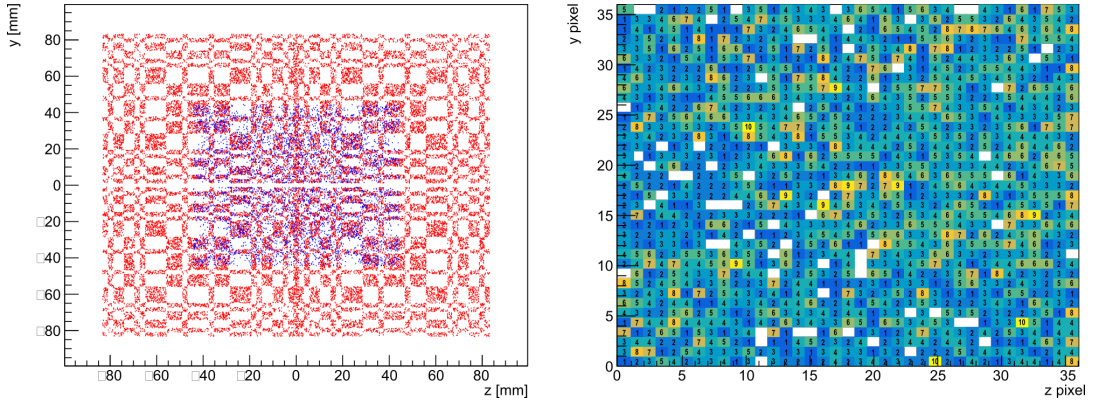
Figure 4.4: Left: Position of the photons that pass through the mask and survive the first cut (red) and photons that reach the sensor (blue). Right: Number of photons that hit each pixel of the sensor when using a mask as optical system.

mask-sensor system as per Fig. 4.5.

Lenses When using the lens, the procedure is similar to the one described for the mask, with the first cut used to reject all the photons that do not impinge the lens (Fig. 4.6) and the propagation from the lens to the sensor performed using the ray transfer matrix analysis technique and assuming the lens as a thin lens.

This technique is valid only in the paraxial approximation, in which the direction of the scintillation photons is at a small angle with respect to the optical system of the lens and can be used to perform the ray tracing of the photons that pass through the lens.

77
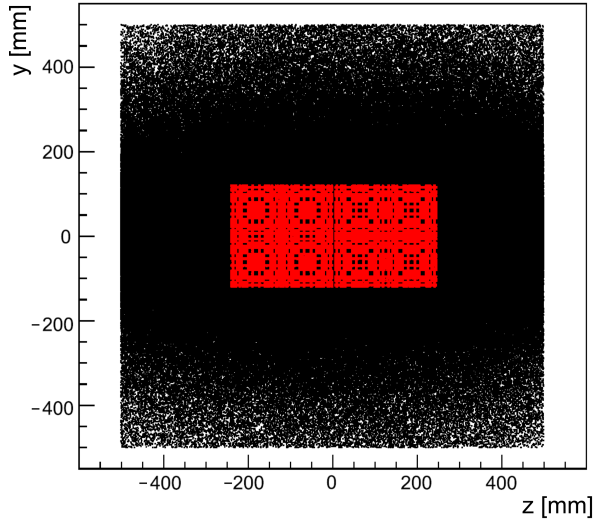
Figure 4.5: Position of the photons on a lateral face of the LAr box after the propagation (black) and photons that pass through the mask (red, left) and the antimask (red, right) and survive the first cut.
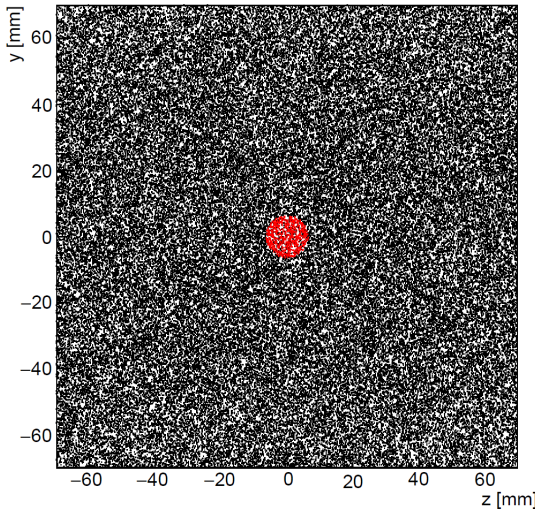
Figure 4.6: Position of the photons on a lateral face of the LAr box after the propagation (black) and photons that impinge on the lens and survive the first cut (red).

Using this technique then, the position and direction of a photon that comes out of the lens can be calculated as:

$$\begin{bmatrix} x_2 \\ \theta_2 \end{bmatrix} = \begin{bmatrix} A & B \\ C & D \end{bmatrix} \begin{bmatrix} x_1 \\ \theta_1 \end{bmatrix} \tag{4.1}$$

where x_1 and θ_1 are the position at which the photon impinges on the lens and its direction respectively, x_2 and θ_2 are the position at which the photon comes out from the lens and its new direction respectively and the matrix, in the case of the thin lens approximation, is defined as:

$$\begin{bmatrix} A & B \\ C & D \end{bmatrix} = \begin{bmatrix} 1 & 0 \\ -\frac{1}{f} & 1 \end{bmatrix} \tag{4.2}$$

with f as the focal length of the lens. The photons are then propagated along the new direction to reach the sensor's position and, as with masks, for every hit pixel the number of photons is counted (Fig. 4.7).
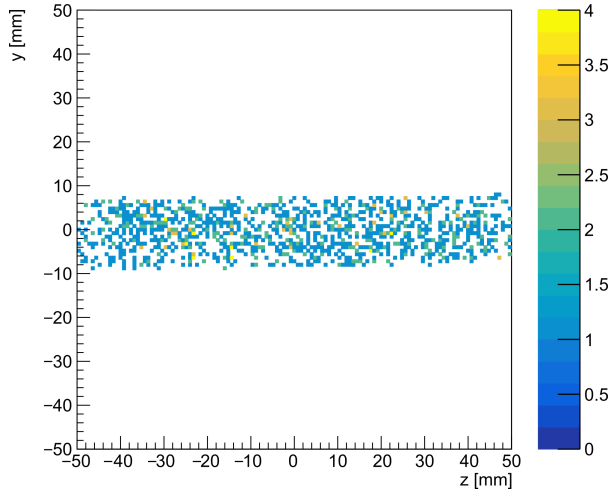
Figure 4.7: Number of photons that hit each pixel of the sensor when using a lens as optical system.

4.1.3 Image reconstruction

Using the lens, the sensor's response is already the final image and no other manipulation of the signal is needed. Figure 4.8 shows some examples of final images obtained with the lens camera.

Using the mask as optical system instead, the deconvolution process of the signal obtained by the sensor is needed to obtain the final image. This process is performed as described in Section 3.2.1, with the deconvolution matrix obtained using the algorithm in Eq. (3.11) and the response matrix obtained from the previous phase of the simulation. The same reconstruction process is used for both the mask and the anti-mask systems. An image obtained from the mask system will be referred as mask-image while the one obtained using the anti-mask system will be the antimask-image. During this phase, the information on the field of view of the camera (Eq. (3.14)) and on the initial position of
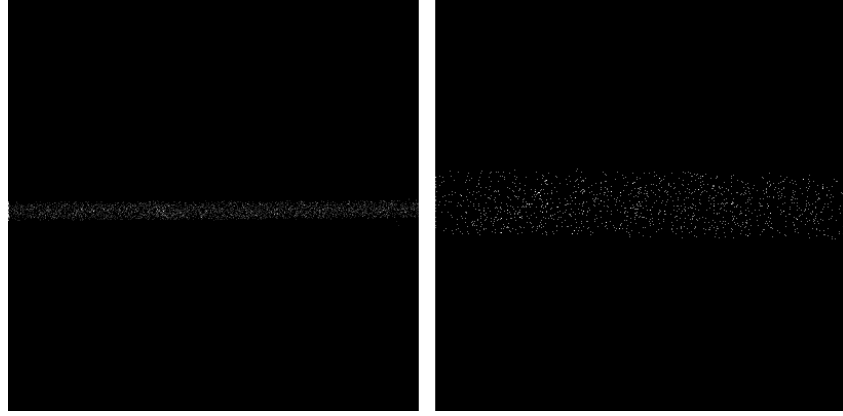
Figure 4.8: Example of reconstructed images obtained using lenses.

the emitted photons obtained from the Geant4 simulation allow to also reconstruct an ideal image of what the camera see. Figure 4.9 shows the result of these reconstructions as well as the combination of the mask-antimask images (sum of the mask-antimask images).
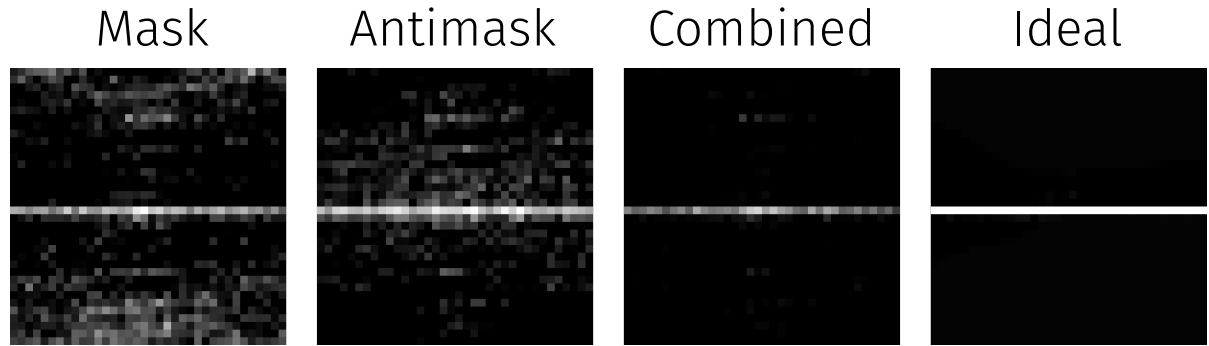

Figure 4.9: Example of reconstructed images obtained using masks.

Starting from these reconstructed images in the next Section it will be studied the performance of the detector in correctly reconstructing the simulated tracks.

4.2 Parameters optimization

Many parameters are involved in a detector as the one here simulated and their values could have a major impact on the camera's reconstruction capability. The definition of the ideal parameters' values is thus needed to obtain the maximal reconstruction capability. Due to the fact that this thesis is part of a project which aims to build a prototype of this detector, the values of some parameters are constrained by the hardware planned to be used.

4.2.1 Pixel size and box dimension

The sensor that will be used in the prototype of the detector will be a matrix of N×N squared Silicon Photon Multipliers of 1.2 mm of side. This defines the dimension of the simulated pixels at exactly the same size of the prototype pixel or, possibly, to an integer multiple of it. This will be possible combining multiple signals in one single signal, as per Fig. 4.10.
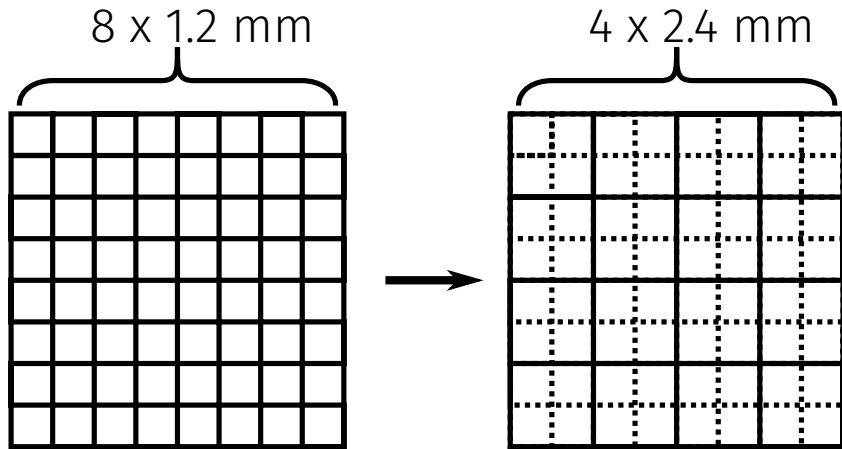

Figure 4.10: Example of one possible pixel combination.

To test whether a 1.2 mm pixel matrix could be used in the prototype, a complete simulation like the one described above has been performed and repeated several times with different distances between tracks and mask. For each simulation, the pitch of the mask has been changed to guarantee an integer value of the parameter alpha (Eq. 3.18). This is needed to find the maximal distance at which the detector is able to reconstruct the images in ideal condition. As showed in the previous Chapter, small sized pixels need high intensity sources and increasing the distance of the tracks could imply that not sufficient light reaches the sensor. Figure 4.11 shows the results of these simulations. It is visible how the scintillation light is not enough to reconstruct the image already at small distances from the mask. To verify the capability of the camera to reconstruct the tracks, a track finding algorithm, described in Appendix A, has been developed. The algorithm is able to find a track in the correct position only for the first image of Fig. 4.11, meaning that a 1.2 mm pixel could not be suitable to be used in the prototype. The same simulations then have been performed with a 2.4 mm side pixels, keeping the same number of pixels, to test whether the increased area of the pixels is enough to reconstruct the tracks. Figure 4.12 shows the results, where the effect of the increased pixel size is evident. Despite the high background noise of the images, the camera is able to reconstruct tracks up to some tens of centimeters and the algorithm correctly finds the track in every image. The choice to simulate tracks up to the distance of 35 cm is due to the fact that the final prototype will have a dimension comparable with this value
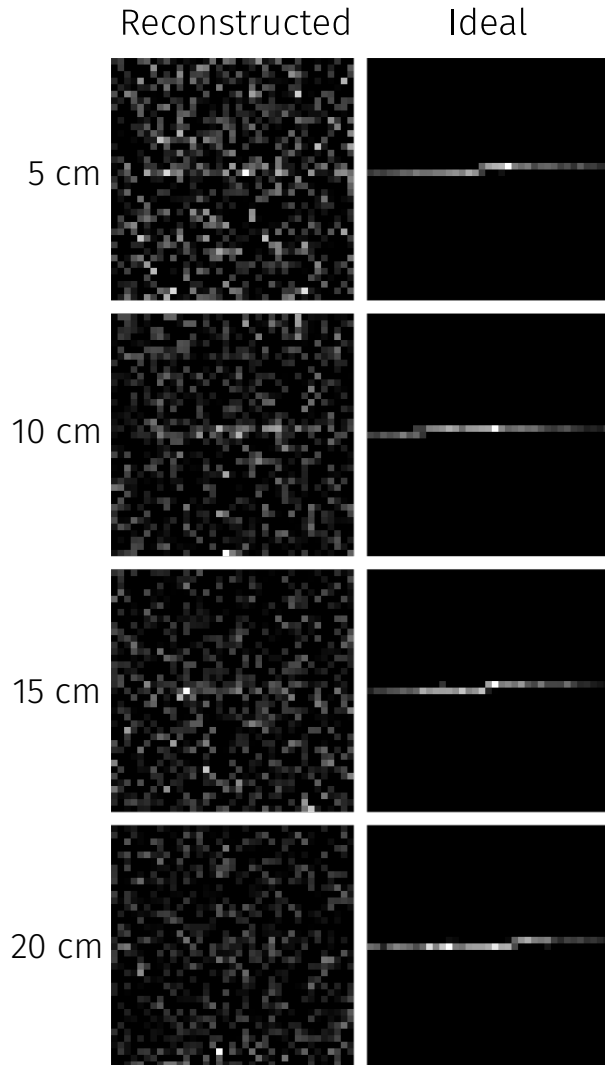
Figure 4.11: Reconstructed images using a 1.2 mm pixel for tracks at 5, 10, 15 and 20 cm from top to bottom respectively.

and bigger sizes are not yet needed. At the same time, increasing the distance, the FOV of the camera also increases, meaning that the farthest tracks could be seen as too short to be reconstructed. The final configuration regarding pixel size and box dimension is thus with pixels of 2.4 mm side and a LAr box of 35 cm side.

4.2.2 Mask-sensor distance and sensor efficiency

Another parameter that has to be optimized is the mask-sensor distance. Following the results obtained in Section 3.3.2, this distance has an ideal value that provides

Reconstructed   Ideal
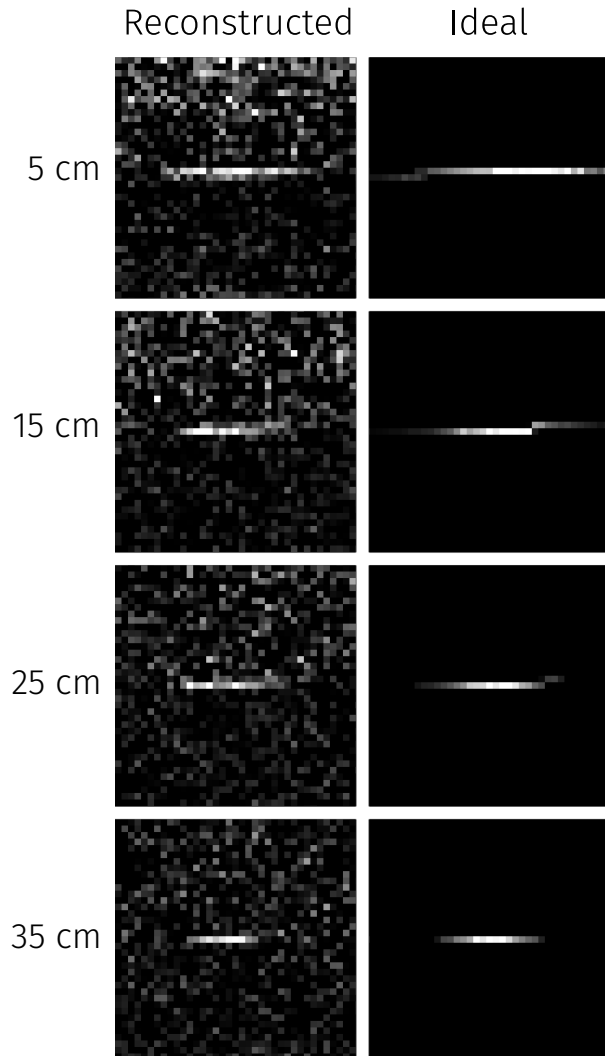
Figure 4.12: Reconstructed images using a 2.4 mm side pixel for tracks at 5, 15, 25 and 35 cm from top to bottom respectively.

the maximal reconstruction capability and reduces the amount of artifacts due to the variation of alpha. To ease the construction of the detector, however, this value has been chosen to be 5 mm. This value, despite not being the optimal one, is small enough to reduce the amount of sampling artifacts while still providing good track reconstruction.

The sensor's efficiency is also constrained by the available hardware and, since the estimated efficiency of the pixel matrix of the prototype is of about 50%, this value is the one used during the simulations.

4.2.3 Mask pitch and alpha

After the definition of the pixel size, the scintillator dimension and the mask-sensor distance, the camera has to be arranged in a way that the artifacts are minimized. This is performed scanning different values of the mask pitch to find the ones that maximize the region of the LAr volume in which the variations of alpha are minimal. Figure 4.13 summarize the procedure used to find such a value. First, a maximal value of the allowed variation of alpha has been chosen. This value is ±4% and has been chosen empirically from the study of the artifacts of the previous chapter. After that, different values of the mask's pitch are tested to find the one that maximizes the region of the LAr volume within the $\alpha = (1 \pm 0.04)$ band. The maximal region is found with a value of the pitch
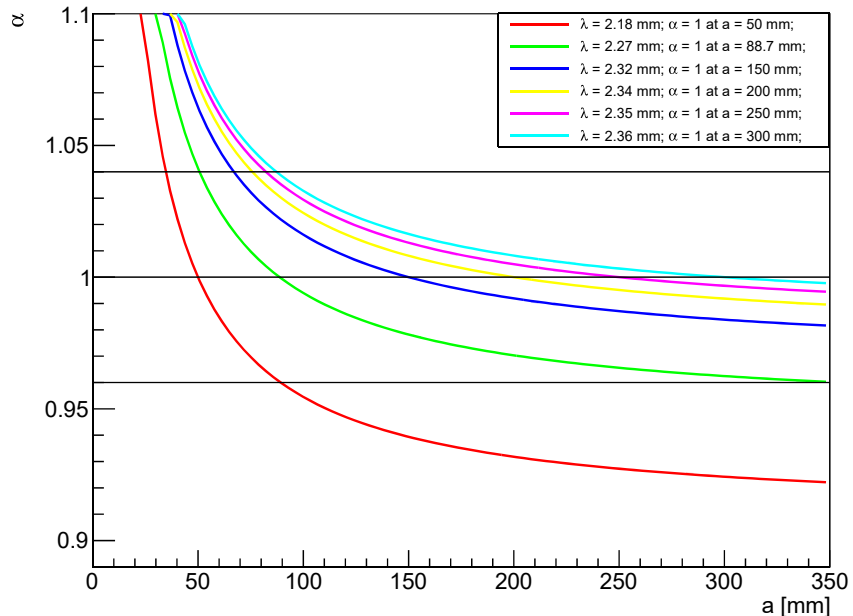
Figure 4.13: Plot of α as a function of the distance from the mask for different values of the mask's pitch. The green line is the line that maximizes the region included in the ±4% region.

of 2.272 mm but, due to the limit on the fabrication precision, the value is rounded at the hundredth of a millimeter precision. The closest value that maximizes the region is then 2.28 mm. Table 4.3 shows the results obtained with the value of 2.272 mm as well as the ones obtained with the two closest rounded values.

	$a(\alpha = 1)$	$a(\alpha = 0.96)$	$a(\alpha = 1.04)$	Covered distance
$\lambda = 2.27$	87.31	50.22	333.82	283.6
$\lambda = 2.272$	88.75	50.71	350	299.29
$\lambda = 2.28$	95	52.78	350	297.

Table 4.3: Results of the minimal and maximal values of a included in the $\pm 4\%$ region for the best value of λ and the two closest, rounded, values. Units are in mm.

4.2.4 Lens

Due to the different type of analysis and performances of the lens camera, and the higher granularity of the sensor with which is still possible to reconstruct tracks, the simulated sensor has pixel size of side 0.1 mm. A SiPM sensor of this type is not currently available to be used in the prototype and its simulation has the purpose to verify the maximal performance of a detector with lenses as optical system.

The lens specifications are obtained from the *eSource Optics* catalog. To reconstruct the higher number of tracks in the volume, the chosen lens is the one from the catalog with the higher D/f ratio, where D is the lens diameter and f its focal length. The need of a larger diameter is to collect the higher amount of light while the short focal length allows most of the tracks to be reconstructed as real images on the sensor. Due to the lens being simulated as a thin converging lens, tracks whose position is closer to the lens than the focal length are reconstructed as virtual images, and it is thus not possible to reconstruct the images on the sensor. Table 4.4 summarizes the lens' specifications.

The last parameters to be optimized are the distance at which the camera is focused and the lens-sensor distance. Due to the thin lenses approximation used in the simulation, these quantities are in relation through the thin lens equation:

$$\frac{1}{f} = \frac{1}{S_1} + \frac{1}{q} \tag{4.3}$$

where f is the lens' focal distance, S_1 is the desired focused distance and q is the lens-sensor distance, as in Fig. 4.14. As it will be explained later, the focused distance should be the closest possible to the lens and to the focal length while keeping the lens-sensor

Diameter	25.4 mm
Focal Length @ 157nm	31.2 mm
Transmission Efficiency	90%

Table 4.4: Lens' specification as obtained from [44].
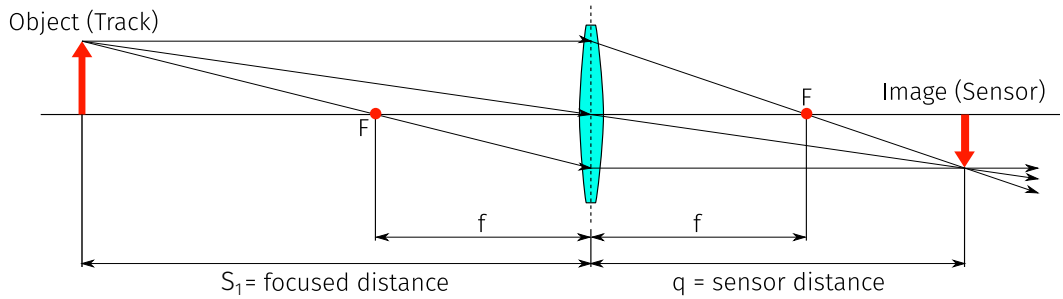
Figure 4.14: Scheme of the important distances for a thin lens camera.

distance sufficiently small to ease the detector construction. Figure 4.15 shows the lens-sensor distance as a function of the focused distance with $f = 31.2$ mm. Excluding the
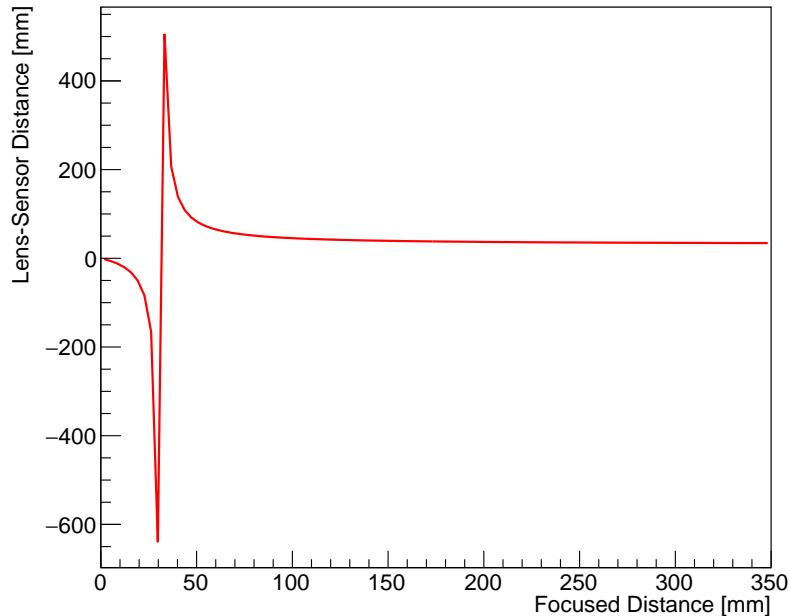

Figure 4.15: Lens-sensor distance as a function of the focused distance.

distances smaller that the focal length, for which the reconstructed images are virtual images and the lens-sensor distance is negative, the chosen focused distance is 4 cm. This value defines a sensor distance equal to 14.2 cm and it has been chosen since smaller values make the sensor distance rapidly rise up to 50 cm while larger values could generate ambiguities in the analysis, as explained in the next section.

4.3 Analysis strategy

After the optimization of the detector, different analyses have been performed to study its performance. The strategy used with the mask is different from to the one used with the lens but in both cases the aim is to study how well the detector can reconstruct the tracks in the correct position.

4.3.1 Simulated events

The particle track generation is common for both the mask and the lens. The simulated particles are muons of 1 GeV of energy and their position and direction at the generation level are sketched in Fig. 4.16. Each muon enters the box perpendicular to the back face and passes through the entire volume along the z-axis (Fig. 4.16a). Two different position along the y-axis have been simulated: one at half the volume height and one at 148 mm (27 mm) above the center when using masks (lens) as optical systems (Fig. 4.16b). The position of the muons along the x-axis has been modified to span half the volume length with steps of 25 mm: from 25 to 175 mm (Fig. 4.16c).
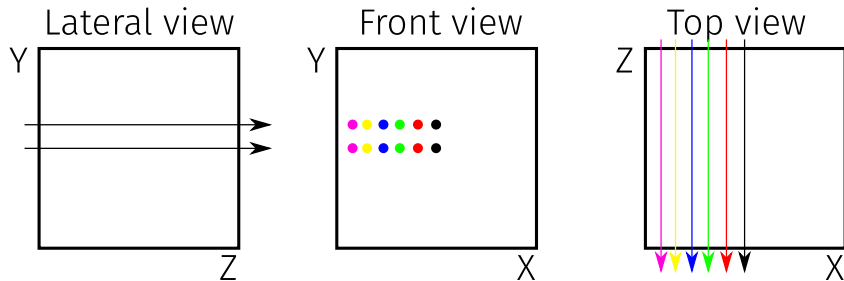
Figure 4.16: Lateral, front and top view of the muon positions and directions for each simulated configuration.

Using two optic-sensor systems, one on each lateral face of the LAr box, as in Fig. 4.17, it is then possible to reconstruct tracks at two distances for each simulation, covering all the possible distances from a mask in the volume. For each configuration, 20 different muons have been simulated. Each simulated muon will be referred as an event.

4.3.2 Masks analysis

From each simulation, the reconstructed images, obtained as described in Section 4.1, are analyzed. Two different types of analysis are performed: one to measure the quality of the reconstructed images and one to verify how well the muon tracks can be reconstructed.
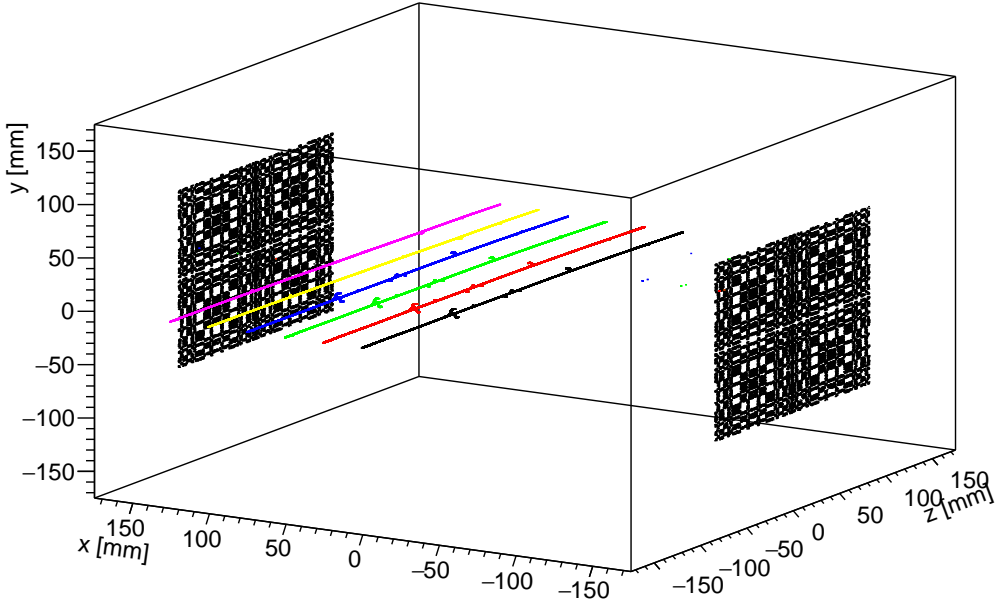
Figure 4.17: 3D view of the muon position passing through the center of the y-axis.

Images quality The quality of the reconstructed images is evaluated measuring its similarity with the ideal image. The similarity is measured using the Manhattan Distance, which is defined as[45]:

$$d(x, y) = \sum_i |x(i) - y(i)| \tag{4.4}$$

where x and y are the images that are being compared while $x(i)$ and $y(i)$ are the intensity of the same pixel of both the images. The sum is performed for all the pixels of the images. Using this metric, two identical images have a distance equal to zero, while different images have a distance that is bigger the more the images are different. To be able to use this metric, all the images obtained from the simulations are scaled in the range $[0, 255]$, where 0 is black and 255 is white. This distance is calculated for each event for each configuration and the mean value is taken.

Tracks reconstruction The track finding algorithm used in Section 4.2.1 is applied to analyze the images obtained from the muon simulations.

The analyzed image depends on the possibility to include or not the antimask system. In the case in which only the mask-sensor system can be placed on the box face, the used image is the one obtained directly from the reconstruction. When the antimask-sensor system is also included, the mask and antimask images are combined with the

88

final intensity of each pixel obtained as the sum of the intensity of the pixels of both the mask and antimask images:

$$I_{final}(i) = I_{mask}(i) + I_{antimask}(i). \tag{4.5}$$

The resulting image is the one analyzed by the algorithm.

It's worth noticing that this kind of image combination is possible only since both the systems reconstruct a straight track that passes through the entire FOV of the cameras. In a more complex situation, the different position of the cameras could imply that the reconstructed tracks are located in different position of the images. The combination of such images, in that case, could generate a final image whose quality is worse than the single images (Fig. 4.18) and a more refined combination algorithm could be necessary.
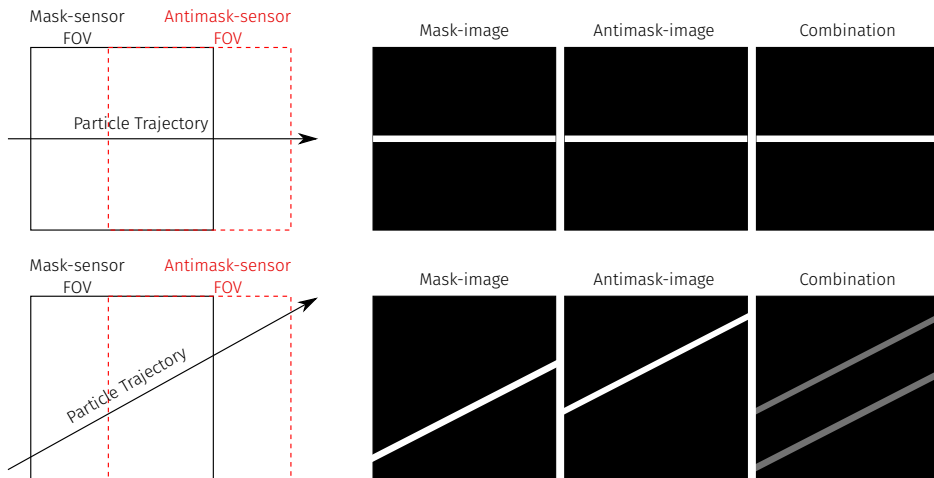
Figure 4.18: Representation of two possible combinations of the mask- and antimask-images. The need of a refined combination algorithm is evident in the bottom row, where the mask- and anti-mask images are different.

4.3.3 Lens analysis

The analysis performed using the masks cannot be applied to the lens due to the different type of reconstructed images. When analyzing the images obtained using lenses, the main problem is the width of the out-of-focus tracks, that makes the correct identification of the tracks position difficult. Many algorithms for the refocusing of the images exist but they are not directly applicable to remove defocus blurs in photographs with wide depth variations[46]. The chosen solution is thus to use the width of the blur to obtain information on the track position. This is possible using the Circle of Confusion (CoC). The CoC is the spot that is generated by the light rays when the focus is not ideal, as

shown in Fig. 4.19, and its dimension is defined as[47]:

$$c = A\frac{|S_2 - S_1|}{S_2}\frac{f}{S_1 - f} \tag{4.6}$$

where S_2 is the distance of the source, S_1 is the distance at which the camera is focused, A is the lens diameter and f the focal length (Fig. 4.20). Since S_1, A and f are defined,
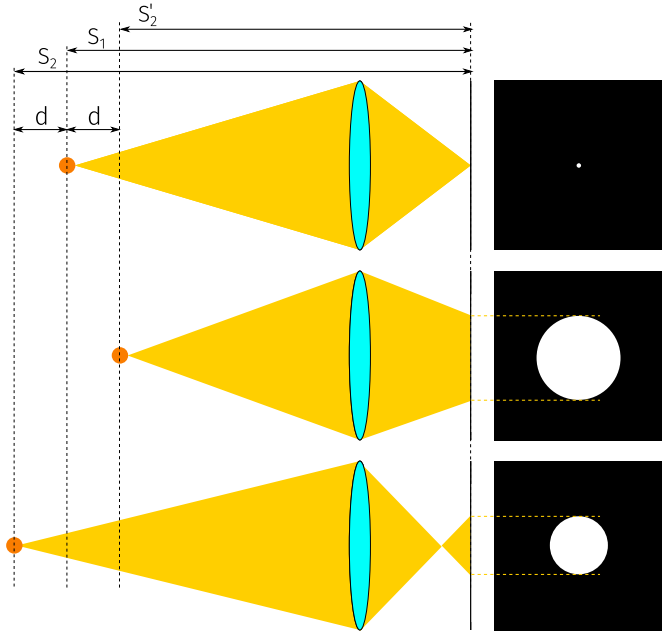

Figure 4.19: Representation of the Circle of Confusion (CoC) for in- and out-of-focus sources.

measuring the width of the CoC could give information on the distance of the track from the lens.

Due to the nature of the CoC, its value is zero when a track passes through the focused distance S_1 and increases as the track moves away from it, both approaching and moving away from the lens. This could be a source of ambiguities when measuring the track's position, as two possible solutions exist. It is thus important to reduce the region in which these ambiguities arise. As shown in Fig. 4.21, where the CoC dimension is plotted as a function of the track-lens distance, this region increases as the $S_1 - f$ distance increases. For the chosen value of $S_1 = 40$ mm this region goes from 31.2 mm (the focal length) to 48.8 mm. Every simulated configuration thus is outside the ambiguous region and the analysis method should be able to correctly identify the tracks' position. The only configuration for which the analysis cannot be performed is the one at 25 mm from the lens. These events, being closer than the focal length, are reconstructed as virtual images an cannot be analyzed.

90
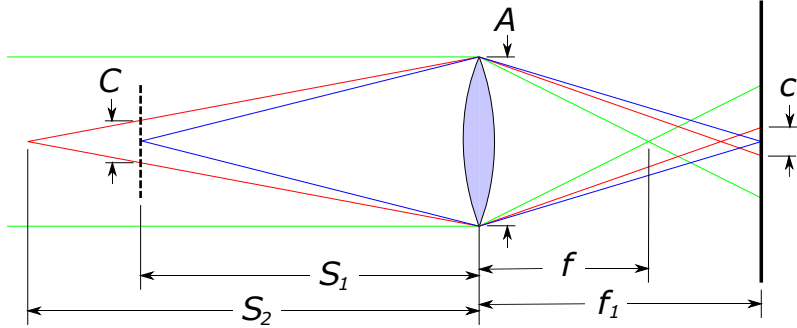
Figure 4.20: Scheme of the important quantities utilized in the measurement of the CoC width.
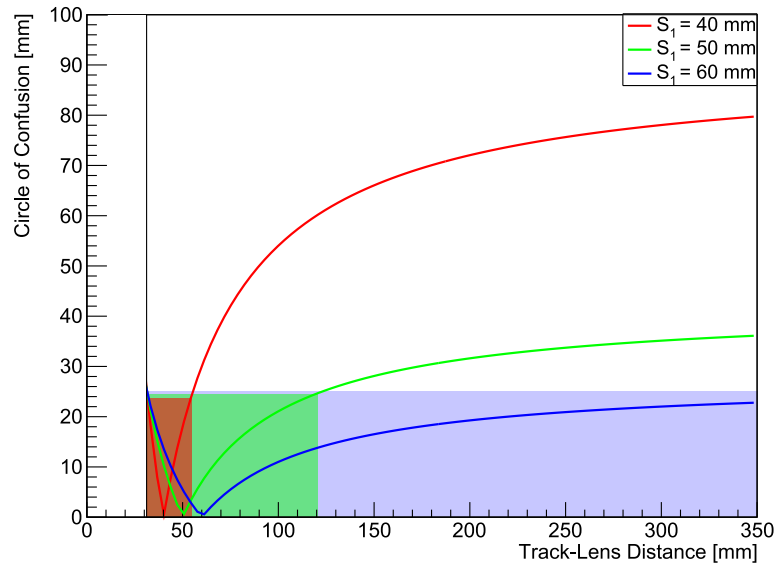

Figure 4.21: CoC's dimension as a function of the track-lens distance for different values of S_1. The vertical line indicates the focal length of the camera and thus the minimal distance from the lens for which the tracks can be reconstructed while the colored bands represent the ambiguous regions for each value of S_1.

Chapter 5

Results

In this Chapter the results of the simulation of the two optical systems presented in Chapter 4 are discussed in terms of track reconstruction performances and achievable detector resolution.

5.1 Mask results

The results described in this Section are obtained using two mask-sensor systems, with a sensor of 37x37 pixels (88.8×88.8 mm) and a mask whose rank is 37, that becomes a 73x73 mask when arranged in the 2x2 mosaic configuration (166.44×166.44 mm), both placed in the center of opposite box faces. Due to the dimensions of both the sensor and the mask, only the mask-sensor system could be used in this configuration while everything else is arranged as already described in the previous chapter. The events simulated along the center of the y-axis of the box are seen in the center of the coded camera and are thus called *on-axis* events. The events simulated 148 mm above the center are instead called *off-axis*.

5.1.1 Images quality

For each event of each simulation configuration, the Manhattan Distance (Eq. (4.4)) has been measured and the mean value of each configuration has been calculated. Figure 5.1 shows the results for one of the configurations, while Fig. 5.2 shows the measured distance and the comparison of the images for the ideal, best and worst case scenario between all the analyzed configurations.

   The final result of this analysis is showed in Fig. 5.3, where the mean value for each configuration is plotted as a function of the track-mask distance for both the on- and off-axis tracks. For the on-axis tracks, the behavior in Fig. 5.3 is coherent with what expected from the preliminary study of the artifacts: the maximal similarity to the ideal
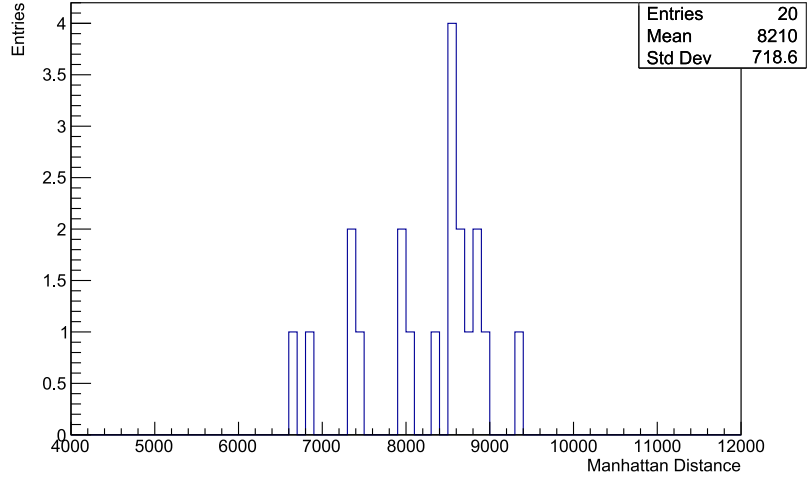
Figure 5.1: Distribution of the measurements of the Manhattan distance for the configuration in which the muons are generated at 15 cm from the mask.
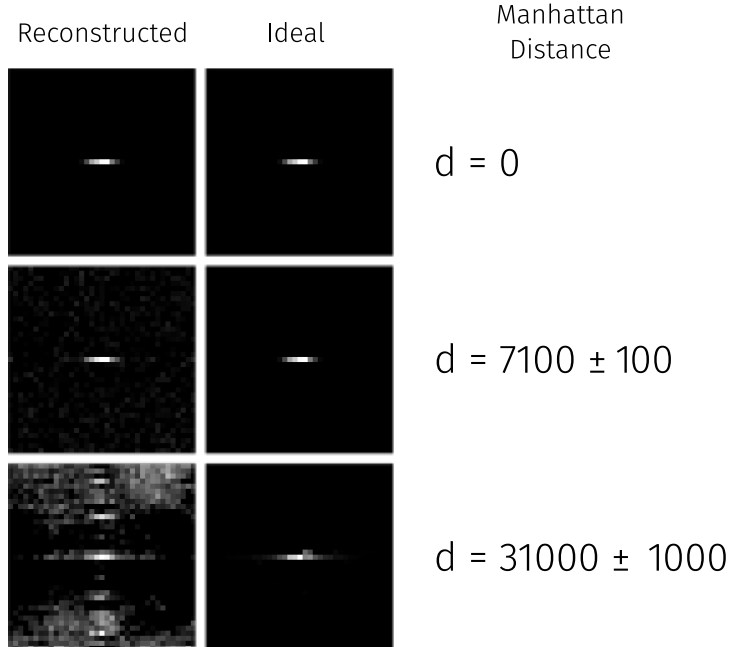

Figure 5.2: Comparison between the reconstructed images and the ideal one in an ideal case (top row), in the best case (central row) and worst case (bottom row) out of all the simulated configuration. For each comparison the Manhattan distance is also reported.

image is obtained with the muon at the distance closest to 95 cm, the distance at which $\alpha = 1$ and the farther from this value the muon is, the worst the quality becomes. The

slow deterioration of the image quality, as the distance from the mask increases, is in agreement with the slow variation of α at large distances, while, when the distance of the tracks decreases, the quality of the image rapidly worsens, as expected from the much faster variation of alpha at short distances from the mask. The point with the smaller track-mask distance (25 mm) needs an additional consideration, as this configuration is the only one in the near field region. The high value of the Manhattan Distance thus is mostly due to the near field artifacts and, in order to improve the quality of the image, the antimask-image is needed. Figure 5.4 shows the reconstructed images for the two closest distances from the mask (25 and 50 mm) for the on-axis configuration, where the halos generated by the second order artifacts are evident for the closest image at 25 mm. The
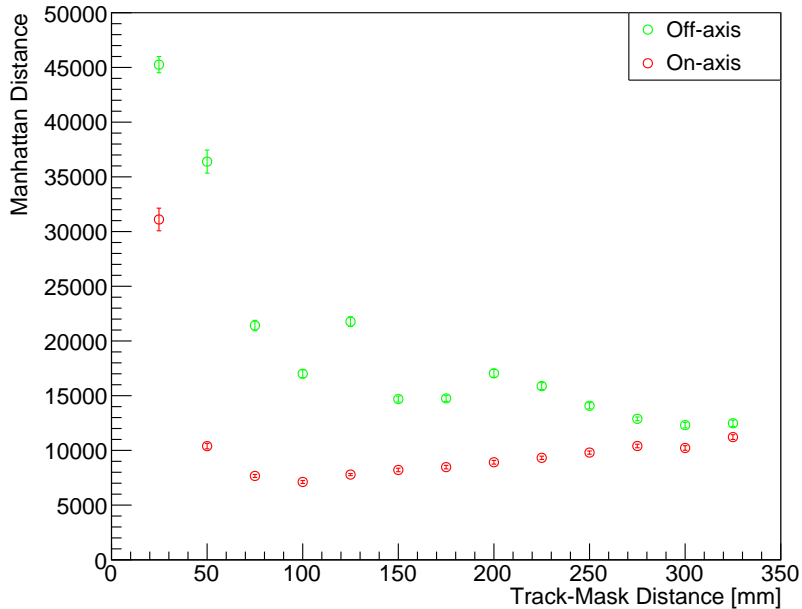

Figure 5.3: Mean value of the measured Manhattan distance as a function of the track-mask distance.

behavior of the results for the off-axis tracks is quite different from the on-axis one but is again coherent with what expected. The increased value of the Manhattan Distance for the configurations closer to the mask is due to the increase of the Near Field Artifacts. Recalling the first order artifacts of Section 3.3.1, the farther the object is from the center the more important these artifacts are. Figure 5.5 shows a reconstructed event at 50 mm from the mask for both on- and off-axis tracks, where the increase of the near field artifacts is evident. As the distance from the mask increases, the Manhattan Distance gets closer to the values obtained with the on-axis tracks, as expected. Another characteristic of the off-axis results are the peaks at 125 mm and around 200 mm. These

94

peaks are the consequence of an ambiguity in the track reconstruction (Fig. 5.6): when a track is near the border of a line of pixels, the position of the reconstructed track is split among two pixels' lines, while in the ideal case the track is displayed in just one line. Despite all the off-axis tracks are simulated 148 mm above the center of the box, the effective position on the reconstructed image changes depending on the distance from the mask, making the reconstruction ambiguity appear only for some configurations: 125 mm, 200 mm and 225 mm from the mask. The increased Manhattan Distance for these configurations is then a result of the incorrect reconstruction.
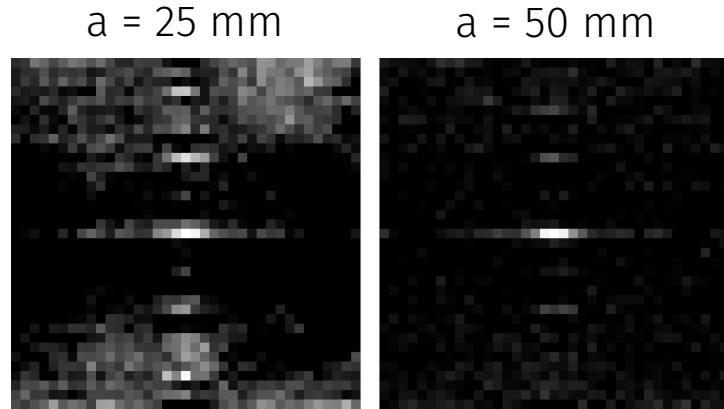
Figure 5.4: Reconstructed images for the two closest on-axis configurations.
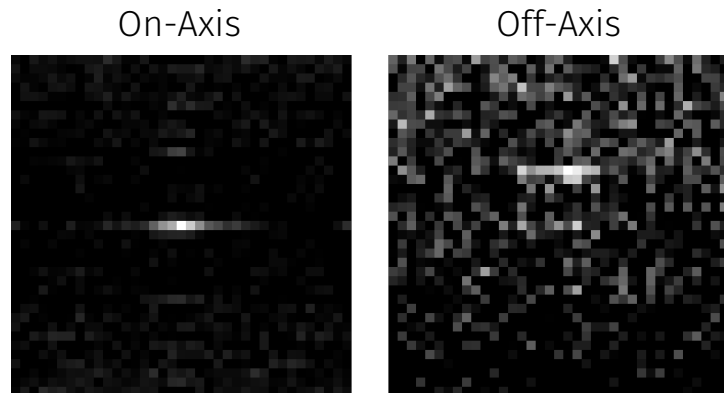
Figure 5.5: Comparison of the reconstructed images for both the on- and off-axis events at 50 mm from the mask.

This analysis confirms what expected from the study of the artifacts: the reconstruction is better for the on-axis tracks compared to the ones off-axis and its quality decreases as the tracks move away from the distance at which $\alpha = 1$. Whether or not this decrease of the images quality could impact on the track identification is verified with the next analysis.
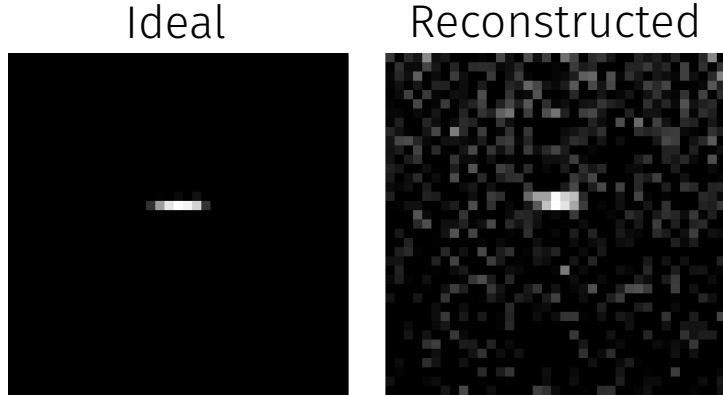
Figure 5.6: Ideal and reconstructed images for the off-axis configuration at 125 mm from the mask.

5.1.2 Tracks reconstruction

When analyzing the images to find the tracks, a method to choose whether or not a track is correctly identified is needed.

Recalling Eq. (3.17), the geometrical resolution of the detector, with the parameters as defined in Section 4.2 and a sensor of 88.8 mm of side, is found to be [13.68, 150.48] mm. This range depends upon the FOV of the camera and corresponds to the values obtained when analyzing the closest and the farthest images respectively. Since the simulated muons are generated horizontally, and because of the values of the detector resolution, one would expect to reconstruct the tracks in a single line of pixels. Thus, to verify whether a track is correctly identified or not, every track need to passes two different checks. First the position of the track is compared with the expected one. If it is found to be in the right pixel, and its errors are still inside the same pixel, the first check is passed. Second, the maximal and minimal slope of the track are obtained from the calculated slope and its error. If the track stays within the right line of pixels using both the slopes, the second check is also passed. Figure 5.7 shows a sketch of this procedure. During the analysis, the correct intercept and slope of the tracks were obtained analyzing the ideal images of each configuration with the same algorithm and, usually, passing of these cuts was sufficient to verify whether or not a track was correctly identified.

This analysis was performed for each event in each configuration and the number of correctly identified tracks was evaluated using the cuts previously described. Figure 5.8 shows the success ratio, defined as the ratio between the number of correctly identified tracks and the total number of tracks, for both the on- and off-axis configurations. The same results are reported in Table 5.1.

For the on-axis configurations, the tracks have been correctly identified about 100% of the times from right outside the near field region and up to 20 cm from the mask.
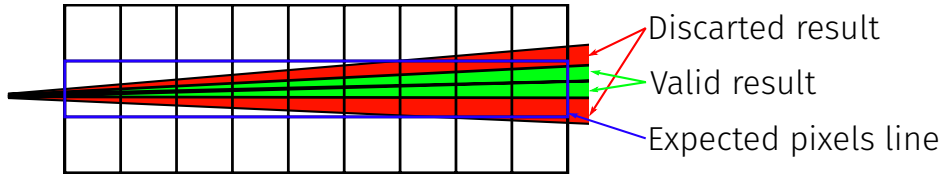
Figure 5.7: Scheme of the cut performed when analyzing the slope of the tracks. The colored regions are defined by the minimal and maximal slope obtained from the fit result.

Due to the the smooth behavior of the Manhattan Distance for track-mask distances
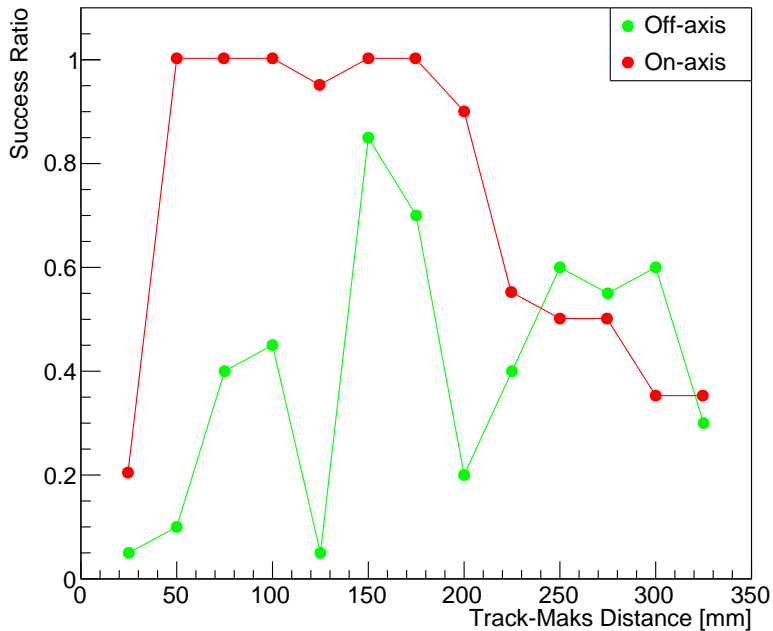
Figure 5.8: Success ratio of the track finding algorithm as a function of the track-mask distance.

greater than 20 cm, one would expect a similar ratio of identification for distance up to 35 cm. This is not the case as shown in Fig. 5.8, since a sharp decrease after 20 cm is present. The origin of this discontinuity can be associated with the increase of the FOV of the camera, thus the tracks detected are shorter and reconstructed with a number of pixels as smaller as the distance from the mask increases. In this condition the algorithm is unable to correctly identify a track.

a [mm]	On-axis	Off-axis	a [mm]	On-axis	Off-axis
25	0.2	0.05	200	0.9	0.2
50	1.0	0.1	225	0.55	0.4
75	1.0	0.4	250	0.5	0.6
100	1.0	0.45	275	0.5	0.55
125	0.95	0.05	300	0.35	0.6
150	1.0	0.85	325	0.35	0.3
175	1.0	0.7			

Table 5.1: Success ratio of the track finding algorithm for both the on- and off- axis configurations.

For the off-axis configurations, the increased Manhattan Distance reflects in a lower success ratio. Every configuration has a smaller number of correctly identified tracks, with only the farthest configurations having a success ratio similar to the one obtained for the on-axis tracks, as expected from the similar value of Manhattan Distance. Moreover, two sharp decreases of the success ratio are present. These correspond to the configurations for which the Manhattan Distance has a peak in Fig. 5.3 and are the consequence of the incorrect reconstruction of the tracks.

To increase the ratio of success, one could either improve the track finding algorithm, change the optimization of the parameters to reduce the FOV of the camera or use the anti-mask to reduce the amount of artifacts.

5.1.3   Detector Resolution

After the identification of the tracks, it is possible to evaluate the detector resolution. This is defined as:

$$\sigma_{det}(a) = \frac{\lambda(a)}{\sqrt{12}\sqrt{N(a)}} \tag{5.1}$$

where $\lambda(a)$ is the geometrical resolution of a coded camera (Eq. (3.17)) calculated at a distance a from the mask and N is the mean value of the number of points of the correctly identified tracks - both on- and off-axis - at the same distance from the mask. Figure 5.9 shows the result as a function of the track-mask distance.

Actually, using two cameras on the opposite faces of the detector, the track-mask distance is always lower than half the width of the box for one of the two cameras. The best resolution for each position in the detector is thus obtained using the result of the
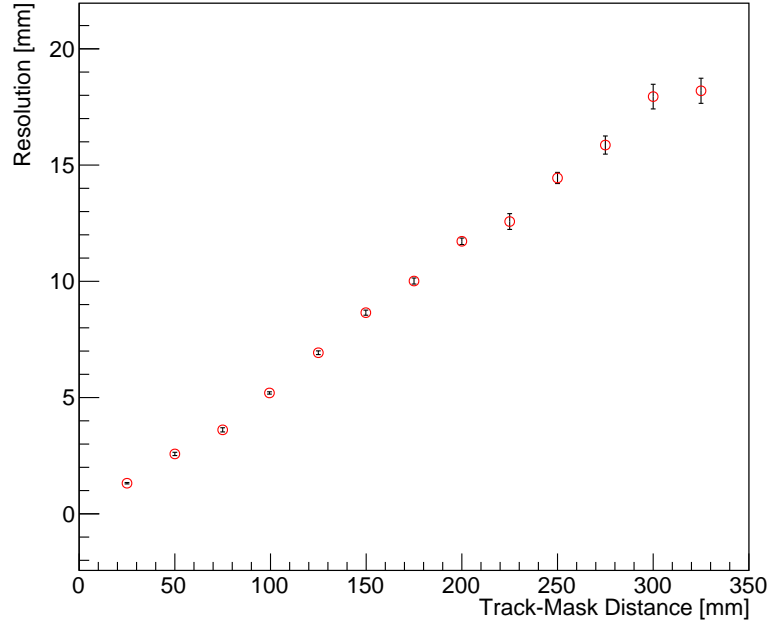
Figure 5.9: Detector resolution as a function of the track-mask distance.

camera closer to the track, as shown in Fig. 5.10. Table 5.2 summarizes the results for half the volume of the box, with the second half being symmetrical.

It is worth noticing that with Eq. (5.1) one obtains an ideal value of the resolution. When reconstructing more complex events, some complications could make Eq. (5.1) not valid anymore and a different method to estimate the resolution could be needed. The results presented in Table 5.2 can be used as a reference for the best resolution achievable with the detector used in the simulations.
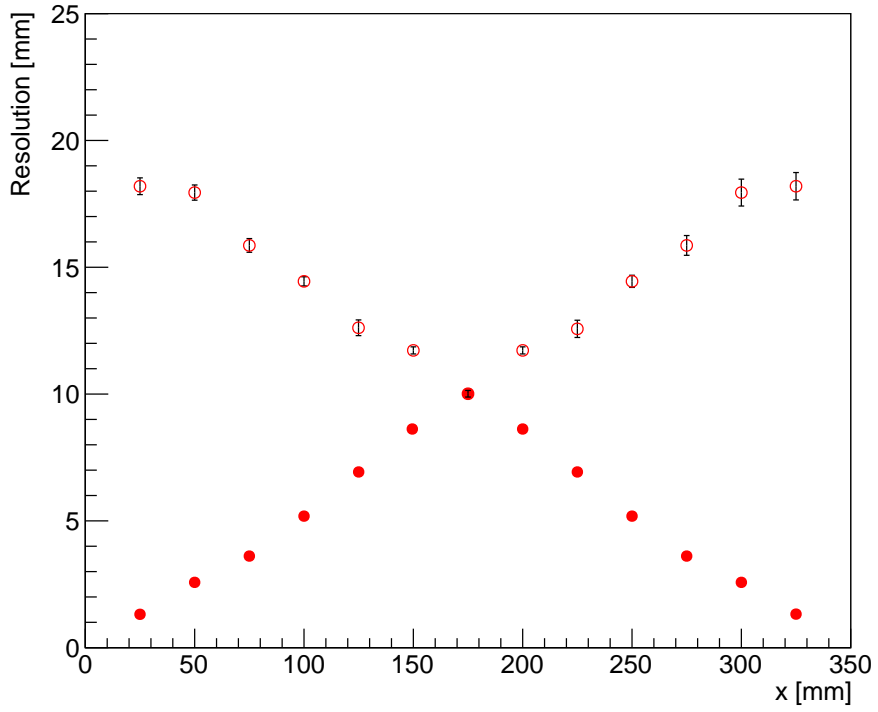
Figure 5.10: Detector resolution as a function of the position along the x-axis of the detector. For each position, the filled circle is the detector resolution obtained using the closest camera while the empty circle is the value obtained using the farthest one.

a [mm]	λ [mm]	N	σ_{det} [mm]
25	13.68	8.9 ± 0.4	1.32 ± 0.03
50	25.08	7.9 ± 0.4	2.5 ± 0.07
75	36.48	8.5 ± 0.4	3.61 ± 0.09
100	47.88	7.1 ± 0.2	5.19 ± 0.06
125	59.28	6.1 ± 0.1	6.93 ± 0.08
150	70.68	5.6 ± 0.1	8.6 ± 0.1
175	82.08	5.6 ± 0.1	10.0 ± 0.1

Table 5.2: Geometric resolution, mean number of points in a track and final detector resolution for each simulated position in the detector up to half the volume width.

5.2 Lens results

As for the masks, two lens-sensor systems are simulated. Both systems are placed in the center of the lateral faces of the LAr box and the same on- and off-axis distinction can be made for the simulated configuration. The simulated sensor is a 2000 × 2000 grid and its dimension is 20×20 cm.

5.2.1 Circle of Confusion size

The first step in the analysis of the reconstructed images is the measurement of the circle of confusion for every configuration. Since the sources in the simulations are tracks, the CoC is a band, which width defines the CoC of the image.

To measure the band's width, the number of illuminated pixels for each pixels' row is counted and plotted, as in Fig. 5.11. The width is taken as the difference from the last and first rows with a number of hits higher than zero. Multiplying this value by the dimension of a single pixel the band's width expressed in millimeters is obtained. The mean value of each configuration has been evaluated and the results are plotted in Fig. 5.12.
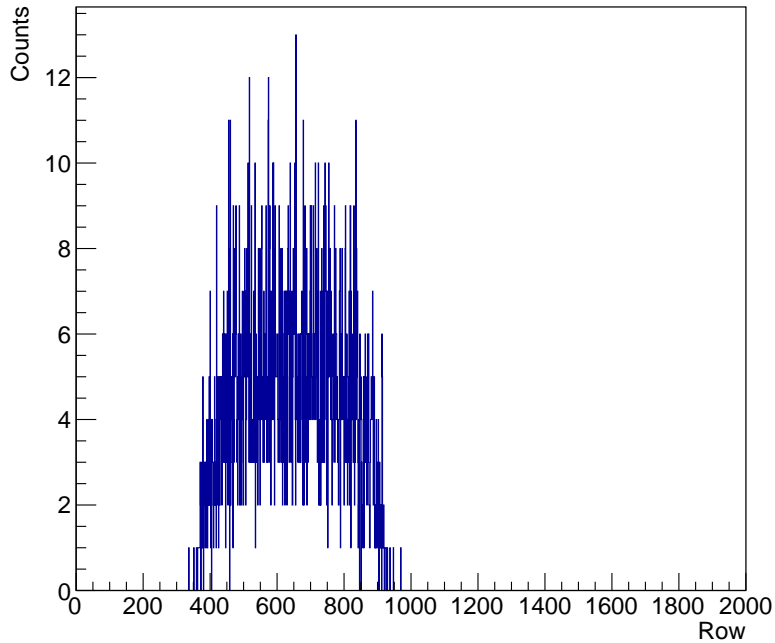

Figure 5.11: Number of illuminated pixels for each pixel's row.

101
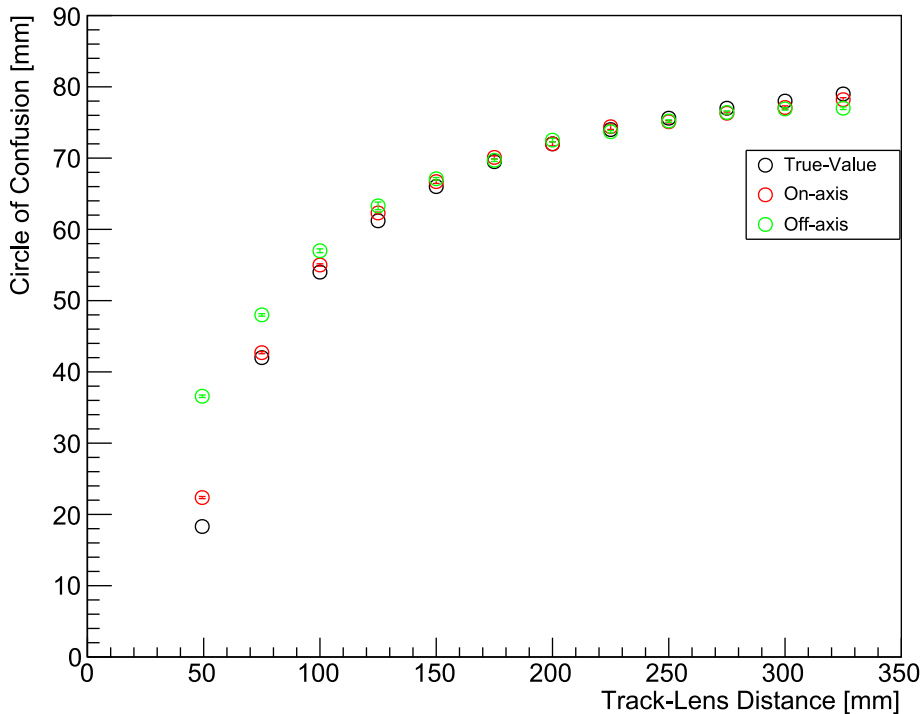
Figure 5.12: Mean value of the measured Circle of Confusion dimension for each on- and off-axis configuration as a function of the mask-lens distance.

The on-axis results are in agreement with the theoretical values obtained using Eq. (4.6) for every tested configuration. For the off-axis configurations, instead, the measured values are bigger than the expected ones for the configurations closest to the lens. This is a consequence of the different aperture of the light cone that reaches the sensor for the off-axis tracks, as shown in Fig. 5.13 and it should be taken into account when analyzing the off-axis results.

Moreover, in some cases, spurious pixels could be illuminated by secondary particles produced in the LAr box. These pixels, if found in a region far from the band, could spoil the measurement. To remove these pixels, for each row candidate to be a border of the band width, the adjacent rows are checked. If no other rows are illuminated, the row is excluded from the measurement.
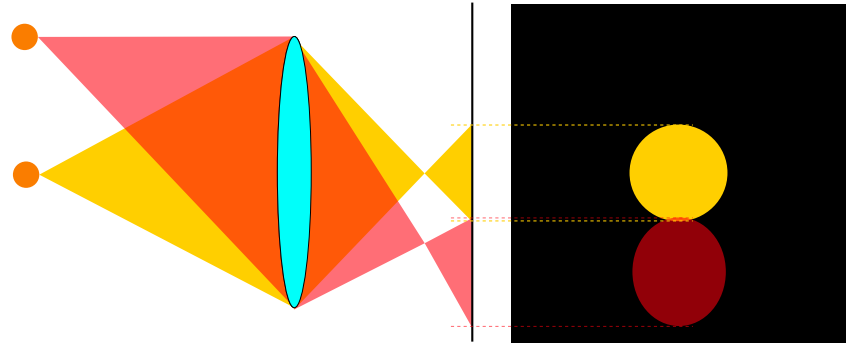
Figure 5.13: Sketch of the different Circle of Confusion generated by the on- and off-axis configurations.

5.2.2 Track position

With the measurement of the CoC dimension it is possible to obtain the track position in the LAr volume using Eq. (4.6). The mean distance is calculated for every configuration and in shown in Fig. 5.14.
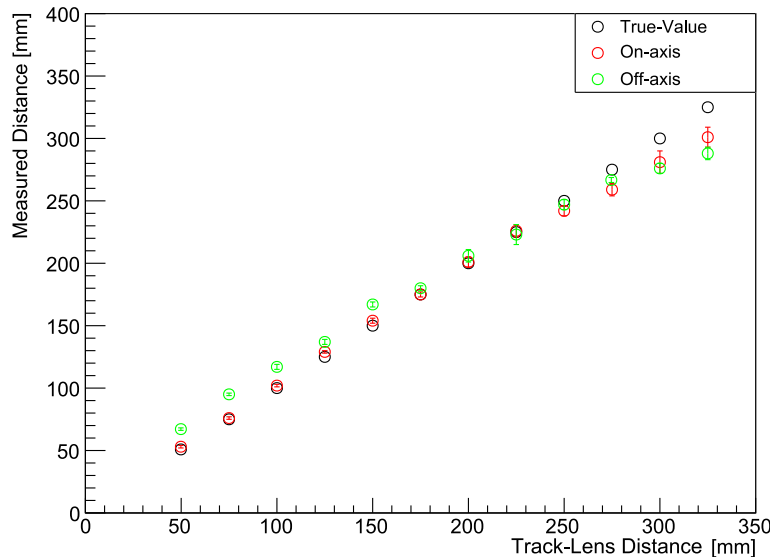

Figure 5.14: Mean value of the measured track distance for each on- and off-axis configuration as a function of the track-lens distance.

The obtained results for the on-axis configurations are mostly in agreement with the true values of the track position. However, for both the on- and off-axis configurations,

some differences between the measured and the true position of the tracks are present for the farthest configurations. These are a consequence of the procedure used to measure the CoC width, described in the previous section: at large distances, the broadening of the CoC makes some pixels at the CoC border appear as spurious pixels. These pixels are not counted in the band's width and its final dimension appears smaller than the real value. The smaller size of the CoC results in a shorter measured distance for the farthest simulated tracks, as shown in Fig. 5.14.

To correct this effect, the same procedure has been performed changing the parameters to be more accurate at the farthest distances from the mask. The results are shown in Fig. 5.15. As expected the modified procedure improves the result for the last points of both the on- and off- axis configurations. However, the inclusion of more spurious pixels spoils the results for shorted distances, due to a larger measured CoC.
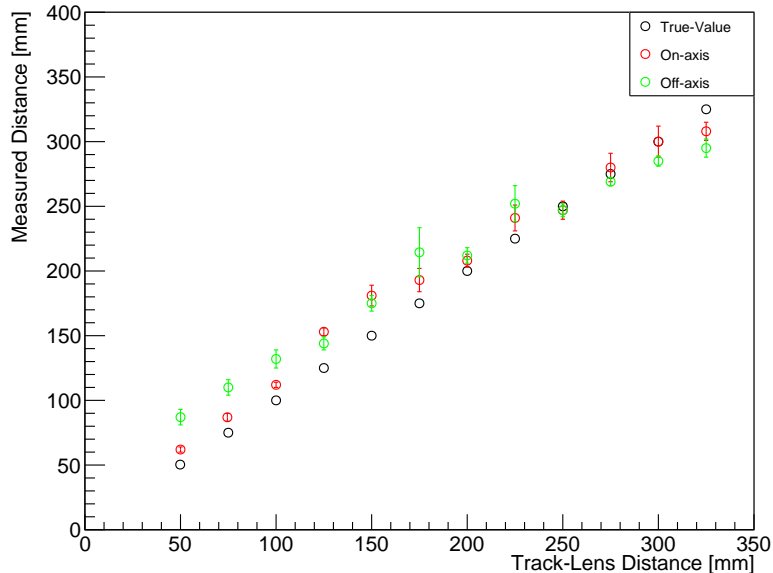

Figure 5.15: Mean value of the measured track distance for each on- and off-axis configuration as a function of the track-lens distance. The procedure used in the measurements has been optimized to be more accurate in the farthest region of the volume.

Moreover, for the closest off-axis configurations, the measured CoC values generate a systematically overestimated track-mask distance, as visible in Fig. 5.14. This effect could be corrected combining the results of multiple views from different faces of the detector.

5.2.3 Detector resolution

Once evaluated the track position, it is now possible to measure the resolution of the detector using lenses. To do so, for every event in each configuration, the difference between the measured track position and its true position a is calculated and plotted (Fig. 5.16). The mean value and the standard deviation of the distribution in Fig. 5.16
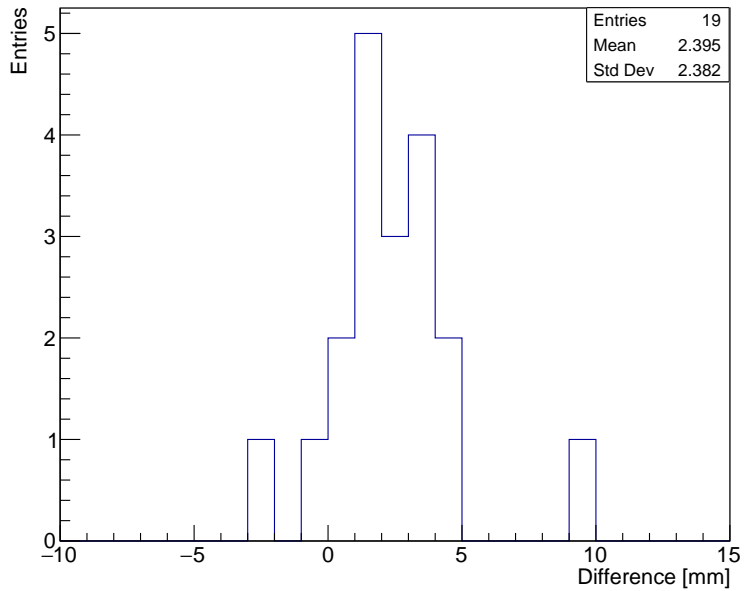

Figure 5.16: Distribution of the differences between the measured position and the true one for an off-axis event at 10 cm from the lens.

are then estimated. Due to the low statistics here simulated, instead of fitting data to a Gaussian distribution the mean and the root-mean-squared error are used. From here, the detector's resolution is obtained as

$$\sigma_{det}(a) = \frac{\Sigma(a)}{\sqrt{12}} \tag{5.2}$$

where $\Sigma(a)$ is twice the standard deviation obtained above. Figure 5.17 shows the results of the estimated resolution for every on- and off-axis configuration. For each configuration, the measurement has been performed using the best result from Fig. 5.14 and 5.15. As for the masks thus, Fig. 5.17 shows the best results achievable with the simulated detector.

Despite some fluctuations originated by the low statistics, the resolution of the detector worsens as the distance from the lens increases for both the on- and off-axis configurations. However, as for the masks, using two cameras on the opposite faces of
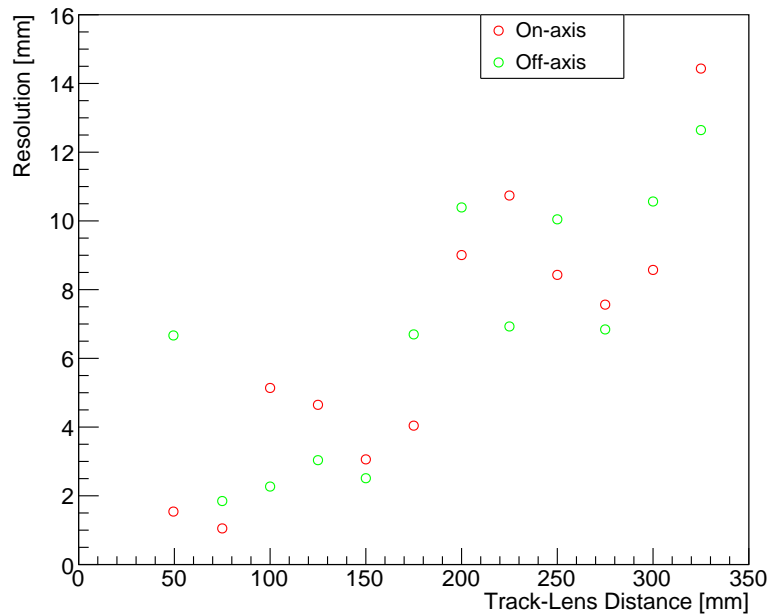
Figure 5.17: Resolution of the detector as a function of the track-lens distance for both the on- and off-axis configurations.

the detector, the best resolution for each position along the volume is obtained using the result of the camera closer to the track. Table 5.3 shows this result for both the on- and off-axis tracks up to half the volume width.

a [mm]	σ_{det}^{on} [mm]	σ_{det}^{off} [mm]
50	1.50	6.64
75	1.05	1.85
100	5.14	2.27
125	4.65	3.04
150	3.06	2.51
175	4.04	6.70

Table 5.3: Detector resolution with the lens as optical system for each simulated position in the detector up to half the volume width.

Conclusions and Outlooks

Neutrino oscillation is one of the most important discoveries regarding neutrinos. The existence of this phenomenon requests the neutrino and antineutrino masses to be different from zero and an extension of the Standard Model. Neutrino oscillations are thus of crucial importance as they could allow to answer some of the open questions about the nature of neutrinos. The identification of the still unknown parameters is thus one of the main objective of a large number of experiments.

One of these is DUNE, a dual-site experiment which will study neutrino oscillations trying to measure some of these parameters. Due to the high interaction rate expected at the DUNE Near Detector, a different type of detector with respect to the one used at the Far Detector (LArTPC) is needed.

In this thesis, the study of the feasibility of an innovative detector, able to operate in the Near Detector complex, was performed. This detector will exploit the scintillation light emitted by the Liquid Argon to provide a complete reconstruction of the events. Firstly, a comparison between two possible optical systems has been made. The studied systems are a coded camera, based on the Coded Aperture Technique, and a more traditional lens camera. The comparison highlighted the advantages and limitations of both the cameras: the coded camera can reconstruct tracks with a depth of field much larger than the lens camera most of the times but suffers from the presence of artifacts and the need of high intensity sources. On the contrary, the lens camera can reconstruct tracks with much lower intensity sources and without artifacts but the depth of field is limited to a small region around the focused distance. In order to evaluate the tracking performances, a complete simulation of the scintillation light produced by charged particles in Liquid Argon has been performed. With this, the tracks reconstruction capability of both the optical systems was tested. The detector resolution using both the cameras was estimated, and found to be, in optimal conditions, $< (10.0 \pm 0.1)$ mm for the coded camera and < 6.7 mm for the lens camera.

This thesis is the first step in the development of this new detection technique. The main parameters involved are now known and from the results here obtained many improvements are possible. The most important one being the 3D reconstruction of the events using multiple views from cameras on different faces of the detector volume. Moreover, this thesis is part of a project which aims to build a prototype of a detector

based on this technique and the results here obtained will be used for the optimization of such a prototype. Lastly, this work highlighted the need for an high amount of scintillation photons for the coded camera to work. Future designs using different types of scintillator materials could thus be studied to better exploit this technique.

Appendix A

Track Finding Algorithm

In the following, the algorithm used to find the tracks during the analysis is described.

Seeds Identification   The first step performed by the algorithm is the identification of the seeds needed to start the search. A seed is defined as three fired pixels, at a mutual maximal distance of one empty pixel. Figure A.1 shows some examples of valid and invalid seeds.
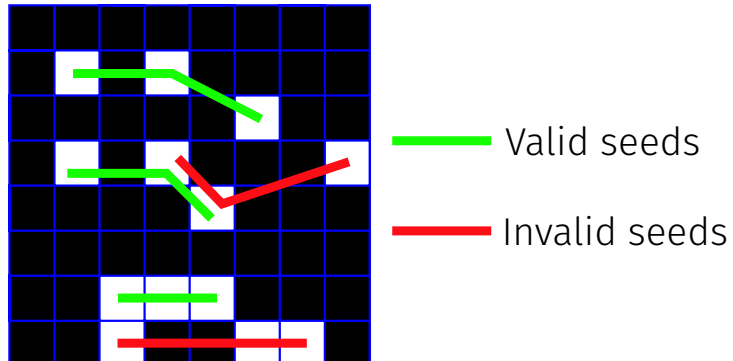

Figure A.1: Sketch of the process of selection of the seeds.

The minimal pixel intensity to be included in a seed is tunable, to minimize the inclusion of the background noise. Figure A.2 shows an image used as an example in this Appendix as well as the seeds found varying the minimal level of intensity.

Seeds Propagation   After the seeds have been found, a linear fit is performed for each one (Fig. A.3) and the result is used to search for other pixels to be added along the direction obtained. A minimal pixel intensity is used as a cut. When such a pixel is found, it is added to the seed and a new fit is performed. The process is then iterated with the result of the new fit. When a seed reaches a given number of entries or when the
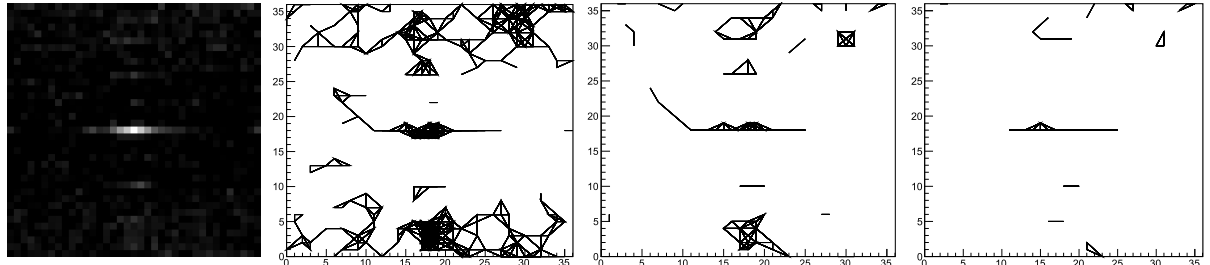
Figure A.2: Example of a reconstructed image (left) and found seeds for three different values of minimal allowed intensity.
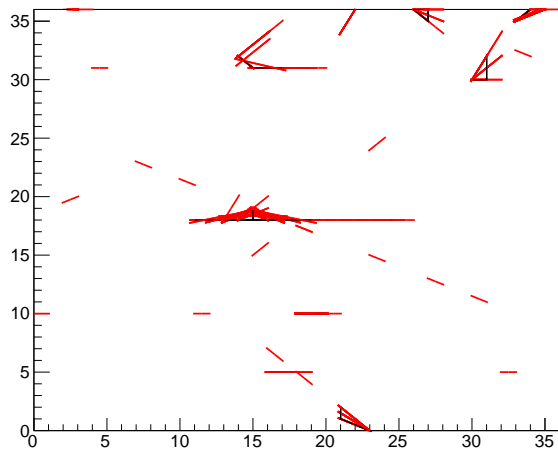

Figure A.3: Fitted seeds.

algorithm scans every position along the x-direction of the image, the algorithm stops. In the first case the seed is saved, while in the second one it is rejected. A sketch of this process is showed in Fig. A.4, while Fig. A.5 shows the result of the propagation of the seeds found in Fig. A.3.

To reduce the number of overlapping seeds, the slope and intercept are compared and possibly merged. The seeds composed by a number of pixels smaller than a minimal value are rejected.

Track Identification   To identify the region of the image in which the track is, the slopes and intercepts of all the final seeds are plotted in a 2D histogram, as per Fig. A.6. The peaks of this histogram are used to identify the parameters constraining the final track finding step. A Gaussian fit on both the slope and intercept distributions obtained from the 2D histogram is applied (Fig. A.7).

The final step is performed scanning each pixel in the region included within param-
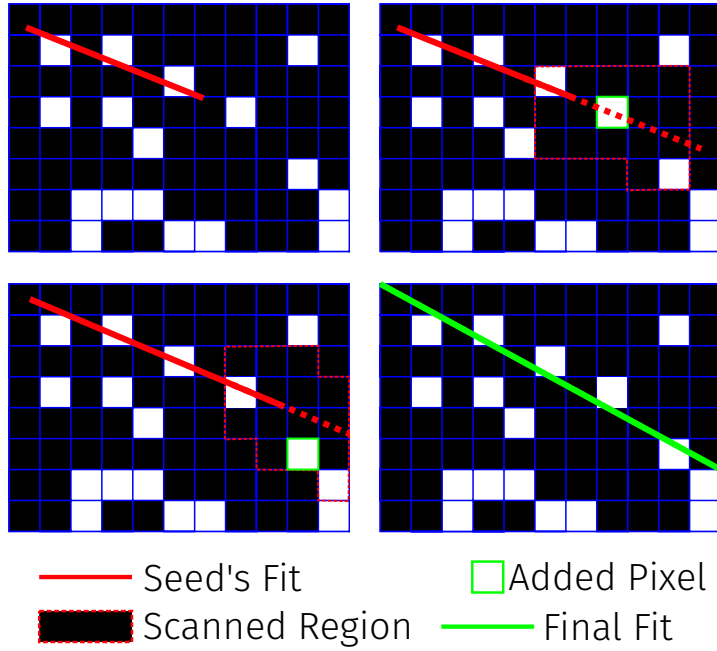
Figure A.4: Sketch of the process of propagation for the seeds. The scanned region is selected as the 3x3 area surrounding each pixel that intercepts the fit direction.
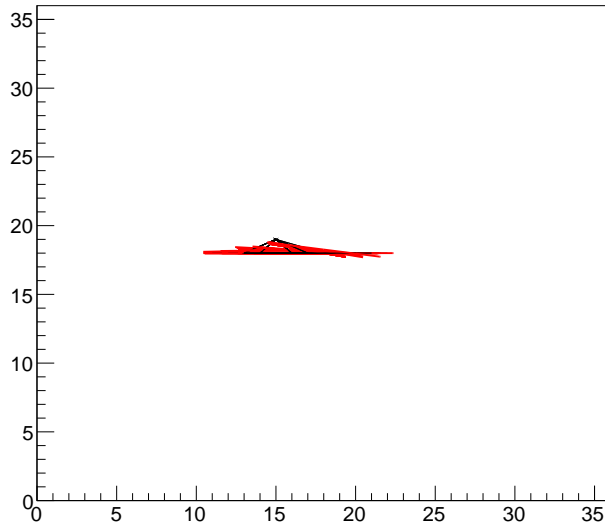

Figure A.5: Seeds that survive the propagation and merging.

eter error (Fig. A.8). For each position along the x-direction of the image, the pixel with the higher intensity, among the ones with intensity higher than a minimal value, is taken

112
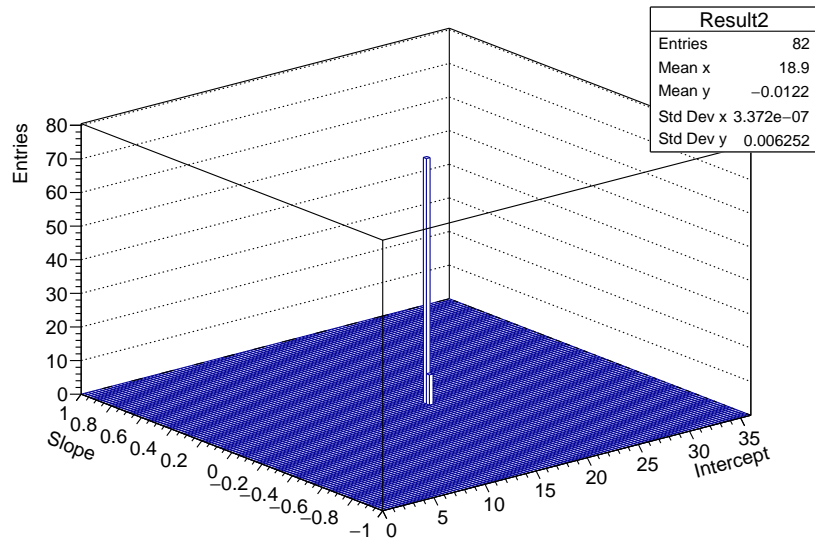
Figure A.6: 2D distribution of the seeds' fit results.
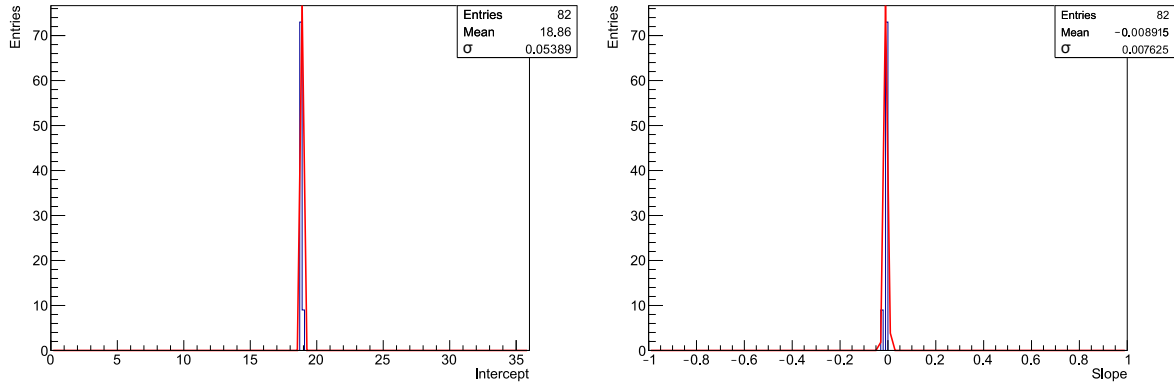
Figure A.7: Distributions of intercepts and slopes of the seeds around the peak of the 2D distribution.

and the final pattern is the track found by the algorithm. Figure A.9 shows the result of this last step and the comparison with the real position of the track.
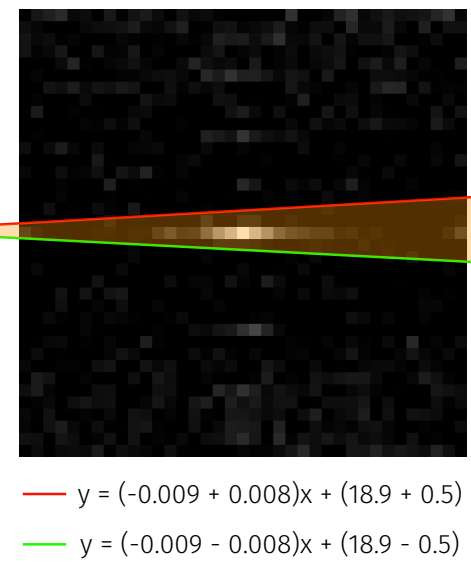
Figure A.8: Scanned region of the image. The slope and intercept of the two lines are obtained from the fit's results of Fig. A.7.
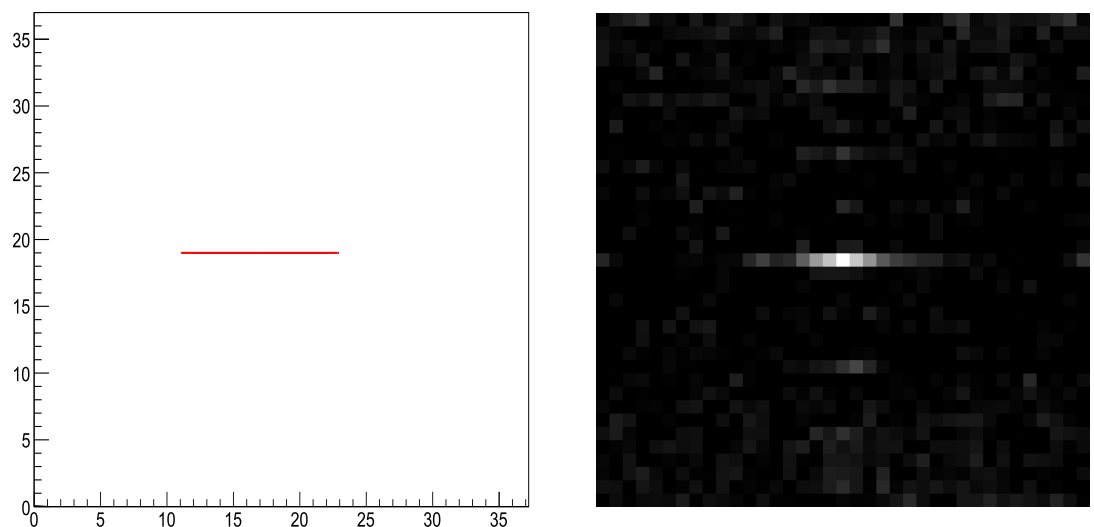

Figure A.9: Final track found by the algorithm and comparison with the analyzed image.

Bibliography

[1] V. N. Aseev *et al.*, "An upper limit on electron antineutrino mass from Troitsk experiment", *Phys. Rev.*, vol. D84, p. 112003, 2011.

[2] C. Kraus *et al.*, "Final results from phase II of the Mainz neutrino mass search in tritium beta decay", *Eur. Phys. J.*, vol. C40, pp. 447–468, 2005.

[3] G. B. Franklin, "The KATRIN Neutrino Mass Measurement: Experiment, Status, and Outlook", in *13th Conference on the Intersections of Particle and Nuclear Physics (CIPANP 2018) Palm Springs, California, USA, May 29-June 3, 2018*, 2018.

[4] M. Tanabashi *et al.*, "Review of particle physics", *Phys. Rev. D*, vol. 98, p. 030001, Aug 2018.

[5] K. Zuber, *Neutrino Physics, Second Edition.* Aug. 2011.

[6] S. T. Petcov, "The Nature of Massive Neutrinos", *Adv. High Energy Phys.*, vol. 2013, p. 852987, 2013.

[7] C. Giunti and C. W. Kim, *Fundamentals of Neutrino Physics and Astrophysics.* 2007.

[8] P. Lipari, "Introduction to neutrino physics", in *2001 CERN-CLAF School of high-energy physics, Itacuruca, Brazil, 6-19 May, 2001: Proceedings*, pp. 115–199, 2001.

[9] C. Giunti and M. Laveder, "Neutrino mixing", 2003.

[10] Y. Farzan and M. Tortola, "Neutrino oscillations and Non-Standard Interactions", *Front.in Phys.*, vol. 6, p. 10, 2018.

[11] F. Capozzi, E. Di Valentino, E. Lisi, A. Marrone, A. Melchiorri, and A. Palazzo, "Global constraints on absolute neutrino masses and their ordering", *Phys. Rev.*, vol. D95, no. 9, p. 096014, 2017.

[12] F. P. An *et al.*, "Measurement of electron antineutrino oscillation based on 1230 days of operation of the Daya Bay experiment", *Phys. Rev.*, vol. D95, no. 7, p. 072006, 2017.

[13] S. H. Seo *et al.*, "Spectral Measurement of the Electron Antineutrino Oscillation Amplitude and Frequency using 500 Live Days of RENO Data", *Phys. Rev.*, vol. D98, no. 1, p. 012002, 2018.

[14] A. Meregaglia, "Multi detector results from the Double Chooz experiment", in *Proceedings, 52nd Rencontres de Moriond on Electroweak Interactions and Unified Theories: La Thuile, Italy, March 18-25, 2017*, pp. 359–366, 2017.

[15] V. Barger, K. Whisnant, and R. J. N. Phillips, "CP nonconservation in three-neutrino oscillations", *Phys. Rev. Lett.*, vol. 45, pp. 2084–2088, Dec 1980.

[16] M. C. Gonzalez-Garcia, M. Maltoni, and T. Schwetz, "Updated fit to three neutrino mixing: status of leptonic CP violation", *JHEP*, vol. 11, p. 052, 2014.

[17] M. Freund, "Analytic approximations for three neutrino oscillation parameters and probabilities in matter", *Phys. Rev.*, vol. D64, p. 053003, 2001.

[18] W. Marciano and Z. Parsa, "Intense neutrino beams and leptonic CP violation", *Nucl. Phys. Proc. Suppl.*, vol. 221, pp. 166–172, 2011.

[19] K. Abe *et al.*, "Measurement of neutrino and antineutrino oscillations by the t2k experiment including a new additional sample of ν_e interactions at the far detector", *Phys. Rev. D*, vol. 96, p. 092006, Nov 2017.

[20] P. Adamson *et al.*, "Constraints on oscillation parameters from ν_e appearance and ν_μ disappearance in nova", *Phys. Rev. Lett.*, vol. 118, p. 231801, Jun 2017.

[21] W. Winter, "Neutrino mass hierarchy: Theory and phenomenology", *AIP Conf. Proc.*, vol. 1666, no. 1, p. 120001, 2015.

[22] X. Qian and P. Vogel, "Neutrino Mass Hierarchy", *Prog. Part. Nucl. Phys.*, vol. 83, pp. 1–30, 2015.

[23] I. Esteban, M. C. Gonzalez-Garcia, A. Hernandez-Cabezudo, M. Maltoni, and T. Schwetz, "Global analysis of three-flavour neutrino oscillations: synergies and tensions in the determination of $\theta_2 3, \delta_C P$, and the mass ordering", *JHEP*, vol. 01, p. 106, 2019.

[24] C. Adams *et al.*, "The Long-Baseline Neutrino Experiment: Exploring Fundamental Symmetries of the Universe", in *Snowmass 2013: Workshop on Energy Frontier Seattle, USA, June 30-July 3, 2013*, 2013.

[25] R. Acciarri *et al.*, "Long-Baseline Neutrino Facility (LBNF) and Deep Underground Neutrino Experiment (DUNE), Conceptual Design Report Volume 2: The Physics Program for DUNE at LBNF", 2015.

[26] E. Kearns *et al.*, "Hyper-Kamiokande Physics Opportunities", in *Proceedings, 2013 Community Summer Study on the Future of U.S. Particle Physics: Snowmass on the Mississippi (CSS2013): Minneapolis, MN, USA, July 29-August 6, 2013*, 2013.

[27] P. Adamson *et al.*, "The NuMI Neutrino Beam", *Nucl. Instrum. Meth.*, vol. A806, pp. 279–306, 2016.

[28] R. Acciarri *et al.*, "Long-Baseline Neutrino Facility (LBNF) and Deep Underground Neutrino Experiment (DUNE), Conceptual Design Report Volume 4: The DUNE Detectors at LBNF", 2016.

[29] B. Abi *et al.*, "The DUNE Far Detector Interim Design Report, Volume 2: Single-Phase Module", 2018.

[30] B. Abi *et al.*, "The Single-Phase ProtoDUNE Technical Design Report", 2017.

[31] A. A. Machado and E. Segreto, "ARAPUCA a new device for liquid argon scintillation light detection", *JINST*, vol. 11, no. 02, p. C02004, 2016.

[32] E. Segreto *et al.*, "Liquid Argon test of the ARAPUCA device", *JINST*, vol. 13, no. 08, p. P08021, 2018.

[33] C. Amsler *et al.*, "ArgonCube: a novel, fully-modular approach for the realization of large-mass liquid argon TPC neutrino detectors", Tech. Rep. CERN-SPSC-2015-009. SPSC-I-243, CERN, Geneva, Feb 2015.

[34] Argoncube Website. https://argoncube.org/duneND.html.

[35] G. Adamov *et al.*, "A Proposal to enhance the DUNE Near-Detector Complex", DUNE Document Database, DUNE-doc-13262, 2019.

[36] T. Doke *et al.*, "Let dependence of scintillation yields in liquid argon", *Nuclear Instruments and Methods in Physics Research Section A: Accelerators, Spectrometers, Detectors and Associated Equipment*, vol. 269, no. 1, pp. 291 – 296, 1988.

[37] G. M. Seidel, R. E. Lanou, and W. Yao, "Rayleigh scattering in rare gas liquids", *Nucl. Instrum. Meth.*, vol. A489, pp. 189–194, 2002.

[38] A. Neumeier *et al.*, "Attenuation of vacuum ultraviolet light in liquid argon", *The European Physical Journal C*, vol. 72, 10 2012.

117

[39] E. E. Fenimore and T. M. Cannon, "Coded aperture imaging with uniformly redundant arrays", *Appl. Opt.*, vol. 17, pp. 337–347, Feb 1978.

[40] R. Accorsi, "Design of a near-field coded aperture cameras for high-resolution medical and industrial gamma-ray imaging", 08 2005.

[41] S. R. Gottesman and E. E. Fenimore, "New family of binary arrays for coded aperture imaging", *Appl. Opt.*, vol. 28, pp. 4344–4352, Oct 1989.

[42] R. Accorsi and R. C. Lanza, "Near-field artifact reduction in planar coded aperture imaging", *Appl. Opt.*, vol. 40, pp. 4697–4705, Sep 2001.

[43] J. Allison *et al.*, "Recent developments in geant4", *Nuclear Instruments and Methods in Physics Research Section A: Accelerators, Spectrometers, Detectors and Associated Equipment*, vol. 835, pp. 186 – 225, 2016.

[44] eSource Optics catalog. https://www.esourceoptics.com.

[45] S. Sural, C. Histogram, E. Distance, M. Distance, V. Cosine, A. Distance, H. Intersection, a. Vadivel, and A. Majumdar, "Performance comparison of distance metrics in content-based image retrieval applications", *Proc. of Internat. Conf. on Information Technology, Bhubaneswar, India*, pp. 159–164, 01 2003.

[46] Y. Bando and T. Nishita, "Towards digital refocusing from a single photograph.", pp. 363–372, 01 2007.

[47] M. Pharr, W. Jakob, and G. Humphreys, *Physically Based Rendering (Third Edition)*. 2017.